Multi-mode Absorption Spectroscopy for multi-species and multi-parameter sensing

A thesis submitted for the degree of Doctor of Philosophy

Seamus O'Hagan

Keble College, University of Oxford

Hilary Term 2017

Multi-mode Absorption Spectroscopy for multi-species and multi-parameter sensing

Seamus O'Hagan, Keble College

A thesis submitted in partial fulfilment of the requirement for the degree of Doctor of Philosophy of the University of Oxford.

Hilary Term, 2017

Abstract

The extension of Multi-mode Absorption Spectroscopy (MUMAS) to the infra-red spectral region for multi-species gas sensing is reported. A computationally efficient, theoretical model for analysis of MUMAS spectra is presented that avoids approximations used in previous work and treats arbitrary and time-dependent spectral intensity envelopes, thus facilitating the use of commercially available Interband Cascade Lasers (ICLs) and Quantum Cascade Lasers (QCLs).

The first use of an ICL for MUMAS is reported using a multi-mode device operating at 3.7 µm to detect CH_4 transitions over a range of 30 nm. Mode-linewidths are measured using the pressure-dependent widths of an isolated absorption feature in HCl. Multi-species sensing is demonstrated by measurement of partial pressures of CH_4, C_2H_2 and H_2CO in a low-pressure mixture with uncertainties of around 10%. Detection of CH_4 in N_2 at 1 bar is demonstrated using a shorter-cavity ICL to resolve spectral features in pressure-broadened and congested spectra.

The first use of a QCL for MUMAS is reported using a commercially available device operating at 5.3 µm to detect multiple absorption transitions of NO at a partial pressure of 2.79 µbar in N_2 buffer gas. The revised model is shown to enable good fits to MUMAS data by accounting for the time-variation of the spectral intensity profile during frequency scanning. Individual mode-linewidths are derived from fits to pressure-dependent MUMAS spectra and features from background interferences due to H_2O in laboratory air are distinguished from those of the target species, NO. Data obtained at scan rates up to 10 kHz demonstrate the potential for achieving short measurement times.

The development of a balanced ratiometric detection scheme for MUMAS with commercially available multi-mode lasers operating at 1.5 µm is reported for simultaneous detection of CO and CO_2 showing improved SNR performance over previous direct transmission methods and suitability for a compact field-employable instrument. In addition, MUMAS spectra of CO_2 are used to derive gas temperatures with an uncertainty of 3.2% in the range $300 - 700$ K.

To my parents, Alison and Kevin.

Acknowledgements

After seven years as a student at Oxford, I am finally ready to conclude my student life. During this time, I have had countless incredible opportunities and experiences and have been privileged to have been taught by and to have spoken with many inspiring academics and colleagues. There are a number of people whom I would like to thank who have lent me their support, encouragement and friendship.

Firstly, I would like to thank my supervisor, Prof. Paul Ewart, for providing the opportunity for me to undertake this research. I will always be indebted to him for his great kindness, wonderful supervision, encouragement, support and advice. Paul has been a role-model to me, and his principled academic approach, honesty and generosity are qualities that I aspire to. His world view, extraordinary in its unwavering positivity, has certainly left its mark upon my own. Along with hiking the Franconia Notch and the mountain biking we enjoyed together at the Gordon Research Conference 2015, our many enlightening conversations have been one of the highlights of my DPhil.

I must also thank Dr. Henry Northern for his excellent guidance, intuition and expertise during the project, without which this body of work would be far worse off. I am also grateful to him for his meticulousness and advice during his many readings of this thesis. Along with providing great company in the lab during longs periods of experimental work, many of the key developments were made during the time we spent bouncing ideas off of one other.

I wish to thank Prof. Grant Ritchie for enabling a collaboration with his research group in the chemistry department and for his entertaining company at conferences. Acknowledgement must also go to Tomas Pinto of the Ritchie group for his work during this collaboration.

I would also like to thank all members of the Ewart group, both past and present, for their advice and company. Andrew Luers, Chris Willman, Ben Williams, Felix Förster and Anna-Lena Sahlberg have always been quick to lend support, academically or otherwise.

EPSRC and the Oxford Physics Department deserve recognition for their financial support, as do all the workshop and administrative staff for their assistance.

My friends, house-mates, team-mates and fellow members of Keble MCR also deserve acknowledgement for the endless enjoyment they have provided. Many lifelong friendships are sure to follow. Without the experiences I have shared with them during numerous non-academic 'distractions', I would probably not have finished at all.

I wish to thank my parents, to whom I owe everything, for their unerring support in helping me reach where I am today. I'm grateful to my siblings for putting up with me and for both keeping me grounded and 'correcting' my accent every time I return home.

Finally to Libby, for her joy, inspiration and love.

Contents

1 Introduction **1**
- 1.1 Introduction to MUMAS . . . 4
- 1.2 Overview of this thesis . . . 5

2 Background **9**
- 2.1 Overview . . . 9
- 2.2 Optical gas sensing . . . 9
- 2.3 Laser absorption spectroscopy . . . 13
  - 2.3.1 Line-strength . . . 14
  - 2.3.2 Broadening mechanisms . . . 16
- 2.4 Tunable diode laser absorption spectroscopy . . . 21
  - 2.4.1 SNR enhancements . . . 22
- 2.5 Broad spectral coverage . . . 25
- 2.6 Existing broad spectral-coverage techniques . . . 27
  - 2.6.1 Multi-transition TDLAS . . . 27
  - 2.6.2 Broadband spectroscopy . . . 29
  - 2.6.3 Programmable mid-infrared source for gas sensing (MIREGAS) . . . 30
  - 2.6.4 Correlation spectroscopy . . . 31
  - 2.6.5 Frequency-comb spectroscopy . . . 33
  - 2.6.6 Multi-heterodyne spectroscopy . . . 36
- 2.7 Multi-mode Absorption Spectroscopy (MUMAS) . . . 38
- 2.8 Summary . . . 42

3 The theory of MUMAS **44**
- 3.1 Overview . . . 44
- 3.2 Theory of operation . . . 45
- 3.3 Theory of tuning . . . 51
- 3.4 Modelling of MUMAS . . . 54
  - 3.4.1 Spectroscopic data modelling . . . 54
  - 3.4.2 Computational modelling code for the translation-model . . . 55
  - 3.4.3 Computational modelling code for the expansion-model . . . 57
- 3.5 Laser requirements for MUMAS applications . . . 62
- 3.6 Summary . . . 66

4 MUMAS with Interband Cascade Lasers **67**
4.1 Overview . . . 67
4.2 Interband Cascade Lasers . . . 68
4.3 Experimental apparatus and procedure . . . 71
4.3.1 Apparatus . . . 71
4.3.2 Data processing . . . 75
4.3.3 Linearisation of MUMAS frequency scale . . . 76
4.4 Fitting the model to experimental data . . . 80
4.4.1 Determing the laser parameters . . . 81
4.4.2 Additional fitting parameters . . . 84
4.4.3 Fitting procedure . . . 85
4.5 Results . . . 88
4.5.1 Linewidth measurements . . . 88
4.5.2 Mid-infrared MUMAS spectrum of methane . . . 90
4.5.3 Fitting sequential pseudo-repeat-units . . . 93
4.5.4 Enhanced spectral coverage with a single device . . . 95
4.5.5 Species concentration measurements . . . 97
4.5.6 Multi-species detection . . . 99
4.5.7 Minimum Detection Limit (MDL) . . . 104
4.5.8 Atmospheric pressure sensing . . . 109
4.6 Current limitations of ICLs for MUMAS . . . 112
4.7 Conclusion . . . 114

5 MUMAS with Quantum Cascade Lasers **116**
5.1 Overview . . . 116
5.2 Experimental details . . . 117
5.3 MUMAS spectrum of nitric oxide . . . 119
5.4 Linewidth measurements . . . 122
5.5 Detection of an interfering species . . . 125
5.6 Laser intensity envelope effects on data analysis . . . 127
5.6.1 Inaccurate measurement of intensity envelope . . . 129
5.6.2 Effect of a varying MFP on MUMAS spectra . . . 134
5.7 Fast scan rates . . . 136
5.8 Conclusions . . . 138

6 Development of MUMAS in the near-infrared region **140**
6.1 Overview . . . 140
6.2 Experimental details . . . 142
6.3 Balanced ratiometric detection scheme . . . 144
6.3.1 Dynamic range improvements . . . 147
6.3.2 Comparison of detection schemes . . . 148
6.4 Computational modelling of a varying laser intensity envelope . . . 150
6.5 MUMAS with balanced detection and a varying mode intensity envelope . 153
6.5.1 Linewidth measurements . . . 153

6.5.2 Multi-species detection . . . 154
6.5.3 Atmospheric pressure sensing . . . 156
6.6 Thermometry with MUMAS . . . 157
6.6.1 Temperature measurements . . . 158
6.6.2 Temperature sensitivity . . . 164
6.6.3 Temperature sensitivity enhancement . . . 166
6.7 Conclusion . . . 168

7 Conclusions **170**

8 Future work **175**
8.1 Portable MUMAS device . . . 176
8.2 Mid-infrared balanced ratiometric detection scheme . . . 178
8.3 Multi-heterodyne MUMAS . . . 178
8.4 Measurement of relaxation dynamics in excited species . . . 180

A Derivation of the MUMAS equation **182**

B Approximation of Voigt profiles **187**

List of Abbreviations

CCS Carbon Capture & Storage

CEAS Cavity-Enhanced Absorption Spectroscopy

CEO Carrier-Envelope Offset

CRDS Cavity Ring-Down Spectroscopy

DFCS Direct Frequency Comb Spectroscopy

DFG Difference Frequency Generation

EC-DL External-Cavity Diode Laser

FFT Fast Fourier Transform

FP-QCL Fabry-Perot Quantum Cascade Laser

FSR Free Spectral Range

FWHM Full-Width at Half Maximum

HITEMP High-temperature molecular spectroscopic database

HITRAN High-resolution transmission molecular absorption database

HWHM Half-Width at Half Maximum

ICL Interband Cascade Laser

MDL Minimum Detection Limit

MEMS Microelectromechanical Systems

MFP Mode Fractional Power

MHF Mode-Hope Free

MIREGAS Mid-Infrared Source for Gas Sensing

MUMAS Multi-mode Absorption Spectroscopy

NRL Navel Research Laboratory

OF-CEAS Optical-Feedback Cavity-Enhanced Absorption Spectroscopy

OFC Optical Frequency Comb

PIC Photonic Integrated Circuit

QCL Quantum Cascade Laser

RF Radio-Frequency

SLED Superluminescent Light-Emitting Diode

SNR Signal-to-Noise Ratio

TDLAS Tunable Diode Laser Absorption Spectroscopy

TEC Thermoelectic cooling

UV Ultraviolet

VCSEL Vertical-Cavity Surface-Emitting Laser

VIPA Virtually-Imaged Phased Array

WMS Wavelength-Modulation Spectroscopy

Chapter 1

Introduction

The ability to quantitatively detect and monitor gaseous species lends itself to a large range of applications, both scientific and commercial. A technique that enables monitoring of gaseous species could be used in a variety of situations, including enabling air quality control in cities, optimising industrial processes and also for potential use in medical diagnostics.

When attempting to mitigate anthropogenic climate change, gas detection can be used to identify sources of offending emissions and to monitor and optimise the efficacy of abatement systems in order to reduce the emissions at source. Furthermore, atmospheric science and modelling depends on data obtained from gas monitoring, and complex monitoring schemes may be able to provide insights into the fundamental reaction pathways in the atmosphere, further aiding climate models.

In industrial processes, levels of feedstock can be altered for the purpose of quality assurance, and the intermediates, whose concentrations may be rapidly varying, can be studied to maximise product yield. Air pollutants are detrimental to human health; environmental monitoring is therefore essential for regulation and control of harmful emissions. As abnormal concentrations of particular species in a patient's breath can be

indicative of certain diseases, the ability to monitor the concentrations of these species would constitute a large breakthrough in clinical diagnosis. In addition, the concentrations of certain species in a patient's breath can also be used for real-time monitoring of oxygen consumption during critical care.

Non-optical methods of gas monitoring exist, including gas chromatography, mass spectrometry, and calorimetric methods. Whilst a number of these techniques result in accurate measurements with high reliability, they present certain limitations. They typically involve the use of expensive, bulky equipment, and they also require sampling, thus precluding any real-time or non-invasive sensing. Other techniques, such as those based on chemical activation, have been highly developed for certain applications and are widely and successfully deployed. However, the majority of these non-optical methods target one particular species, and so multiple devices are required for multiple species.

Optically based sensors are an attractive alternative for gas sensing, as they overcome many of the limitations of the other techniques discussed above and also have several superior performance characteristics. A particular strength is that because each species has a characteristic absorption spectrum, they can be applied with high specificity. This avoids the need for a discrete device for each target species or having each device based on a different technique with dissimilar operating conditions, mismatched quantitative accuracy and precision and differing calibration procedures. Furthermore, optically based sensors can provide a direct, highly accurate quantitative measurement of the properties of a gaseous sample. Additionally, they are non-invasive whilst still allowing in-situ detection. Finally, their fast time-response enables real-time monitoring of the properties of rapidly varying gaseous systems.

The development of laser diodes in the 1960s provided a suitable light source for use in optical gas sensors. Laser diodes are now widely used for laser absorption spectroscopy in a highly established gas-sensing technique called Tunable Diode Laser Absorption

Spectroscopy (TDLAS). Their narrow linewidth enables high-resolution absorption spectra to be obtained, thus allowing for high selectivity and high specificity. Furthermore, they are typically small and robust with a reasonable power output, and yet they have low power requirements and high immunity from vibrations, temperature fluctuations and other noise sources. They therefore lend themselves to integration in a portable and robust device.

The principal disadvantage of single-mode diode lasers, however, is their intrinsic limitation on the Mode-Hope Free (MHF) tuning range which limits the spectral coverage of the devices. This typically limits each device to the detection of a single absorption line. It is therefore difficult to detect multiple species, or multiple transitions of the same species, using a single laser.

Alternative optically based techniques have been developed with larger spectral coverage. Broadband sources such as superluminescent diodes or wide bandwidth femtosecond frequency combs have been developed for spectroscopic gas sensing, but they often require high dispersion instruments. What is more, these systems tend to be complex, bulky and expensive, and are therefore unsuited to field applications. Some novel devices have been developed with a much larger MHF tuning range, such as External-Cavity Diode Lasers (EC-DL) and Vertical-Cavity Surface-Emitting Lasers (VCSEL). However, these techniques are typically vulnerable to vibrations or have only been developed in a few restricted wavelength ranges.

There is, therefore, a need to develop a gas sensing device which is capable of monitoring multiple species simultaneously. Additionally, it is desirable for such a device to be portable, robust and low-cost.

1.1 Introduction to MUMAS

Multi-mode Absorption Spectroscopy (MUMAS) is a novel gas sensing technique that combines high-spectral resolution with broad spectral coverage [1–10]. As the name implies, and in contrast to conventional laser absorption spectroscopy which utilises single frequency radiation, a multi-mode laser is used as the source. The spectral resolution originates from the narrow linewidth of each mode in the laser, and the broad spectral coverage is the result of many modes covering a large bandwidth.

The technique uses a conventional absorption spectroscopy approach, in which the ratio of the transmitted to the incident intensity of a laser beam is measured for light propagating through a sample of gas. All longitudinal modes of the laser are scanned, typically across the frequency interval separating adjacent modes, known as the intermode-spacing. In this way, the whole range of the spectrum covered by the broadband output of the laser is interrogated. If, during the scanning of the modes, an individual mode comes into resonance with an absorption transition in the gas, the total transmitted power is reduced. The resulting spectrum is a superposition of the transmission spectrum of each mode and constitutes the MUMAS signature. The location of each absorption feature in time is determined by its location in frequency relative to the scanning modes and their initial frequencies at the start of the scan. Given that the spectral locations of the absorption lines are available from a suitable database, when the laser mode parameters are also known, the resulting MUMAS signature can be calculated and compared with an experimental MUMAS spectrum in order to deduce the properties of the absorbing species.

1.2 Overview of this thesis

This thesis reports work undertaken during development of the MUMAS technique. The three main aims of the work are as follows: firstly, to further understand the operation of MUMAS and subsequently improve the modelling of MUMAS spectra; secondly, to perform MUMAS in the mid-infrared region so as to access the strong fundamental transitions of many species found in this region and; thirdly, to identify and address the limitations of MUMAS when working towards the ultimate aim of designing and manufacturing a robust and portable gas monitoring device based on MUMAS.

Chapter 2 explains the motivation for developing a trace gas sensing device by identifying a range of existing and potential applications. Non-optical methods are briefly mentioned as a solution before the most fundamental optical method, laser absorption spectroscopy, is introduced. The need for a technique with a broad spectral coverage is explained before various existing techniques and enhancement methods are critiqued. Finally, multi-mode absorption spectroscopy is introduced as a viable alternative which presents a simple method to acquire high-resolution spectral information across a broad spectral range.

Chapter 3 presents the theory of MUMAS. The basic theory of operation is discussed and the theory of tuning is considered in detail. Inadequacies of the previous model for the tuning, the *translation-model*, are exposed, and a new model for the tuning, the *expansion-model*, is proposed. The inadequacies of the translation-model only manifest themselves when performing MUMAS with lasers which operate in the mid-infrared region and/or lasers which have many more modes than the multi-mode lasers used for previous work in MUMAS. Thus, this modelling is particularly important for the majority of the lasers used for the work in this thesis. Details and limitations of the translation-model are outlined, and the advantages of the expansion-model are described.

The *MUMAS Equation*, which defines the position of the MUMAS absorption features, and which is also the basis of the expansion-model, is presented. The need for modelling of MUMAS spectra is explained and the modelling process is conceptually described before particular features of the modelling process, in the context of the new expansion-model, are discussed. The chapter concludes with a discussion of the theoretical and performance requirements of a multi-mode laser for a MUMAS application.

Chapter 4 is the first of three chapters detailing the experimental results. The first mid-infrared MUMAS spectrum obtained using an Interband Cascade Laser (ICL) is presented. This provides access to the strong fundamental transitions found in this region, which subsequently improves the sensitivity of the technique. These devices are physically small and have low power requirements, thus making them suitable for gas sensing applications in the field. The apparatus and experimental method used to perform MUMAS is described, and the fitting procedure which allows the MUMAS model to be used to make quantitative measurements of gas concentration is explained. A new method is developed for measuring the individual mode-linewidths which uses pressure broadening of lines from spectra with widely spaced absorptions. The improvements of the new model, the expansion-model, are demonstrated before the large tunability and wide spectral coverage of these ICL devices are demonstrated. A multi-species spectrum of trace amounts of methane, acetylene and formaldehyde is obtained in order to demonstrate the multi-species capability of the technique. The Minimum Detection Limit (MDL) of the technique is then investigated. Finally, ICLs with a wider intermode-spacing are used to obtain MUMAS spectra of trace amounts of methane in atmospheric pressure, thus demonstrating the potential for highly sensitive, multi-species detection using a single multi-mode laser source. The chapter concludes with a brief discussion of the limitations of the technique at this stage in the thesis.

The work in chapter 5 demonstrates the first application of a Quantum Cascade

Laser (QCL) to MUMAS, also carried out in the mid-infrared region of the spectrum. Multiple transitions of the NO molecule are detected over a large bandwidth using this commercially available multi-mode device. Additionally, in the presence of laboratory air containing water vapour, transitions of H_2O are simultaneously recorded, thereby demonstrating the ability to distinguish interfering species in the gas sample. A new method is developed for measuring the individual mode-linewidths which uses pressure broadening of the MUMAS spectra. The commercially available QCL used for the work in this chapter extends the technique to the $5-6$ µm region. The Mode Fractional Power (MFP) of the modes during scanning is introduced as an important concept in the interpretation of MUMAS spectra. The key demonstration is that MUMAS can be applied using a commercially available QCL device, one which exhibits not only strong variations across the spectral intensity distribution when the modes are not being scanned but also significant changes in the MFP during the scan over the intermode-spacing. It is also shown that MUMAS data can be obtained at fast scan rates, thus enabling gas sensing with short measurement times. This is important for applications in rapidly changing environments or for active process control.

Chapter 6 describes further developments of the technique in the near-infrared region of $1-2$ µm. An alternative detection scheme, *balanced ratiometric detection*, is introduced and the advantages of this scheme are described and demonstrated. Furthermore, the chapter describes the modifications to the modelling code which takes into account the variation of the laser intensity envelope as the modes are scanned in frequency. By relaxing the restriction that the laser intensity envelope must be constant, it opens up the possibility of having a much wider selection of multi-mode lasers available for performing MUMAS. The work in this chapter demonstrates the first MUMAS spectrum obtained at atmospheric pressure using a commercially available laser. Finally, MUMAS spectra obtained at a range of temperatures demonstrate the ability to perform thermometry

using MUMAS.

Chapter 7 draws conclusions from the thesis as a whole before suggestions for further development of the MUMAS technique are discussed in chapter 8. Development of a portable MUMAS device, extension of the balanced ratiometric detection scheme to the mid-infrared region, using MUMAS in a multi-heterodyne configuration, and measurement of relaxation dynamics in excited species are all considered in turn.

Chapter 2

Background

2.1 Overview

This chapter begins by explaining the need for a gas sensing device. A range of existing and potential applications are explored and the key requirements of such a device are listed. Laser absorption spectroscopy is introduced as a powerful method which is able to meet many of these requirements. The principal method of gas detection, Tunable Diode Laser Absorption Spectroscopy (TDLAS), is presented, and the benefits and limitations of this technique are discussed. The need for a technique with a broad spectral coverage is explained, before various existing techniques are critically examined. Previous work on MUMAS is outlined, and the work presented in this thesis is introduced.

2.2 Optical gas sensing

Gas detection is of great importance in a wide range of applications, both scientific and commercial.

Early applications were motivated by safety concerns, and progress was stimulated by tightening legislation [11]; sensing devices were required for detecting toxic or flammable

species, particularly in the petrochemical industry [12], and for pollution control in cities where high levels of certain gases can cause respiratory problems [13, 14]. Since then, a wide variety of other potential applications have been identified. The required characteristics of each gas sensing system are dependent upon the application and therefore factors including the required sensitivity, typical response time, operating environment and operational lifetime have to be considered when designing a gas sensing device.

As industrial processes have increased in variety and complexity, so too has the need for robust gas monitoring systems to both optimise these processes and also to provide quality assurance [15]. Levels of feedstock can be altered, and the intermediates, which may be varying on short timescales, can be studied to maximise product yield.

Atmospheric science and modelling depends on data obtained from gas monitoring [16]. Models can be improved by obtaining additional data from various locations around the globe. There is therefore a need for a relatively inexpensive gas sensing device to be widely and remotely deployed. Furthermore, more complex monitoring schemes may have the potential to provide insights into the fundamental reaction pathways in the atmosphere, further aiding climate models [17, 18].

The main sources of atmospheric pollutants are the by-products of industrial processes and the emissions from traffic and agriculture [15]. In addition to monitoring the gases in the atmosphere, it is important to target these large-scale, localised sources of harmful emissions with gas monitoring and abatement systems which can be optimised to reduce the emissions at source. When attempting to mitigate anthropogenic climate change, the economic viability of carbon abatement technologies such as Carbon Capture & Storage (CCS) will have to consider the cost of long-term monitoring of CO_2.

Air pollutants are detrimental to human health and therefore environmental monitoring is essential for regulation and control of harmful emissions [19–21]. In order to

effectively regulate these emissions, a standardised method of monitoring is required to avoid problems such as a mismatch of scales or sensitivity to an insufficient range of species from certain devices.

A breath test device for the purpose of identification and quantification of species in a patient's breath would be a large breakthrough in clinical diagnosis [22, 23]. The matrix of breath is a mixture of nitrogen, oxygen, carbon dioxide, water, inert gases, and trace volatile organic compounds. Abnormal concentrations of these species in a patient's breath can be indicative of a particular disease [24, 25]. In addition, the concentrations of certain species in a patient's breath can also be used for real-time monitoring of oxygen consumption during critical care [26].

Traditional, non-optical methods of sensing and monitoring gaseous species include gas chromatography [27] and mass spectrometry [28]. They both have high sensitivity and selectivity, however, they require sampling which precludes any real-time or non-invasive sensing. Furthermore, the equipment is generally expensive and bulky. Other low-cost, robust sensors include calorimetric methods such as pellistors, and devices based on electro-chemical properties of metal oxide semiconductors [29], but these either have problematic cross-response to different species or have a slow recovery time, hence precluding any high-speed monitoring. They also require particular operating conditions, can become contaminated by non-target species, have limited lifetimes and there are zero-drift issues. Despite these limitations, there are some applications to which each of these devices are particularly well suited. However, they normally target one particular species and therefore different devices are required for multiple species.

Optically based sensors are an attractive alternative for gas sensing as they overcome many of the limitations of other techniques and also have numerous superior performance characteristics. Optical absorption techniques provide a direct, quantitative measurement of the properties of a gaseous sample. Furthermore, as the properties of the gaseous

sample are directly probed, and also by self-referencing the output of the optical source, a device can be made resistant to drift and hence be calibration-free. In addition to this, every species and their isotopic variations have a characteristic absorption spectrum - a 'fingerprint' that is unique to that species. This provides the possibility of high-selectivity, contingent upon the device having zero-response to the other, non-targeted constituents of a gas sample. This selectivity extends to particular absorption transitions belonging to a targeted molecule and therefore individual spectral lines of the same species can be directly identified if the aim is to study a particular absorption transition. Another key benefit of optical techniques is that they are non-invasive, yet allow in-situ detection. They can be used to make measurements in a situation where the system would otherwise be perturbed by the physical imposition of the sensor, such as in a flame [30]. Similarly, they can be deployed in harsh environments where a physical sensor would otherwise be damaged such as in the boiler exhaust of a pulverised-coal-fired power plant [31]. A further key benefit of optically based sensors is their fast time-response which enables real-time monitoring of the properties of rapidly varying gaseous systems [32, 33].

A gas monitoring device would ideally have the following properties: be small, robust and non-invasive; have low fabrication costs; have high resolution; operate over a broad bandwidth so as to target multiple species with the same device; have high-selectivity; have reasonable output power yet have low power requirements; have a fast time-response and have high immunity from vibrations, temperature fluctuations and other noise sources. These factors would be prioritised in a different way for different applications, and ultimately the disposable finances for an application will determine the technology of choice. In the gas-sensing and monitoring market, optically based methods are positioned in a particularly wide gap between the expensive techniques, which are highly sensitive but have slow-sampling and are not real-time – they require post-analysis with laboratory equipment, and the low-cost techniques, which are typically small and in-situ but may

have inconvenient operating conditions and inferior performance. Furthermore, other than a characteristic absorption spectrum, the technique does not require the target species to have any distinctive properties. This means that the device could, in principle, be extended to detect multiple species. This would avoid the need for a discrete device for each target species or having each device based on a different technique with dissimilar operating conditions, mismatched quantitative accuracy and precision and differing calibration procedures.

2.3 Laser absorption spectroscopy

Laser absorption spectroscopy can be applied to the majority of gaseous species, and this allows widespread application. The basic concept is to measure the absorption spectrum of a gaseous sample, from which certain gas properties can be derived. If the frequency of the electromagnetic radiation is resonant with the transition between two quantum states of the species, absorption occurs, resulting in the removal of a photon from the light field and, in turn, the excitation of a single molecule from the lower- to the upper-state.

In practice, a monochromatic beam of light from a laser operating on a single longitudinal mode passes through a gaseous sample, and the incident and transmitted intensities of the laser are monitored and recorded. The frequency of this longitudinal mode is tuned, or 'scanned', so that a particular segment of the spectrum is interrogated. If there are resonant transitions in this frequency-segment, the transmitted intensity will be attenuated. The amount of attenuation is given by the Beer-Lambert Law, equation 2.1, where ν is the frequency, $I_T(\nu)$ and $I_0(\nu)$ are the transmitted and incident intensities, respectively, $\sigma(\nu)$ is the absorption cross-section, N is the number density of

the absorber, and l is the path length of the propagation through the sample [34].

$$I_T(\nu) = I_0(\nu)\, e^{-\sigma(\nu)Nl}\,. \tag{2.1}$$

The exponent, $\sigma(\nu)\,Nl$, is known as the absorbance. In a sample containing many species, the absorbances from each species are linearly combined, and the negative of this summation is then exponentiated to calculate the total absorption spectrum.

Each species will have many quantum states, and the many transitions between these states will each give rise to a resonant absorption. The absorption cross-section of each of these must be calculated or measured. Furthermore, several broadening mechanisms, which are described in section 2.3.2 below, will cause these absorption features to have a finite spectral width. It is common for the absorption features to spectrally overlap, and therefore, in the same way that absorbances from multiple species must first be linearly combined, it is also important to linearly combine all the overlapping absorbances from a particular species before exponentiating to calculate the total absorption spectrum.

The profile of each of these spectral lines will be determined by the various broadening mechanisms applicable to that absorption (section 2.3.2), and each spectral line will also have a magnitude, or *line-strength*, which is described by the integral over the spectral line (section 2.3.1).

2.3.1 Line-strength

The strength of a given absorption line can be characterised by its integrated line-strength, S, given by equation 2.2.

$$S = \int_0^\infty \sigma(\nu)\, d\nu\,. \tag{2.2}$$

For the transition between two isolated molecular energy states, i and f, with equal

degeneracy, this line-strength is determined by the initial population density of the lower- and upper-states, N_i and N_f respectively, and the transition probability which is represented by the Einstein coefficient of stimulated absorption, B_{if}. This is described in equation 2.3 [35, 36].

$$S_{if} = \frac{h\nu}{c} B_{if} \left(N_f - N_i\right). \tag{2.3}$$

Assuming thermal equilibrium, the initial population densities, N_i and N_f, are determined by the Boltzmann distribution. The number density of molecules in state i, at temperature T, is given by equation 2.4, where J_i is the rotational quantum number of state i, E_i is the energy of state i and N is the total number density.

$$N_i = \frac{N}{Q}(2J_i + 1)e^{-E_i/k_B T}. \tag{2.4}$$

The partition function, Q, is defined by equation 2.5:

$$Q = \sum_i (2J_i + 1)e^{-E_i/k_B T}. \tag{2.5}$$

The Einstein coefficient of stimulated absorption is given by equation 2.6, where ϵ_0 is the permittivity of free space.

$$B_{if} = \left[\frac{8\pi^3}{(4\pi\epsilon_0)3h^2}\right] |\mu_{if}|^2 . \tag{2.6}$$

The transition dipole moment, μ_{if}, describes the quantum mechanical probability of a particular transition occurring and is given by equation 2.7, where ψ_i and ψ_f are the wavefunctions for the lower- and upper-states, $\vec{\mu}$ is the dipole moment vector between

these states, and the integration is carried out over all of space, τ.

$$\mu_{if} = \int \psi_i^* \vec{\mu} \psi_f \, d\tau \,. \tag{2.7}$$

2.3.2 Broadening mechanisms

When observing the absorption features from any spectroscopic technique, each resonant absorption will have a finite spectral width. This width arises from a combination of several effects [35]. Mechanisms that cause all molecules within the sample to affect the linewidth in the same way are known as homogeneous, and will typically result in a Lorentzian lineshape, whereas mechanisms which cause an effect that varies from one molecule to another are described as inhomogeneous, and typically result in a Gaussian lineshape.

Natural broadening

Natural broadening, ubiquitous to all spectral features, is a fundamental limit on the minimum spectral width of a transition, and arises from the *Uncertainty Principle* [37]. The Uncertainty Principle defines a reciprocal relationship between the uncertainties in the lifetime and energy of a state whereby less uncertainty in the lifetime of a state results in more uncertainty in the energy of the state and hence increased broadening of a transition involving this state. The finite lifetime results from the spontaneous emission of a photon from the upper-state of a transition, and is therefore related to the Einstein A-coefficient. The relations between the Einstein coefficients, A_{if} and B_{if}, are given by equations 2.8a and 2.8b [38], where g_i is the degeneracy of the i$^{\text{th}}$ state, and ω_{21} is the

resonant frequency for this transition.

$$\frac{A_{21}}{B_{21}} = \frac{\hbar\omega_{21}^3}{\pi^2 c^3}\,. \tag{2.8a}$$

$$\frac{g_1}{B_{12}} = \frac{g_2}{B_{21}}\,. \tag{2.8b}$$

The average lifetime of the upper-state is the reciprocal of the Einstein A-coefficient. From equation 2.8a, the Einstein A-coefficient has an ω^3 dependence, and therefore transitions with a higher resonant frequency will have more broadening. This means that natural broadening will be more prominent for spectral features found in the UV and visible range of the electromagnetic spectrum, and that natural broadening of infrared features will be less prominent. Indeed, it is usually necessary to perform a Doppler-free measurement at low pressure in order to observe the natural broadening of infrared transitions [39].

Pressure broadening

Pressure broadening is another contribution to the overall linewidth, and it is especially prominent at higher pressures. It originates from collisions between the species in the sample which subsequently leads to the phase of the electric-field oscillation suddenly changing, and is thus also known as collisional broadening. However, a collision in the classical sense is not strictly necessary, and the electric field from a nearby species is also sufficient to distort the wavefunction and cause a broadening of the transition. Pressure broadening is a homogeneous effect and results in a Lorentzian lineshape, $g_L(\nu - \nu_0)$,

given by equation 2.9, where $\Delta\nu_L$ is the broadened width.

$$g_L(\nu - \nu_0) = \frac{1}{2\pi}\left[\frac{\Delta\nu_L}{(\nu-\nu_0)^2 + \left(\frac{\Delta\nu_L}{2}\right)^2}\right]. \tag{2.9}$$

The lifetime effects include both natural and collisional induced processes, and the FWHM of the Lorentzian lineshape, $\Delta\nu_L$, is given by equation 2.10, where A_{if} is the contribution from natural broadening and $\tau_{\text{collision}}$ is the mean duration between collisions.

$$\Delta\nu_L = A_{if} + \frac{2}{\tau_{\text{collision}}}. \tag{2.10}$$

Kinetic theory is used to calculate the mean time between collisions, which is given by equation 2.11, where σ_Q is the collisional cross-section, μ is the reduced mass of the interacting particles, and P is the pressure of the sample. Therefore, the pressure broadened linewidth is proportional to the pressure and inversely proportional to the square root of the temperature.

$$\frac{1}{\tau_{\text{collision}}} = \frac{\sigma_Q P}{\sqrt{\pi\mu k_B T/8}}. \tag{2.11}$$

Doppler broadening

For low-pressure gases, the largest contribution to the broadening of ro-vibrational spectra is typically Doppler broadening. Doppler broadening arises from a combination of the thermal distribution of species in a sample and the Doppler-effect, and is an inhomogeneous broadening effect. The Doppler-effect describes how a moving body experiences a different frequency of radiation when compared with the frequency of radiation measured in a stationary reference frame. Therefore, the distribution of velocities in a sample results in the transition also having a distribution of resonant

frequencies.

Equation 2.12 defines how the frequency of radiation, ν_a, absorbed by a molecule moving with speed, $\pm v$ (defined as positive away from the radiation source), is related to the resonant transition frequency, ν_{res}.

$$\nu_a = \frac{\nu_{\text{res}}}{1 \pm \frac{v}{c}} \,. \tag{2.12}$$

The species is defined to have a Maxwell-Boltzmann distribution of velocities, $f(v)$, given by equation 2.13, where m is the particle mass and T is the temperature [40].

$$f(v) = \sqrt{\left(\frac{m}{2\pi k_B T}\right)^3} 4\pi v^2 e^{-\frac{mv^2}{2k_B T}} \,. \tag{2.13}$$

Combining equations 2.12 and 2.13 results in a Gaussian lineshape, $g_G(\nu - \nu_0)$, given by equation 2.14.

$$g_G(\nu - \nu_0) = \frac{c}{\nu_0}\sqrt{\frac{m}{2\pi k_B T}} \exp\left(\frac{-4\ln(2)\,(\nu - \nu_0)^2}{\Delta\nu_{\text{Dopp}}^2}\right) \,. \tag{2.14}$$

The FWHM of this distribution, $\Delta\nu_{\text{Dopp}}$, is given by equation 2.15. The Doppler broadened width of a transition is proportional to the square root of the temperature.

$$\Delta\nu_{\text{Dopp}} = \frac{\nu_0}{c}\sqrt{\frac{8k_B T \ln(2)}{m}} \,. \tag{2.15}$$

Laser mode-linewidth broadening

The probing laser will have a finite spectral width, which will, in turn, contribute to the spectral width of the measured absorption features. The mode-linewidth of a laser is strongly linked to the properties of the laser cavity and is found to have an approximately Lorentzian lineshape [41], however, these effects are often eclipsed by sources of technical

noise such as mechanical vibrations, acoustic noise and thermal drift which lead to small changes in cavity length or alignment. Ultimately, the mode-linewidth is typically much smaller than the other broadening mechanisms and will have a negligible effect on the width of the overall spectral absorption features.

Voigt profile

The balance between the different thermodynamic properties of the sample will determine which type of broadening is more dominant. At low pressures, Doppler broadening is the dominant contribution, whereas at atmospheric pressures, the linewidth is dominated by pressure broadening. However, at intermediate pressures, the magnitude of the broadening effects are comparable and therefore the observed lineshape is a combination of both pressure and Doppler broadening effects. The combined lineshape will be a convolution between the individual Gaussian- and Lorentzian-lineshapes, which results in a Voigt-lineshape. The form of the Voigt-function is given by equation 2.16, where x and y are given by equations 2.17a and 2.17b, and where $\Delta\nu_L$ and $\Delta\nu_G$ are the FWHMs of the Lorentzian- and Gaussian-components respectively.

$$g_V = \frac{2y}{\Delta\nu_G \pi}\sqrt{\frac{\ln 2}{\pi}}\int_{-\infty}^{\infty} \frac{e^{-t^2}}{y^2 + (x-t)^2}\, dt\,. \tag{2.16}$$

$$x = \sqrt{\ln 2}\ \frac{2\,(\nu - \nu_0)}{\Delta\nu_G}\,. \tag{2.17a}$$

$$y = \sqrt{\ln 2}\left(\frac{\Delta\nu_L}{\Delta\nu_G}\right)\,. \tag{2.17b}$$

Generation of Voigt profiles for spectral modelling is typically computationally expensive, and therefore approximations are regularly used, such as the one described in

appendix B.

2.4 Tunable diode laser absorption spectroscopy

Lasers were developed in the 1960s with the first demonstration in 1960 by Theodore H. Maiman [42]. The first laser diode device was demonstrated in 1962 by Robert N. Hall [43]. Gordon Gould suggested using a laser for spectroscopy in 1959, before this initial demonstration [44]. It was clear that a monochromatic source of light would be advantageous for obtaining high-resolution absorption spectra. Subsequent development has resulted in laser diode devices becoming readily available, which are compact, robust, operate at room temperature and produce stable, narrow-linewidth, monochromatic light.

Laser diodes are now widely used for laser absorption spectroscopy in a highly established gas sensing technique called Tunable Diode Laser Absorption Spectroscopy (TDLAS). There are many inherent properties of laser diodes that make them particularly suited to laser absorption spectroscopy, and they are discussed below.

Laser diodes are typically small, robust, have reasonable output power yet have low power requirements and have high immunity from vibrations, temperature fluctuations and other noise sources. Therefore, they lend themselves to integration in a portable and robust device. Furthermore, the narrow-linewidth of the light means that high-resolution absorption spectra can be obtained. This, coupled with the ability to accurately control the output frequency of the laser, allows for high selectivity and high specificity. The technique provides a direct measurement of concentration, and as it is non-invasive, it is also not susceptible to poisoning. The high-resolution allows an accurate measurement of spectral lineshapes, thus providing the ability to monitor other properties of the sample such as the temperature, ambient pressure and mass flow [45]. In addition, laser diodes have been demonstrated to have modulation bandwidths of up to 1 GHz [46]. This

facilitates fast scan rates, thus allowing for noise-reduction via averaging on reasonable timescales and also enabling real-time monitoring of the properties of rapidly varying gaseous systems.

In theory, the same technique can be used to probe the absorption spectra of a wide range of molecules, thus precluding the need for a different method for each target species. The main requirement for it to be possible to detect a molecule is that the line-spectrum is resolvable at the Doppler limit, which in practice includes most molecules with five or fewer atoms [11]. In practice, the main limitation to detecting all gaseous species is that reliable diode lasers are not readily available across the full infrared spectrum. There are many suitable lasers in the near-infrared region due to their development within this region for their use in telecommunications (this is the optimum region for telecommunications as it is where both the optimum transmission window for silica optical fibres and the operational wavelength of erbium fibre-amplifiers are found). However, lasers which operate in the mid-infrared region are not as common as near-infrared lasers, and the requirement that the laser spectrum must have a single, stable mode adds additional complexity [47].

Finally, the main disadvantage of single-mode diode lasers is their intrinsic limitation on the Mode-Hope Free (MHF) tuning range. This limits the spectral coverage of the devices, and therefore typically limits each device to the detection of a single species. Further discussion and alternative, broad spectral coverage techniques are discussed in section 2.5.

2.4.1 SNR enhancements

The quality of an absorption spectrum for concentration measurements is often characterised by the Signal-to-Noise Ratio (SNR) of the spectrum. The general criterion for the sensitivity limit is the concentration of the species which gives a SNR of one. Thus,

decreasing the noise of a signal, or increasing the magnitude of the signal relative to the noise, will allow for increased sensitivity.

A commonly employed method of noise reduction is Wavelength-Modulation Spectroscopy (WMS) which, when used with TDLAS, has been reported to achieve minimum detection limits of parts per trillion by volume, pptv [48, 49]. In WMS, the laser is scanned across an absorption feature as before, but a high-frequency wavelength modulation, on the order of kHz, is applied to the laser output [50]. The high modulation bandwidth of diode lasers make these high modulation frequencies possible. An absorption feature causes an amplitude modulation of the signal, and the component of this which is in resonance with the modulating frequency of the laser is obtained using a lock-in amplifier. The amplitude modulation of this signal therefore gives a measure of the absorption feature. The noise-rejection is achieved by encoding the signal in the high-frequency modulation, applying a notch-filter at the modulation frequency via the lock-in amplifier, and hence rejecting the low-frequency noise. Calibration of this absorption measurement is necessary only if one harmonic is monitored, however, calibration-free measurement is also possible by monitoring higher harmonics in order to provide a normalisation which accounts for variations in the laser intensity [51]. An additional benefit of the noise-rejection capabilities of WMS is the improved dynamic range of the signal produced. Direct absorption produces a small signal on a large background whereas WMS produces a zero-baseline signal proportional to the absorber concentration. This reduces the possibility of measurement drift and also alleviates the resolution requirements of the data acquisition device.

Along with reducing noise, the SNR can be enhanced by increasing the magnitude of the signal. The magnitude of the signal is given by equation 2.1, where it is clear that for a given concentration of absorber, either increasing the absorption cross-section or increasing the path length of the light propagation through the sample increases the

magnitude of the signal. When performing TDLAS in the near-infrared region, the absorption lines are typically due to combinational ro-vibrational or overtone transitions. The transitions have cross-sections which are approximately 10^2 to 10^5 times weaker than the fundamental vibrational transitions found in the mid-infrared region. Hence, the magnitude of the signal could be increased by detecting transition lines in the mid-infrared region. However, as mentioned previously, mid-infrared emitting devices are not as readily available as near-infrared emitting devices. An alternative way of increasing the magnitude of the signal strength is to increase the path length of the light propagation through the sample. This can be achieved by simply using a multi-pass cell, or by using one of various enhancement techniques which employ an optical cavity [52].

A relatively simple enhancement technique which uses an optical cavity is Cavity-Enhanced Absorption Spectroscopy (CEAS). This technique directly measures the total, time-integrated intensity of light transmitted by a cavity which is continuously irradiated. A particular technical challenge of this technique is to prevent a cavity fringe spectrum appearing on the absorption spectrum, which is caused by the interference of the many cavity modes which have been excited. Common techniques to remove these interference fringes are to either slightly mis-align the cavity or to rapidly change the cavity length through mechanical vibrations. As mechanical vibrations are usually unwelcome and difficult to eliminate, their usefulness for CEAS makes this technique both relatively simple and particularly attractive for use in robust, highly sensitive gas sensors.

One of the drawbacks of CEAS in this form is that the linewidth of the laser is usually spectrally wider than the width of the cavity modes, which results in a noisy cavity output. An enhancement of this technique is Optical-Feedback Cavity-Enhanced Absorption Spectroscopy (OF-CEAS) which has the effect of reducing the laser linewidth via optical feedback from the cavity into the laser, and hence eliminating the noisy cavity output [53, 54]. As light builds up in the cavity, some also leaks back to the laser. This

in-phase feedback field acts as injection seeding, locking the emitted laser frequency to the resonant cavity mode, and subsequently narrowing the laser linewidth. This selective optical feedback results in the laser frequency locking to successive cavity modes as the driving current is scanned, and hence the laser scans stepwise through the successive cavity modes. This results in a cavity transmission consisting of an envelope of modes whose frequency spacing corresponds to the Free Spectral Range (FSR) of the optical cavity. Spectra resulting from an OF-CEAS system are therefore ready-calibrated for relative frequency. However, the need to maintain the distance between the laser and the cavity to a high precision coupled with the step-wise nature of the scanning adds to the complexity of this enhancement technique.

An additional cavity enhancement technique is Cavity Ring-Down Spectroscopy (CRDS), in which light is injected into an optical cavity and the decay in intensity is monitored [52, 55]. The decay rate provides an indirect measure of the absorption. This technique has much greater sensitivity than CEAS. Greater sensitivity results from the improved dynamic range characteristic of this technique – high accuracy measurements can be made of decay-rates, which is better than detecting a small change on a large signal when measuring direct absorptions. However, CRDS requires higher speeds from the associated electronics and is more prone to noise disturbances from mechanical vibrations.

2.5 Broad spectral coverage

TDLAS is a mature technology that is widely used for selective and quantitative gas monitoring. However, the main limitation of TDLAS is the limited range of MHF tuning inherent to most single-mode lasers, thus limiting the spectral coverage of the technique. This often restricts TDLAS methods to detection of a single species unless, fortuitously, two species have transitions lying within the MHF tuning range. There are two main

reasons why larger spectral coverage is desirable: the possibility of multi-species detection and thermometry.

There are many applications where the ability to simultaneously detect multiple species would be advantageous, a few examples of which are outlined below. For the majority of applications mentioned in section 2.2, the detection of multiple species would be beneficial in order to build up a complete understanding of the system being monitored. During pollution monitoring in atmospheric science, it is necessary to monitor the evolution of multiple species [56, 57]. By monitoring the concentrations of CO and CO_2 in the exhaust gas of a combustion engine, in combination with closed-loop control of the air feed, fuel efficiency can be maximised by ensuring complete combustion [58–60]. In combustion diagnostics, many reaction pathways occur and monitoring the concentrations of the various exhaust gases would help in further understanding these processes [30, 61–63]. In the context of spectroscopic breath analysis for medical diagnostics, monitoring of several species would provide further diagnostic markers for various disease processes, opening up the possibility of convenient, non-invasive, en-masse diagnostics within the population [24].

As well as being able to monitor multiple species, a broad spectral-coverage would also allow multiple transitions from a single species to be monitored, thus enabling temperature measurements to be performed. The potential temperature sensing capability arises because the absorption strengths of a particular species are temperature dependent, and they vary at different rates with temperature. Equation 2.18 illustrates how the intensity ratio, R, of the absorption strengths of a pair of lines is purely a function of temperature [57].

$$R = \frac{S_1(T_{ref}).g(\nu - \nu_1)}{S_2(T_{ref}).g(\nu - \nu_2)} \exp\left[-\left(\frac{1}{k_B}\right)(E_1' - E_2')\left(\frac{1}{T} - \frac{1}{T_{ref}}\right)\right]. \tag{2.18}$$

Two such absorption lines, with transition energies given by E_1' and E_2', can be specifically targeted to maximise the rate of change of their ratio with temperature, and can therefore be used as a high-precision temperature probe. As laser absorption spectroscopy is non-invasive and can be performed remotely, it is possible to take temperature measurements of harsh environments. Furthermore, the ratiometric nature of this technique provides some immunity to fluctuations in laser power or sample concentration.

Both multi-species detection and a temperature probe would have many applications, but the limited spectral-coverage of laser diodes precludes them as a viable option for TDLAS for these applications. However, there are a range of other techniques that have a much broader spectral-coverage with a single device, some of which are discussed below.

2.6 Existing broad spectral-coverage techniques

2.6.1 Multi-transition TDLAS

TDLAS can be expanded to detect multiple transitions, and hence perform multi-species detection or thermometry. The simplest extension is to simultaneously perform TDLAS with many lasers, each tuned to a target transition [64, 65]. It is important that each of these lasers cover the same optical path so that the relative concentrations of species in the sample can be accurately determined. Therefore, the beams from each device are combined before being passed through the sample, and are separated after emerging from it. This multiplexing and de-multiplexing of several lasers and detector systems can be achieved by time-division-multiplexing [56], wavelength-division-multiplexing [64], or frequency-modulation-multiplexing [65]. In addition to these techniques requiring multiple lasers and detectors which increases the cost, the coupling with multiplexing techniques also presents further complexity.

Alternatively, TDLAS can be performed with novel devices which have a much larger MHF tuning range compared with typical single-mode laser diodes. Two such devices are External-Cavity Diode Lasers (EC-DL) and Vertical-Cavity Surface-Emitting Lasers (VCSEL).

The key element of EC-DLs is the use of a diffraction grating as a wavelength selective element [66, 67], which is placed outside the active medium and forms a resonator. By rotating the grating, the resonant wavelength, and hence the frequency, is tuned. A continuous scanning range of 70 nm has been reported [68]. The main limitations are the vulnerability to vibrations which comes with a multi-component device, and the severely restricted tuning rate which is effected by the mechanical rotation of the grating.

In contrast to conventional diode lasers, which emit radiation from one edge of their active layer along the axis of the cavity formed in the plane of this layer, VCSELs radiate from a surface perpendicular to this plane [69]. Their structure consists of an inner cavity containing the quantum wells, which is the active medium, surrounded by electrically conductive layer stacks which form the laser mirrors which provide optical feedback. The result is a particularly thin cavity, of the order of 1 µm, and therefore the FSR is relatively large. The FSR is often larger than the gain bandwidth of the active medium and therefore there is only a single permitted mode within the gain bandwidth and hence there is no threat of mode-hopping. Large, continuous, MHF tuning ranges are thus possible, with tuning ranges up to 100 nm being achieved [70]. Simultaneous detection of C1 to C4 alkanes in a multi-component gas mixture has subsequently been demonstrated [71]. The scanning rates on the order of MHz are also superior to EC-DLs. However, VCSELs have only be developed in a few restricted wavelength ranges and their output powers tend to be low.

A promising technology with high-tunability (up to 50 nm) is external cavity devices based on MEMS technology (Microelectromechanical Systems), which is also able to

produce fast response, high accuracy and enhanced mechanical stability [72]. MEMS facilitates external cavities at particularly short lengths (< 100 µm), and thus, by extension, MHF tuning over wide spectral regions. However, along with their high cost, the packaging and integration present extreme difficulties in handling, optical alignment and attachment, and may cause mechanical, electrical and thermal stability problems.

2.6.2 Broadband spectroscopy

Instead of tuning a monochromatic laser source, broad spectral-coverage from a single device can be achieved simply by using a source emitting a broadband continuum. A source with broad spectral-coverage provides access to many molecular transitions, thus enabling multi-species sensing with a single device. Compact broadband sources have been developed with successful application to spectroscopy, such as Super-luminescent Light Emitting Diodes (SLEDs) [73, 74], however, their inherent poor spectral brightness often limits their sensitivity. By simultaneously monitoring a wide spectral range with a broadband light source, there is no need to tune the output of the device and therefore the associated limitations of tuning are avoided. There is a range of broadband spectroscopic techniques which, depending on the detection scheme, can be grouped into either dispersive or non-dispersive techniques.

In non-dispersive techniques, the radiation that passes through the sample is observed in two different, wide spectral windows, which are defined by optical notch-filters. The windows are specifically chosen so that one is free from absorptions of any target or interfering species, known as the reference window, and the other contains an absorption band of the target molecule, known as the signal channel. The absorption is found by calculating the ratio of the signal and reference channel, and a measurement of the concentration of the absorbing species can be determined from this. This technique requires small absorptions of the target species, and also requires the light intensity

fluctuations to be correlated across both detection windows. To avoid cross-response, the technique also requires the fortuitous situation whereby there are windows available which exclusively contain absorptions from the target species. Although this situation is rare, when the spectral information favours the technique, it can lead to simple, cheap, and reliable devices, capable of long periods of unattended operation. One such example is the Li-Cor open path CO_2/H_2O analyser which operates in the 4.2 µm measurement band [75]. In general, these sensors have poor selectivity, and what's more, the poor noise characteristics cannot be overcome by modulation techniques due to the limited electronic modulation frequencies.

In contrast to non-dispersive techniques, where the signal is just the spectrally integrated intensity in each window, dispersive techniques examine the spectral structure of the broadband radiation which emerges from a gas sample. A dispersive element is used to enable an absorption spectrum to be recorded with high spectral-resolution and therefore light of different wavelengths are spatially separated so that the intensity as a function of wavelength can be monitored. The high spectral-resolution and broad spectral coverage of this technique allows multi-species detection. However, the dispersive elements and detection schemes are typically complex, bulky and expensive, and due to the requirement for wavelength dispersion the resolution is inherently limited by the resolution of the dispersive elements [76].

2.6.3 Programmable mid-infrared source for gas sensing (MIREGAS)

A novel technique currently being proposed, known as MIREGAS (Programmable Mid-Infrared Source for Gas Sensing), involves utilising wide-band SLEDs which operate in the mid-infrared region in combination with a Si-based photonic integrated circuit (PIC) filter to provide tunability to different spectral bands [77]. In this proposal, recently developed SLEDs will cover the $2.7 - 3.5$ µm range with each particular device having

a spectral coverage of approximately 100 nm [78, 79]. A Si PIC filter allows 2.5 nm and 5 nm bands to be selected from the emission spectrum of the SLED light source. This novel PIC-filter is re-programmable and also has the capability of fine tuning the filtering response up to 1 nm resolution. This enables high specificity through probing of single absorption lines. There is a proposal for this technique to be validated in several key applications including: building ventilation; process control and safety; and the monitoring of industrial asset condition, emissions, and gas leakage [**miregasH2020**].

The potential to customise a spectral response to match any wanted set of absorption lines makes this a promising technique for gas sensing in the mid-infrared region. However, despite operating in the mid-infrared region, the spectral range of the technique is currently limited to $2.7 - 3.5$ µm which precludes sensing of molecules which have molecular absorption lines at longer wavelengths. Additionally, due to its resolution of 1 nm, it is yet to be demonstrated how discriminating it will be to other interfering species in these wavebands. Furthermore, the sampling nature prohibits any open-path sensing and the relatively low output powers of the SLEDs of ~ 1 mW makes various cavity enhancement techniques with long path lengths impractical. Despite these drawbacks, the device promises to be robust and has an anticipated low cost (300 €/unit with 5000 units/year), thus facilitating widespread deployment. It is noted that the proposed low-cost demonstrates the potential, in general, to substantially decrease the unit price when manufacturing large quantities of devices, and this principle of economies-of-scale could benefit the affordability of other similar gas sensing techniques, including MUMAS.

2.6.4 Correlation spectroscopy

Irregular laser fluctuations due to mode competition or mode hops restrict the bandwidth and performance of TDLAS, and this disadvantage represents the main drawback of the technique. Correlation spectroscopy circumvents this fundamental problem of unruly

laser fluctuations in the data processing.

In gas correlation spectroscopy, the output of a multi-mode laser source, or other broadband source, is split with half the light passing through the test-cell containing the sample under investigation, and the other half passing through the reference-cell which contains a well characterised sample of the target species. As with TDLAS, the laser spectrum is tuned across a segment of the spectrum, and the intensity of the transmitted radiation from both the reference- and test-cell is simultaneously recorded. The total laser intensity, before passing through the cells, is also monitored to correct for any laser power variations. The transmitted radiation contains absorption features arising from the species in each cell, and also has variations in intensity caused by arbitrary laser fluctuations and/or optical fringes. By analysing the correlations between the two signals, it is possible to discern which signals arise from absorptions due to the target species. The ratio between the magnitude of the correlated components provides a measure of the concentration of the target species [80, 81].

The narrow mode-linewidth of the unstabilised Fabry-Perot laser source results in high-sensitivity and high-selectivity. The technique can also be extended to multiple species by having multiple reference cells, one for each target species [82]. In addition, the technique can be used in combination with modulation techniques such as WMS to improve the noise characteristics and hence the sensitivity of the technique [83]. As the technique is a direct comparison with real absorption features, detailed spectral knowledge is not required, thereby greatly simplifying the data processing. Furthermore, the immunity to laser fluctuations, and by extension immunity to mechanical vibrations, make this a highly robust and relatively low cost technique. However, the main disadvantage of the technique is the inherent need for a reference cell containing a well characterised sample of the target species. Furthermore, the sample must also be at the same temperature and pressure as the unknown sample, which precludes applications to varying or unknown

environments.

2.6.5 Frequency-comb spectroscopy

Optical Frequency Combs (OFCs) are optical spectra consisting of a series of equally spaced laser modes, for which John L. Hall and Theodor W. Hänsch were awarded the Nobel Prize in Physics in 2005. Due to their high-spectral resolution and precision, OFCs have been widely used in metrology [84], for the measurement of physical constants [85] and are an integral part of an optical atomic clock [86]. The high-spectral resolution provided by each laser mode coupled with the extremely broad spectral coverage provides a particularly attractive light source for performing high-resolution multi-species spectroscopy. Consequently, OFCs have been used for spectroscopy, with a range of detection schemes being used to exploit their impressive properties [87–92].

Mode-locked femtosecond lasers are used to produce an optical frequency comb through the interference of periodic femtosecond pulses in a temporally coherent pulse train. Figure 2.1a shows a periodic train of short pulses which is emitted by a mode-locked laser. The temporal separation of the emitted pulses is given by the laser cavity round-trip time, $\Delta t_{rep} = 2L_c/v_g$, where L_c is the cavity length and v_g the mean group velocity [94]. Figure 2.1b shows the Fourier-transform for this train of pulses which reveals that the frequency spectrum comprises a series of discrete frequencies, with the frequency spacing given by the repetition rate of the laser cavity round-trip time, $\Delta\omega_{rep} = 1/\Delta t_{rep}$. The repetition frequency can be determined with high accuracy using a fast photodiode and so the absolute frequencies of each mode can be known to better than one part in 10^{15} [95]. The duration of the individual pulses, Δt_{env}, determines the spectral width of the comb. Individual pulses are typically in the range of 1 to 10 fs giving the comb a bandwidth, $\Delta\omega_{env} = 1/\Delta t_{env}$, of 100 to 1000 THz.

In reality, with this system alone, there will be a small offset, ω_0, to the frequency

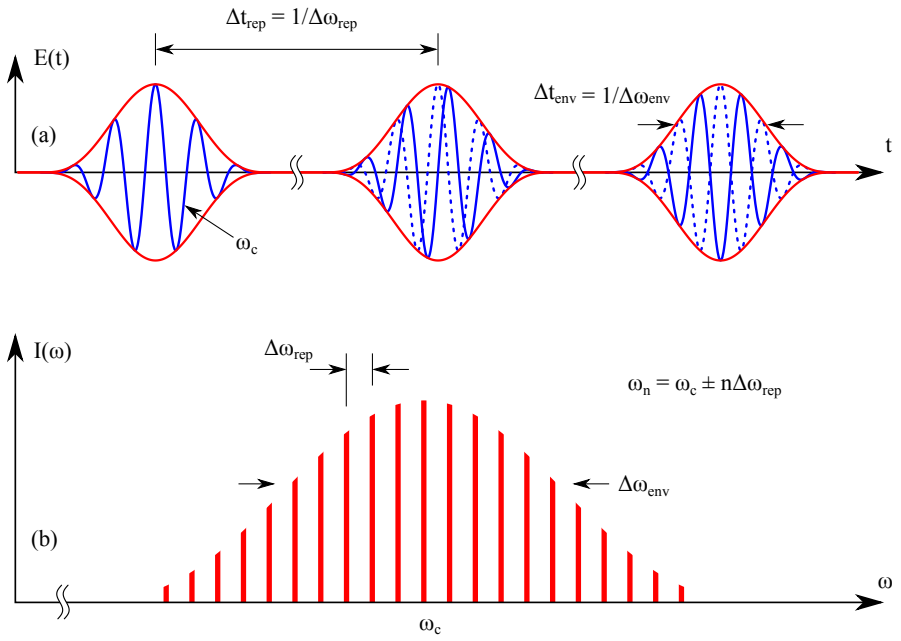

Figure 2.1: A schematic of optical frequency comb generation from [93]. Panel (a) shows the time domain description of a train of three extremely short (fs) pulses emitted by a mode-locked femtosecond laser. Panel (b) shows that the corresponding frequency spectrum consists of a comb of extremely narrow modes. The spectral width of the comb is dependent on the pulse duration, $\Delta\omega_{env} = 1/\Delta t_{env}$, while the pulse repetition frequency, $\Delta\omega_{rep}$, which is dependent on the cavity length, L_c, gives the spacing between the modes.

of all modes, and their absolute frequencies will be ill-defined. This offset is caused by a difference between the group and phase velocities of the train of pulses, v_g and v_p respectively, which, rather than the pulses being identical, leads the each sequential pulse in the train being shifted by an amount known as the Carrier-Envelope Offset (CEO) frequency, ω_0. If the spectral width of the comb spans more than an octave, a self-referencing technique can be used to fix this offset, and even set it to zero. The self-referencing technique works by frequency doubling the spectrum, and observing the heterodyne signal between the highest frequency mode in the original comb and the proximal mode in the frequency-doubled comb. The frequency beat will be ω_0. This CEO frequency is stabilised by having a control feedback loop into the cavity.

These high-resolution, broad spectral-coverage lasers can be used to perform Direct Frequency Comb Spectroscopy (DFCS) of multiple species, where the resolution is determined by the frequency interval separating adjacent modes. Additionally, the high spectral brightness of OFCs improves the SNR experienced by detectors [96]. Furthermore, sensitivity enhancements can be achieved by using a modulation/lock-in detection scheme that samples at exactly the repetition rate of the mode-locked laser source, thus evading the main sources of noise [97].

The intensity of the OFC which passes through the sample is a superposition of the intensity of each individual mode, and a dispersive element is normally required to determine which group of modes caused an absorption feature. It is possible that high-resolution spectrometers are able to probe individual frequency components in the comb, however, given the typically narrow intermode-spacing, the spectral resolution achievable with such systems is usually insufficient to resolve the individual modes. Alternatively, Fabry-Perot etalons can provide much higher resolution, but the multiple modes and insufficiently small free spectral range of the etalon cause many overlapping orders, hence restricting the resolution. Therefore, to achieve sufficient resolution, two orthogonal spectral dispersers, such as a grating and a Virtually-Imaged Phased Array (VIPA), can be used to provide sufficient 2D spatial separation of the individual modes [87].

Frequency comb spectroscopy is a powerful technique which is able to provide extremely high resolution measurements over a wide spectral range and on short timescales. Nonetheless, and similarly to other broadband techniques, the combination of a large stabilised optical frequency comb and a high-resolution disperser causes this technique to be highly complex and expensive. This makes it unsuitable for field work or use in hostile environments, and is therefore an unrealistic option for a widely deployable, multi-species, spectroscopic device.

2.6.6 Multi-heterodyne spectroscopy

When performing spectroscopy with a multi-mode laser, the intensity of the radiation which passes through the sample is a superposition of the intensity of each individual mode. When an absorption occurs, it is therefore impossible to determine which mode is being absorbed. Without a spectrometer to selectively monitor the intensity of particular modes, the specific mode involved in the absorption feature is unknown. In gas correlation spectroscopy, described in section 2.6.4, this is circumnavigated by not requiring explicit spectral information of the target species, but instead by looking for correlations between a gas sample of the target species and a well characterised reference sample of the target species.

Multi-heterodyne spectroscopy is able to disentangle this sum of mode intensities into the intensities for each particular mode. By down-converting a multi-mode laser spectrum to the radio-frequency (RF) domain using an optical multi-heterodyne process with another multi-mode laser used as the local oscillator, the transmitted intensity of each individual mode can be observed in the RF spectrum. A fast photodiode is used to detect the transmitted intensity and the photocurrent containing the multi-heterodyne signal is analysed by an RF spectrum analyser. The intermode-spacing for the two multi-mode lasers must be slightly different, and their outputs must also be phase-locked. This will result in a comb of heterodyne signals in the RF spectrum, with the modes separated by the difference between the intermode-spacings of the two multi-mode lasers.

The number of distinct frequencies in the heterodyne signal that can be detected, N_{H}, is limited by the bandwidth of the fast detectors, $\Delta\nu_{\mathrm{rf}}$, and is given by equation 2.19, where $\Delta\left(\Delta\nu_{\mathrm{mode}}\right)$ is the difference between the intermode-spacings of the two lasers.

$$N_{\mathrm{H}} = \frac{\Delta\nu_{\mathrm{rf}}}{\Delta\left(\Delta\nu_{\mathrm{mode}}\right)}\,. \tag{2.19}$$

A smaller difference between the intermode-spacings of the two lasers will result in a larger spectral density of heterodyne signals and hence more heterodyne signals for a given detector bandwidth. More heterodyne signals means an increased number of mode intensities being recorded and therefore a broader spectral coverage of the technique. However, there is also a lower bound on the difference between the intermode-spacings. This is necessary in order for the heterodyne signals to be resolved. Both the linewidth of the modes of the two frequency combs and the frequency stability of the modes will contribute towards the linewidths of the heterodyne signals. Narrow linewidth heterodyne signals will mean that the difference between the intermode-spacings can also be lower whilst still resolving each heterodyne signal, and hence an increased spectral density of resolved heterodyne signals is possible. In summary, the spectral coverage of this technique is increased by having a higher bandwidth of the fast detector and a smaller difference between the intermode-spacings which is facilitated by having narrow linewidths for the modes of the two lasers.

Multi-heterodyne spectroscopy has been realised with a pair of optical frequency combs, described in section 2.6.5 [98]. Fine control of the intermode-spacing for each frequency comb is enabled by the fine control of the repetition rate of the laser-cavity round-trip time. An optical frequency comb with $155,000$ individual frequency-comb lines, spaced by 100 MHz intervals and spanning from 1495 to 1620 nm, was used to probe a sample of hydrogen cyanide. The technology has also been used outside the laboratory thereby demonstrating the improving portability of the technique [99, 100]. Although this technique has a high-resolution and broad spectral coverage, it still suffers from high complexity and expense.

Multi-heterodyne spectroscopy has also been demonstrated in the much more portable situation of using two Fabry-Perot Quantum Cascade Lasers (FP-QCLs) mounted on the same device. Fine control of the intermode-spacing for each of these lasers was not

practically possible. Fortuitously, however, each laser had slightly different intermode-spacings [101]. The main drawback when compared with multi-heterodyne spectroscopy using OFCs is that both the linewidths and frequency jitter of the individual modes are much larger. This means that the difference between the intermode-spacings of the two lasers must be larger for the heterodyne signals to be resolved. The resulting spectral density of heterodyne signals is decreased, resulting in fewer modes being probed for a given detector bandwidth and therefore less spectral coverage with the technique. Despite this, multi-heterodyne spectroscopy with two FP-QCLs is a promising technology, which is able to produce highly-resolved spectra covering a broad spectral range. One limitation is the upper bound on the bandwidth of the fast detectors, which directly impacts the spectral coverage that is possible. Furthermore, a significant limitation is the difficulty in acquiring two phase-locked, narrow-linewidth, FP-QCLs with slightly different intermode-spacings. To solve this, a method has been developed for ensuring phase stability between two multi-mode lasers which involves locking each multi-mode laser to two separate, frequency stable, single mode lasers [102]. The resulting beat notes are used to measure any time or phase shifts in the multi-mode lasers and the error signal is used to compensate for any drifts. However, this phase-locking solution requires four separate lasers and thus presents further complexity.

2.7 Multi-mode Absorption Spectroscopy (MUMAS)

Multi-mode Absorption Spectroscopy, MUMAS, uses a conventional absorption spectroscopic approach in which the ratio of transmitted to incident intensity of a laser beam is measured for light propagating through a sample of gas. In the case of MUMAS, all longitudinal modes of a multi-mode laser are scanned, typically across the frequency interval separating adjacent modes, which is known as the intermode-spacing. Whenever

an individual mode comes into resonance with a molecular absorption transition, that mode will be partially absorbed. The resulting MUMAS spectrum is a superposition of the transmission spectra of the individual modes in the laser comb. In this way, the entire range of the spectrum covered by the broadband output of the laser is interrogated.

The resolution of the technique is limited by the individual linewidths of the modes, which are typically narrow. As a consequence, this novel technique offers a simple method to acquire high-resolution spectral information on multiple transitions, and hence multiple species, across a broad spectral range. A subsequent modelled fit to the MUMAS spectrum allows identification and a quantitative measurement of a sample species.

MUMAS only requires a single laser and a simple detection scheme, and therefore presents a viable alternative to TDLAS multiplexing methods which require multiple lasers and multiple detectors in order to achieve broad spectral coverage. In contrast to broadband spectroscopy, MUMAS does not require complex dispersive elements, which are typically expensive. Furthermore, unlike gas correlation spectroscopy, MUMAS does not require a reference cell of the target species and can detect species at unknown pressures and temperatures. Finally, the laser sources for MUMAS are inexpensive and more readily available when compared to those used for direct frequency comb spectroscopy and multi-heterodyne spectroscopy.

The first demonstration of MUMAS was reported in 2008. For these initial proof-of-concept experiments, the transitions in the A-band $b^1\Sigma_g^+ - X^3\Sigma_g^-$ of molecular oxygen were detected using a commercially available multi-mode Fabry-Perot diode laser operating around 760 nm [1]. Quantitative measurements using the same diode laser were performed. The pressure and temperature of oxygen samples were simultaneously measured over a range of conditions, with both sets of measurements found to have a precision better than ± 2 % [3]. In order to improve the sensitivity and SNR, MUMAS was subsequently combined with additional sensitivity enhancement techniques such as CEAS and WMS [4].

MUMAS was demonstrated in the near-infrared for the first time using an Er/Yb:glass micro-cavity laser in order to access the spectral information of different species [2]. The new device used in this work also demonstrated the flexibility of the technique to different laser sources. It was clear that the key benefit of MUMAS was the broad spectral coverage and, by extension, the potential to achieve multi-species detection using a single device. The multi-species capability of MUMAS was first demonstrated using a custom-built diode-pumped Er:Yb:glass laser operating around 1565 nm to detect C_2H_2, N_2O, and CO [5]. A similar laser subsequently demonstrated the simultaneous detection of CO_2 and CO in engine exhaust [6].

The technique was extended to the mid-infrared region using a source of multi-mode mid-infrared radiation based on Difference Frequency Generation (DFG). This was an important step as it provided access to the strong, fundamental transitions of many species, hence providing the potential for highly sensitive trace gas spectroscopy. Multi-mode radiation at 1.56 µm, from the diode-pumped Er:Yb:glass laser mentioned above, was mixed with a single-mode Nd:YAG laser at 1.06 µm in a periodically poled lithium niobate crystal to produce multi-mode radiation in the region of 3.3 µm. This relatively complex, low power laser source was used to simultaneously detect CH_4 and NH_3 in the mid-infrared region [7].

This thesis reports the work of extending the MUMAS technique to alternative spectral regions with different laser sources and alternative detection schemes, of greatly evolving the modelling of MUMAS spectra, of overcoming many of the previous limitations of the technique and of improving the understanding and technical details of the technique in general. After careful consideration for the behaviour of the tuning of multi-mode lasers, an entirely new computational model is developed (chapter 3). This computational model has greater accuracy, is more powerful and is faster to operate than the previous computational model. The application of an Interband Cascade Laser (ICL) to MUMAS

in the mid-infrared region is reported (chapter 4), and the high sensitivity due to the strength of the transitions found in this region is demonstrated. The broad spectral coverage of these devices is demonstrated and subsequently utilised to obtain multi-species spectra. ICLs with wide intermode-spacings are used to obtain MUMAS spectra of trace amounts of methane in atmospheric pressure, thus demonstrating the potential for highly sensitive, multi-species detection using a single multi-mode laser source. Extension of the technique to the $5-6$ µm range is demonstrated with a commercially available Quantum Cascade Laser (QCL) (chapter 5). This QCL exhibits strong variations in the spectral intensity distribution. As these variations are less than ideal, this illustrates the resilience of the technique to poorly behaved laser sources. In addition, transitions of H_2O are simultaneously recorded in the presence of laboratory air containing water vapour, thus demonstrating the ability of MUMAS to distinguish interfering species in the gas sample. Further developments of the technique in the near-infrared region of $1-2$ µm using a commercially available diode laser are outlined (chapter 6). The Mode Fractional Power (MFP) of the modes during scanning is introduced as an important concept in the interpretation of MUMAS spectra, and the computational model which is developed in order to account for varying laser intensity envelopes during the scan of the modes is described. An alternative detection scheme, *balanced ratiometric detection*, is introduced and the advantages of this detection scheme are explained and demonstrated. The first MUMAS spectrum obtained at atmospheric pressure using a commercially available laser is reported. Finally, MUMAS spectra obtained at a range of temperatures are shown in order to demonstrate the ability to perform thermometry using MUMAS. Chapter 7 draws conclusions from the thesis as a whole before suggested further developments of the MUMAS technique are discussed in chapter 8.

2.8 Summary

This chapter began by describing a range of existing and potential applications of gas sensing and by demonstrating the need for a trace gas sensing device. Non-optical methods were briefly mentioned before the most fundamental optical method, laser absorption spectroscopy, was introduced.

Tunable Diode Laser Absorption Spectroscopy (TDLAS), the most common method of laser absorption spectroscopy, was subsequently presented. The benefits and limitations of this technique were discussed, and additional sensitivity enhancement techniques which can be combined with TDLAS were outlined. The need for a technique with a broad spectral coverage was explained, before various existing techniques were critically examined. Table 2.1 presents a summary of the range of techniques explored in this chapter, along with some advantages and disadvantages of each technique.

Finally, Multi-mode Absorption Spectroscopy (MUMAS) was introduced as a viable alternative. This technique presents a simple method to acquire high-resolution spectral information across a broad spectral range. MUMAS is the technique used for the experimental work presented in this thesis.

Technique	Advantages	Disadvantages
Gas chromotography	High sensitivity. High selectivity.	Requires sampling (invasive and not real-time). Expensive. Bulky.
Mass spectrometry	High sensitivity. High selectivity.	Requires sampling (invasive and not real-time). Expensive. Bulky.
Calorimetric methods	Low-cost. Robust. Particularly suited to some applications.	Problematic cross-response. Slow recovery time. Requires particular operating conditions. Can become contaminated. Limited lifetime.
Metal-oxide semiconductors	Low-cost. Robust. Particularly suited to some applications.	Problematic cross-response. Slow recovery time. Requires particular operating conditions. Can become contaminated. Limited lifetime.
TDLAS	High selectivity. High resolution. Non-invasive. Fast time response. Compact. Robust. Low power requirements. Operates at room temperature.	Poor bandwidth. Limited MHF tuning range.
WMS	Increased sensitivity. Improved dynamic range.	Added complexity. Requires calibration.
CEAS	Increased sensitivity. Less vulnerable to mechanical vibrations.	Expensive cavity mirrors. Can be bulky.
OF-CEAS	Increased sensitivity. Higher resolution. Ready calibrated frequency scale.	Further complexity with phase locking and step-wise scanning.
CRDS	Increased sensitivity. Improved dynamic range.	Requires high speed electronics. Prone to noise from mechanical vibrations. Indirect measure of concentration.
Multiplex TDLAS	Broader spectral coverage with inherent high-resolution	Further complexity with mutli-plexing. Need to couple the beams. Multiple lasers, detectors, drivers etc. increases cost.
EC-DLs	Large MHF tuning range. High resolution.	Severely restricted tuning range. Vulnerable to vibrations.
VCSELs	Large MHF tuning range. High resolution. Fast scan rates.	Only developed in a few restricted spectral ranges. Low output powers.
MEMS	Large MHF tuning range. High resolution. Fast scan rates. High accuracy. Enhanced mechanical stability.	High cost. Difficulties with packaging and integration. Mechanical, electrical and thermal stability problems.
Broadband source (Non-dispersive)	Simple detection scheme. Relatively low cost.	Only works in fortuitous situations. Poor selectivity. Poor noise characteristics. Poor cross-response.
Broadband source (Dispersive)	Broad spectral coverage. High resolution.	Requires complex dispersive elements. Bulky. Expensive. Resolution limited by inherent resolution of dispersive elements.
MIREGAS	Compact. Robust. Relatively inexpensive. Multi-species capability.	Limited spectral coverage. Vulnerable to contaminating species. Low power.
Correlation spectroscopy	Broad spectral coverage. High resolution. High specificity. Immune to laser fluctuations. No spectral knowledge required. Inexpensive. Robust.	Requires a well-characterised reference cell at the same pressure and temperature as the unknown sample. Multiple reference cells required for multiple species.
OFC spectroscopy	High spectral resolution. Broad spectral coverage. Can be combined with modulation techniques.	Highly complex. Expensive. Bulky. Requires dispersive elements.
Multi-heterodyne spectroscopy	Avoids over-congestion of spectral features. Improved dynamic range. Broad spectral coverage.	High complexity. High cost. Limited by bandwidth of detectors. Requires phase-locked lasers.
MUMAS	Broad spectral coverage. High-resolution. Simple. Relatively low-cost (inexpensive lasers and detection scheme). Immune to interfering species.	Involved modelling process. Vulnerable to pressure broadening. Limited range of suitable multi-mode lasers.

Table 2.1: A summary of the range of techniques explored in this chapter, along with some advantages and disadvantages of each technique.

Chapter 3

The theory of MUMAS

3.1 Overview

This chapter describes the theory of Multi-mode Absorption Spectroscopy (MUMAS), the spectroscopic technique used for all the work presented in this thesis. The basic theory of operation of the technique is described and special consideration is taken for the behaviour of the tuning of the modes.

In order to extract information of a species from experimental MUMAS data, it is necessary to model MUMAS spectra which can be fitted to the experimental data. The model used for previous work is outlined, along with its limitations. A new model, termed the *expansion-model*, which takes into account the behaviour of the tuning, is presented. The *MUMAS Equation*, which forms the basis of this expansion-model, is introduced.

A new computational model is required to incorporate the new expansion-model and the MUMAS Equation. Details of the computational modelling process are described, and the advantages of this technique are discussed.

Finally, the theoretical and performance-related requirements for a multi-mode laser source are discussed.

3.2 Theory of operation

Multi-mode Absorption Spectroscopy (MUMAS) is a spectroscopic technique whereby the radiation from multiple longitudinal modes from a single laser interact with the molecular absorption transitions of a gaseous sample, as the modes are scanned in frequency. In brief, a change in total transmitted intensity, relative to the incident intensity, is recorded whenever any of the modes, during their scan, come into resonance with an absorption line in the spectrum of the gas. The resulting signal is characteristic of the absorbing species being probed by the particular multi-mode laser source being used. Since the spectral locations of the absorption lines are available from a suitable database, when the laser mode parameters are also known, the resulting MUMAS signature can be modelled and compared with the experimental data.

Figure 3.1a schematically illustrates the operating principle of MUMAS. The red lines represent the individual longitudinal modes of the laser and the blue lines represent the molecular absorption transitions of CO_2 in this region. The laser spectrum is made up of a set of longitudinal modes of finite width, $\delta\nu$, which have distinct frequencies, ν_q, are equally spaced by a parameter known as the intermode-spacing, $\Delta\nu_{\text{mode}}$, and have intensities given by the overall intensity envelope of the laser modes, $E(\nu)$. The transmission spectrum of the gas sample is comprised of the molecular absorption transitions which have precisely known frequencies, known temperature-dependent strengths and known pressure- and temperature-broadening coefficients.

To obtain a MUMAS spectrum, the set of laser modes are simultaneously scanned across a frequency interval. Whenever any of the individual modes come into resonance with the molecular absorption transitions, they will be partially absorbed, which results in a decrease in the transmission of the laser, and is forthwith termed a *MUMAS absorption feature*. The resulting MUMAS spectrum is a weighted superposition of the transmission

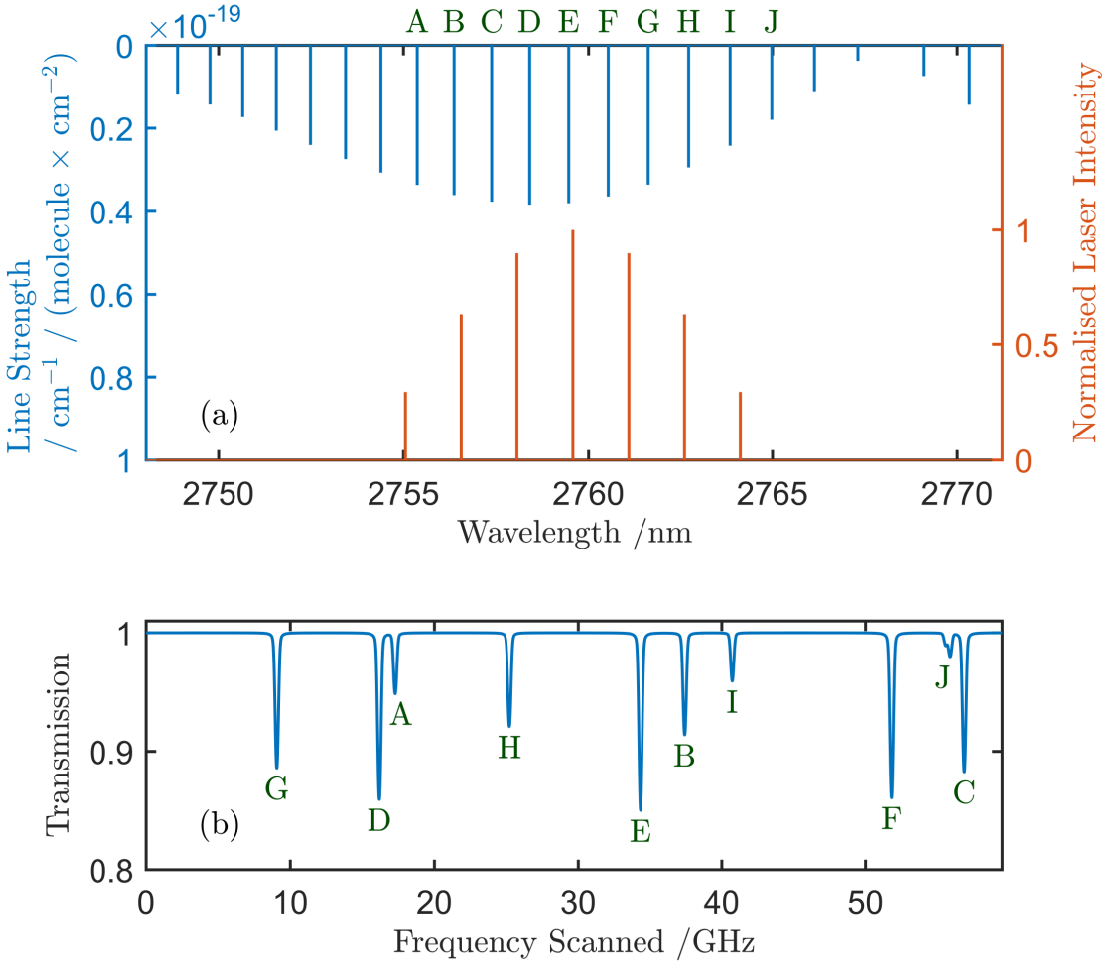

Figure 3.1: In panel (a), the red lines represent the individual longitudinal modes of the laser and the blue lines represent the molecular absorption transitions of CO_2 in this region. Panel (b) shows the simulated MUMAS spectrum that is obtained by interacting the laser modes with the molecular absorption transitions from panel (a). The MUMAS features in this spectrum have been labelled 'A' to 'J', and correspond to transitions labelled in panel (a).

spectra of the individual modes in the laser comb.

Such a MUMAS spectrum is shown in figure 3.1b which is the result of interacting the laser modes with the molecular absorption transitions from figure 3.1a. The number of MUMAS absorption features corresponds to the number of molecular absorption transitions that are probed. MUMAS spectra are placed on a relative frequency scale which corresponds to the frequency range over which each mode is scanned. Unlike conventional absorption spectra, this relative frequency scale cannot be placed on an absolute frequency scale as it contains contributions from several distinct spectral regions.

In figure 3.1a, the conventional molecular absorption transitions are labelled in ascending order across the absolute frequency scale. The MUMAS absorption features which are caused by these molecular absorption transitions are correspondingly labelled 'A' to 'J' in figure 3.1b. It is clear that they occur in a different order than to the conventional order of figure 3.1a. Instead, each absorption feature occurs at a position determined by its frequency position relative to the starting and finishing position of the interacting laser mode. If a molecular absorption transition is near to a laser mode at the start of a scan, it will occur near the start of the MUMAS spectrum, and similarly, if a molecular absorption transition is near to a laser mode at the end of a scan, it will occur near the end of the MUMAS spectrum. The MUMAS spectrum that results is unique to the laser, the species, and the thermodynamic properties of the species, and is therefore known as a *MUMAS fingerprint*.

It was noted above that the MUMAS spectrum is a weighted superposition of the transmission spectra for individual modes of the laser comb. Figure 3.2 further elucidates this concept. Figure 3.2a shows the individual longitudinal modes of the laser labelled '1' to '9'. Note that this is a schematic of the modes when they are in the centre of the scan range, and the scanning direction is such that the frequencies of the individual modes increase as they scan. At the centre of the scan range, the modes labelled '1' and '9' do

not fall within the intensity envelope of the laser and therefore they have zero intensity. However, at the start of the scan, the mode labelled '9' has a non-zero intensity and at the end of the scan, the mode labelled '1' has a non-zero intensity. Figure 3.2b shows the distribution of optical power between these laser modes at each position along the scan. The transmission power has been divided into bands, with the width of each band representing the contribution to the total transmitted power from each individual mode. The proportion of total power that belongs to a particular mode is known as the Mode Fractional Power (MFP) of that mode. The MFP of each mode has been highlighted by a coloured block, and, for clarity, the power in alternate modes have alternate colours. It is also clear that at start of the scan, the mode labelled '9' has a non-zero intensity which eventually goes to zero, and near the end of the scan, the mode labelled '1' goes from having zero intensity to having a non-zero intensity. If there is an absorption by a particular mode, it results in the reduction of power in the corresponding band. Accordingly, each band of the transmission also includes the MUMAS absorption features which arise from absorption by that mode. The overall MUMAS spectrum in figure 3.2c is what results from summing these bands onto a single transmission spectrum, with the various MUMAS absorption features corresponding to the various interactions between individual modes and molecular absorption transitions.

To a first approximation, and in the following description in this section, when the modes are scanned the frequency position of each mode scans at the same rate and therefore the scanning is, in effect, a translation of a comb of laser modes under a fixed intensity envelope. After all the modes have scanned a distance of one intermode-spacing, each mode will occupy the same spectral location that the adjacent mode occupied at the start of a scan, and therefore the laser spectrum will be identical to the laser spectrum at the start of the scan. Hence, further scanning of the laser modes will produce a repeated MUMAS spectrum, termed a *repeat-unit*. Therefore, a 'full' MUMAS spectrum

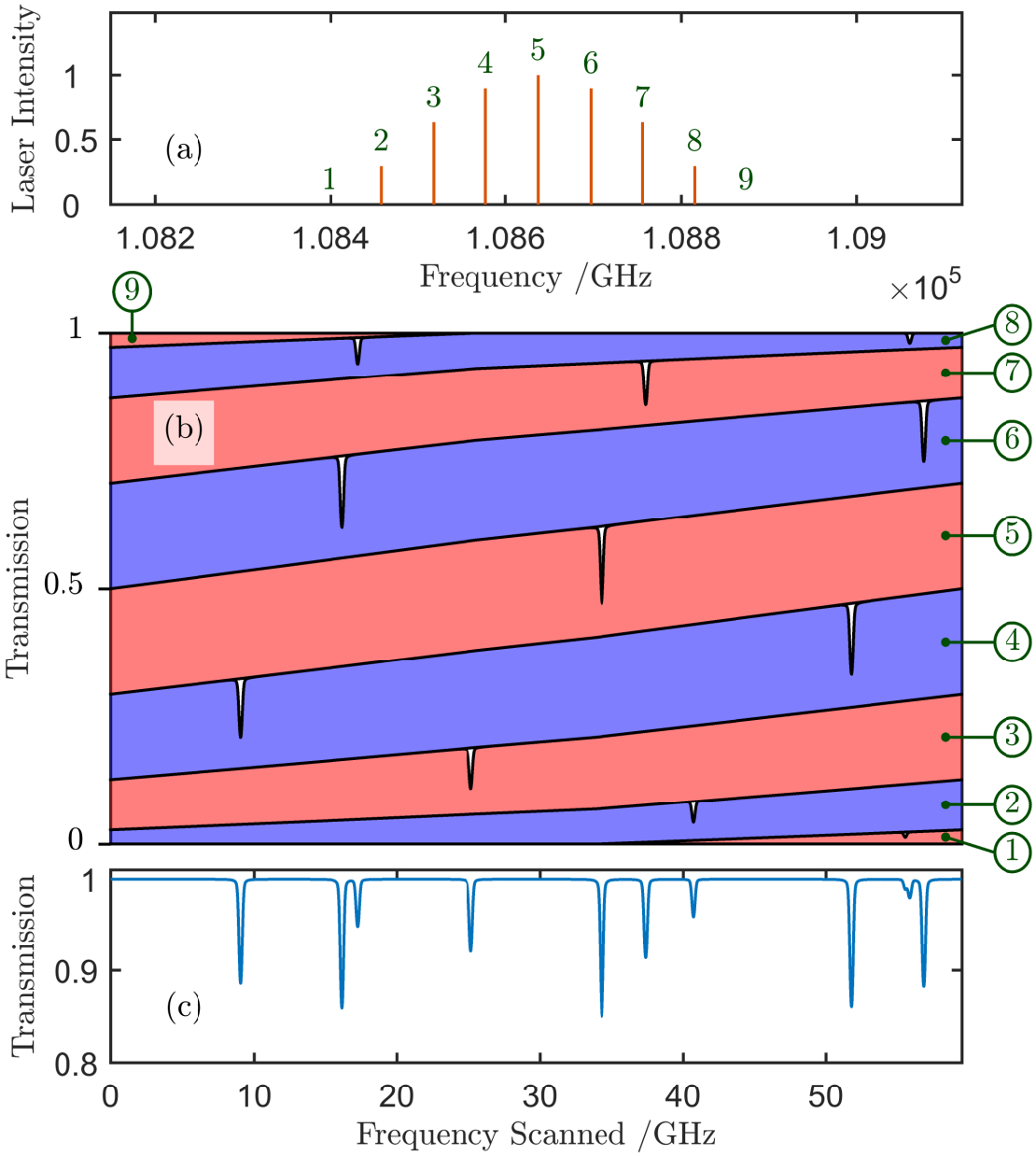

Figure 3.2: Panel (a) shows the individual longitudinal modes of the laser labelled '1' to '9'. Panel (b) shows the distribution of optical power between these laser modes at each point along the MUMAS spectrum. It has been divided into bands, with the width of each band representing the contribution to the transmission from each individual mode. Each band is correspondingly labelled '1' to '9'. Each band also includes the MUMAS absorption features which are caused by that particular mode. Panel (c) shows the simulated MUMAS spectrum that would be obtained by interacting the laser modes with the molecular absorption transitions from figure 3.1a. It is the result of summing the bands of the transmission from panel (b) onto a single transmission.

is defined to have a spectral coverage of one intermode-spacing, with any further spectral features being repeated and redundant. Due to the repetition inherent in a MUMAS spectrum, changing the exact spectral location of the modes will not change the form of the MUMAS signature, but instead will only produce a cyclic shift of the MUMAS signature.

Both the laser parameters and the species parameters will affect the form of a MUMAS spectrum. The key laser parameters that determine the form of the MUMAS spectrum are the intermode-spacing, $\Delta\nu_{\text{mode}}$, the individual mode-linewidths, $\delta\nu$, and the intensity envelope of the laser modes, $E(\nu)$. The key species parameters that determine the form of the MUMAS spectrum are the frequency, strength, and broadening coefficients of the molecular absorption transitions of the species that are present, the partial pressures of the species that are present and the ambient pressure and temperature of the bulk gas.

The form of the MUMAS spectrum can qualitatively be described by the positions, widths and relative heights of the MUMAS absorption features. The positions of the MUMAS absorption features are mainly determined by the intermode-spacing and the frequency position of the molecular absorption transitions. The widths of the MUMAS absorption features are mainly determined by the individual mode-linewidths, the ambient pressure and temperature of the bulk gas and the broadening coefficients of the molecular absorption transitions. The relative heights of the MUMAS absorption features are mainly determined by the strength of the molecular absorption transitions, the partial pressure and temperature of the species and the MFP of the laser modes.

The form of the MUMAS spectrum therefore encodes information on the identity of the species, its partial pressure and the temperature and ambient pressure of the bulk gas. Hence, with known laser parameters, the MUMAS spectrum can be used to infer these various parameters.

3.3 Theory of tuning

To understand how the modes are scanned, it is instructive to look at the equation which governs the frequency of the longitudinal modes.

Longitudinal modes of a laser are caused by a standing wave pattern formed by interference within a cavity of optical length L. For nodes to be at the boundaries of the cavity, there must be an integer number, q, of half-wavelengths, $\frac{\lambda}{2}$, in the cavity, which leads to equation 3.1. q is forthwith termed the *mode index*.

$$L = q\frac{\lambda}{2}\,. \tag{3.1}$$

Re-arranging equation 3.1, and using the relation $c = \lambda\nu$, where ν is the frequency, leads to equation 3.2 which gives the frequency positions of the modes, ν_q, in terms of the optical length of the cavity.

$$\nu_q = q\frac{c}{2L}\,. \tag{3.2}$$

The modes are equally spaced by the intermode-spacing, $\Delta\nu_{\text{mode}}$, which is given by equation 3.3.

$$\Delta\nu_{\text{mode}} = \frac{c}{2L}\,. \tag{3.3}$$

In order to change the frequency position of the modes, as given by equation 3.2, the optical length of the cavity must be altered. The optical length of the cavity is the product of the refractive index of the material inside the cavity and the physical length of the cavity. Therefore in order to effect the scanning of the modes, either the refractive index of the material inside the cavity or the physical length of the cavity must

be modulated. In semi-conductor lasers, this is done by modulating the drive current of the laser which in turn results in a combination of a modulation of the refractive index of the cavity and a modulation of the physical length of the cavity through thermal expansion.

Equation 3.3 describes how changing the optical length of the cavity also changes the intermode-spacing. This gives further insight into how the modes are scanned. As the intermode-spacing increases, all the modes are stretched along the frequency-scale with the higher frequency modes covering a greater frequency interval than the lower frequency modes.

The optical length is assumed to vary linearly in time, $L = L_0 - \phi t$, where L_0 is the initial optical length of the cavity and ϕ is a measure of the rate at which the optical length of the cavity changes. This expression for the length of the cavity is substituted into equation 3.2 to give equation 3.4a. The optical length of the cavity will only vary slightly, and therefore $\phi t \ll L_0$ for all times during the scan. Equation 3.4b is the result of expanding equation 3.2 as a Maclaurin series to first order, and expressing the mode index as $q = q_c + p$, where q_c is the mode index of the central mode in the laser intensity envelope, p is an integer between $-\frac{k}{2}$ and $\frac{k}{2}$, and k is the number of modes in the laser intensity envelope. For the visible and near-infrared lasers used in previous MUMAS work, the mode index was typically of order 10^4, and therefore $q_c \gg p$.

$$\nu_q = q\left(\frac{c}{2\left(L_0 - \phi t\right)}\right) \tag{3.4a}$$

$$\simeq q_c\left(\frac{c}{2L_0}\right) + p\left(\frac{c}{2L_0}\right) + q_c\left(\frac{c\phi}{2L_0^2}\right)t + p\left(\frac{c\phi}{2L_0^2}\right)t\,. \tag{3.4b}$$

As $q_c \gg p$ and $\left(\frac{c}{2L_0}\right) \gg \left(\frac{c\phi}{2L_0^2}\right)t$ for all times during the scan, the fourth term in

equation 3.4b is much smaller than the others, and therefore, to a first approximation, it can be ignored to give equation 3.5.

$$\nu_q = q\left(\frac{c}{2L_0}\right) + q_c\left(\frac{c\phi}{2L_0^2}\right)t\,. \tag{3.5}$$

Equation 3.5 describes the translation of a full set of laser modes with time and is thus termed the *translation-model*. The first term describes the initial frequency position of the set of q modes and the second term is a fixed offset which is applied to all modes as they scan. Due to the validity of the expression $q_c \gg p$ for the lasers used in earlier work on MUMAS, this model was sufficient to describe the MUMAS spectra previously obtained. However, for the work in this thesis, a full model of the scanning of the modes is required. This is primarily due to the breakdown of the assumption $q_c \gg p$. The mode indices for the lasers used in this work are typically much smaller than before, and the lasers also have a greater number of modes and hence a greater maximum value of p. This has consequences for some of the earlier concepts about the theory of operation. In particular, the intermode-spacing will no longer remain constant as the modes scan, and the concept of a repeat-unit, whereby the MUMAS spectrum repeats in equivalent units as the modes are scanned beyond a single intermode-spacing, will need to be revised. These consequences are addressed below.

A complete description of the scanning of the modes, without any approximations, is given in equation 3.4a. The intermode-spacing increases as the modes scan, the modes expand along the frequency axis, and each mode scans at a different rate. This model is termed the *expansion-model*. Unlike in the translation-model, the length of the spectral segment that each mode scans will be different, and instead of a 'full' MUMAS spectrum being defined to have a spectral coverage of one intermode-spacing, it is defined as the spectral-distance over which the central mode in the comb scans in order to reach the

initial spectral-position of the adjacent mode. All other modes will either be slightly in-front of or slightly behind the initial spectral-position of the adjacent mode.

In the expansion-model, the modes will scan over an even greater spectral region for each consecutive scan of one intermode-spacing. Therefore, the spectral location of each mode at the start of the scan of one intermode-spacing will not line-up with the spectral location of each mode at the start of the previous scan of one intermode-spacing. Consequently, the exact position of the MUMAS absorption features will vary slightly between consecutive scans of one intermode-spacing. Therefore, consecutive segments of length equal to the intermode-spacing of the MUMAS spectrum will not be identical repetitions. However, the overall profile of the MUMAS signature for consecutive scans of one intermode-spacing will be approximately similar, and therefore each of these scans of one intermode-spacing is defined as a *pseudo-repeat-unit*.

The translation-model of the scanning of laser modes formed the basis of the original computational model for MUMAS. The expansion-model, which is a more accurate model for the scanning of laser modes, requires a new computational model to be developed.

3.4 Modelling of MUMAS

As has been illustrated, an experimental MUMAS spectrum of a gas sample encodes information on the identity of the species in the sample, its pressure and the temperature and ambient pressure of the bulk gas. Therefore, by modelling a MUMAS spectrum and fitting to the experimental MUMAS spectrum, these various parameters can be derived.

3.4.1 Spectroscopic data modelling

In order to model the MUMAS spectrum of a particular species, spectroscopic data of the species are required. The HITRAN spectral database provides the position, strength

and broadening coefficients for the species of interest [103]. To ensure efficiency in the modelling, only the molecular absorption transitions which fall within the output bandwidth of the laser are imported from the database.

For the HITRAN database, the reference temperature, T_{ref}, for all the molecular absorption transitions is 296 K [104]. The populations of energy levels are determined by the Maxwell-Boltzmann distribution, assuming thermal equilibrium. Therefore, the line-strength factors will change for different temperatures and they must therefore be re-weighted to represent an arbitrary temperature, T. This re-weighting is implemented using equation 3.6, which describes the line-strength, $S_{if}(T)$, of a transition between a lower state, i, and upper state, f, as a function of temperature, T. Values for the total partition sum, Q, are provided by HITRAN, and $\tilde{\nu}_{if}$ is given as vacuum wavenumber of the transition in cm^{-1} in the database. In what follows in the rest of this chapter, the line-strength of a particular transition will be denoted as $S_j(T)$.

$$S_{if}(T) = S_{if}(T_{\text{ref}}) \frac{Q\left(T_{\text{ref}}\right)}{Q(T)} \frac{\exp\left(\frac{-hcE_i}{k_B T}\right)}{\exp\left(\frac{-hcE_i}{k_B T_{\text{ref}}}\right)} \frac{\left(1-\exp(\frac{-hc\tilde{\nu}_{if}}{k_B T})\right)}{\left(1-\exp(\frac{-hc\tilde{\nu}_{if}}{k_B T_{\text{ref}}})\right)} . \tag{3.6}$$

This re-adjustment of the line-strength factors is adequate for temperatures around 296 K. However, for much higher temperatures, there will be molecular absorption transitions which have negligible strength at room temperature, and are not included in the HITRAN database, but become important at high temperatures. These particular transitions can be obtained from the HITEMP database, which includes high-temperature molecular absorption transitions for H_2O, CO_2, CO, NO and OH [104].

3.4.2 Computational modelling code for the translation-model

For the translation-model of the scanning of laser modes, the computational modelling code can be described in three steps: firstly, a conventional transmission spectrum is

generated for the absorbing species that are present; secondly, the laser mode spectrum is generated and; finally, the expected MUMAS spectrum is calculated by considering the interaction between the laser modes and the transmission spectrum of the absorbing species.

The sampling resolution required for the vector describing the laser mode spectrum is typically very high. The origin of this is that a sufficiently high sampling resolution is required to represent the lineshape of each mode. Furthermore, as the intermode-spacing is generally a few orders of magnitude larger than the mode-linewidth, when the high sampling resolution of the lineshape of each mode is extended to the full length of the laser spectrum, the vector describing the laser spectrum becomes very large. Additionally, for computational purposes, the resolution of the vector describing the transmission spectrum of the absorbing species has to be equal to the resolution of the vector describing the laser spectrum. Ultimately, the resulting MUMAS spectrum vector will have the same sampling resolution, which will typically be much larger than necessary, yet this high sampling resolution will cause long computation times.

The interaction is simulated by translating the comb of laser modes across the transmission spectrum of the absorbing species and calculating the sum of the element-wise product at each point. As the interacting vectors are so large, a methodical loop-wise implementation of this interaction would be time consuming and therefore a cross-correlation of these two interacting vectors is used instead. A cross-correlation of two vectors is linked to the element-wise product of those vectors through Fourier transforms and therefore this approach allows efficient computation of the interaction by using Fast Fourier Transform (FFT) algorithms [105]. The result is a vector representing a simulated MUMAS spectrum covering many repeat-units. Only a small section of this result, equivalent to a scan of one intermode-spacing, is required. Despite a large portion of the result being discarded, it is still much more efficient than the loop-wise

implementation.

3.4.3 Computational modelling code for the expansion-model

In the expansion-model, as the scanning of modes is not described by a translation of the comb of laser modes, it is not possible to use the computationally efficient cross-correlation method described in section 3.4.2. This method is physically intuitive as the cross-correlation is analogous to the operation of scanning the modes in frequency. Instead, the expansion-model is computationally modelled by taking a broader view of the nature of a MUMAS spectrum.

The MUMAS equation

The fundamental concept of the computational modelling code for the expansion-model is to prospectively calculate the position of all the MUMAS absorption features in a MUMAS spectrum before the magnitudes or lineshapes of the MUMAS absorption features are considered. For a mode with mode index given by q and a set of j transitions, the frequency position of all the MUMAS absorption features caused by this mode, $F_{q,j}$, in a MUMAS spectrum are defined by the *MUMAS equation*, equation 3.7, the derivation of which is outlined in appendix A. T_j is the absolute frequency position of the set of j molecular absorption transitions, and ν_c is the frequency of the central mode, with mode index q_c.

$$F_{q,j} = \frac{q}{q_c} T_j - \nu_c \,. \tag{3.7}$$

In the modelling process, all the modes which lie within the bandwidth of the laser are considered. Using equation 3.7, many of the frequency positions of the MUMAS absorption features are determined to be outside the range of the MUMAS spectrum, and

are therefore discarded at this stage of the modelling process. This avoids redundantly considering their magnitudes or lineshapes. However, it should be noted that MUMAS absorption features which lie just outside the MUMAS spectrum are also considered as the wings of these features contribute to the MUMAS spectrum.

Absorption spectra for each mode

To generate the full MUMAS spectrum, the absorption spectrum of each mode is considered in turn, with each one accounting for the interaction between that particular mode and all the molecular absorption transitions. Accordingly, the absorption arising from each molecular absorption transition needs to be calculated, with each absorption being dependent upon the number density of the absorber, N, the path-length of the absorber, l, and the absorption cross-section, σ_j.

The absorption cross-sections are modelled as Voigt profiles to account for the two main forms of broadening: Doppler broadening, which typically takes a Gaussian form, and pressure broadening, which typically takes a Lorentzian form. These processes are described in section 2.3.2, and the computational approximation of these Voigt profiles is described in appendix B. The absorption cross-sections, $\sigma_j(\nu)$, centred on the frequency ν_0, are the product of these normalised Voigt line-shapes, $g_V(\nu - \nu_0)$, and the line-strength factors, S_j, for each molecular absorption transition, as described in equation 3.8.

$$\sigma_j(\nu) = S_j \cdot g_V(\nu - \nu_0) \ . \tag{3.8}$$

The Beer-Lambert Law is used to calculate the absorption spectrum, A_q, for a particular mode, q, of the laser. As described in section 2.3, it is found by calculating the product of the absorption cross-sections of all molecular absorption transitions that

interact with that particular mode, the path-length and the number density of the absorber, summing these products and exponentiating this sum, as shown in equation 3.9.

$$A_q = \exp\left(-\sum_j \sigma_{q,j} NL\right) . \tag{3.9}$$

Note that the absorption cross-section for each MUMAS feature is defined to be centred on the frequency of the MUMAS feature in the MUMAS spectrum, as illustrated by substituting $F_{q,j}$ for ν_0 in equation 3.8 to give equation 3.10. The absorption cross-section, $\sigma_{q,j}$, is defined for a particular mode, q, interacting with a particular molecular absorption, j.

$$\sigma_{q,j} = S_j \cdot g_V\left(\nu - F_{q,j}\right) . \tag{3.10}$$

Mode Fractional Power (MFP)

The absorption spectrum for each mode needs to be weighted by the MFP, $W_q(\nu)$. In general, the MFP of a mode will vary slightly as the modes are scanned. This is illustrated in figure 3.2b.

For a fixed intensity envelope of the laser spectrum, the MFP will either increase or decrease as the modes are scanned, depending upon whether the modes are moving along a positive or negative gradient of the intensity envelope, respectively.

For lasers where the intensity envelope of the laser spectrum varies as the modes are scanned, the MFP must be tracked and recorded as the modes are scanned.

MUMAS transmission spectrum

The MUMAS transmission spectrum, $T(\nu)$, is a weighted superposition of the absorption spectra of all the modes, given by equation 3.11, where the weighting is given by the

MFP as the modes are scanned.

$$T(\nu) = \sum_{q} W_q(\nu) \cdot A_q \,. \tag{3.11}$$

Consideration for the finite mode-linewidth of the laser modes

In what has been presented so far, no consideration has been given to the broadening caused by the finite linewidth of the modes themselves.

The lineshape of the laser modes takes an approximately Lorentzian form, with mode-linewidth $\delta\nu$, as discussed in the *Laser mode-linewidth broadening* subsection of section 2.3.2. To incorporate this finite mode-linewidth broadening into the MUMAS transmission spectrum, the spectrum would have to be convolved with a normalised Lorentzian lineshape of width $\delta\nu$. Alternatively, it is noted that the linewidth of the spectral feature resulting from the convolution of two Lorentzians, of width Δ_A and Δ_B, is given by the sum of the two component linewidths, $\Delta_{A\otimes B} = \Delta_A + \Delta_B$. Therefore, a computationally efficient way of considering the finite mode-linewidth is to add it to the pressure broadened Lorentzian linewidth before calculating the Voigt profiles of the absorption cross-sections above, and this is the method used in the computational modelling of a MUMAS spectrum.

Computational advantages of the expansion-model

Along with being more accurate, the computational modelling code for the expansion-model is also more versatile. Unlike in the computational modelling code for the translation-model, for the expansion-model it is focused around each feature in the MUMAS spectrum and therefore the properties of each feature are easily accessible. This allows property-specific modelling of selected features which helps with the diagnosis of

poorly-fitted spectra, the investigation of further advancements of the MUMAS technique and generally aids in a more in-depth understanding of the nature of a particular MUMAS spectrum. Along with these advantages, there are also various computational-efficiency advantages of the computational modelling code for the expansion-model.

One of the most computationally expensive stages of the modelling code is calculating the Voigt profile for all the MUMAS absorption features. However, the height of the majority of these features will be orders of magnitude less than those of the most prominent features and will therefore contribute negligibly to the MUMAS absorption spectrum. The computational modelling code for the expansion-model allows for a pre-selection of the Voigt profile calculation of only the MUMAS absorption features which have a magnitude within a fixed factor of the most prominent MUMAS absorption features (usually two orders of magnitude). This significantly reduces the computation time and has negligible effect on the resulting MUMAS absorption spectrum.

Two of the most significant disadvantages of the cross-correlation method used in the computational modelling code for the translation-model are the large amount of redundancy in the resulting MUMAS absorption spectrum which covers multiple repeat-units, and the high sampling resolution required to account for the disparity between the magnitude of the individual mode-linewidths and the intermode-spacing (section 3.4.2). These are both overcome in the computational modelling code for the expansion-model. In the computational modelling code for the translation-model, the cross-correlation is necessary to determine the position at which MUMAS absorption features will appear in a MUMAS spectrum, however, in the computational modelling code for the expansion-model, the position of the features are pre-calculated and therefore a cross-correlation is unnecessary and the redundancy in the resulting vector is avoided. Furthermore, in the computational modelling code for the expansion-model, the sampling resolution is no longer constrained by the disparity between the magnitude of the individual mode-

linewidths and the intermode-spacing. The high-resolution 'intermediate' spectra of the conventional transmission spectrum and the laser modes is no longer necessary, and therefore the sampling resolution of the MUMAS spectrum can be set to a much lower, yet sufficient, value.

3.5 Laser requirements for MUMAS applications

MUMAS is a generalised form of single-mode absorption spectroscopy that is, in principle, able to make use of any multi-mode laser device for spectroscopy. There are, however, a number of requirements of the laser device which would make it more suitable for the technique.

The most fundamental requirements of a device used for MUMAS are that it has several longitudinal-modes which lase simultaneously, and that these modes overlap with some molecular absorption transitions of the target species.

In order for the device to be used in an application, the laser spectrum must also be 'well-behaved', or repeatable, when the modes are scanned. This requirement for repeatability is two fold; the modes must scan predictably within a scan so as to allow modelling of the experimental data, and the relative intensity of the modes must be temporally stable over multiple scans so as to allow for averaging and long-term use. Predictable scanning is hampered if the modes are not independent. Competition for energy stored in the gain medium by neighbouring modes will lead to random fluctuations in the intensity of the modes, and, if the frequency of these fluctuations is of the same order as the rate of scanning of the modes, then consecutive MUMAS spectra will be different. Furthermore, it is not feasible to constantly monitor the mode intensities either during a single MUMAS scan, or over long-term use of the device and therefore the scanning laser spectrum must be temporally stable over many months of use.

In previous work on MUMAS, it was necessary for the laser spectrum to have an intensity envelope which could be accurately modelled by a simple function (e.g. a truncated Lorentzian or Gaussian form). During the course of the work in this thesis, this constraint was relaxed in order to allow a measured laser intensity envelope to be used as a fixed intensity envelope in the computational modelling process. Further development of the computational model catered for the use of multiple intensity envelopes in the computational modelling procedure, each measured at a particular point along the scan. This is useful if the intensity envelope changes appreciably during a scan. Hence, the computational MUMAS modelling code now has the ability to generate a MUMAS spectrum even when the intensity envelope of the laser changes within a single scan. It should be noted that this varying intensity envelope must still be repeatable and temporally stable.

In order to ensure sufficient sensitivity with a MUMAS device, it is important for the intensity noise of the laser to be low. The SNR decreases with higher noise intensity, and this directly impacts the sensitivity of MUMAS.

In addition to these performance related requirements, there are also some theoretical requirements on the structure of the laser spectrum which affect the form of the MUMAS spectrum.

Firstly, as with all absorption spectroscopy techniques, the spectral resolution of a MUMAS spectrum will be affected by the mode-linewidth of the individual modes. A larger mode-linewidth will result in a decrease in the resolution of the MUMAS absorption features. Therefore, it is desirable for the mode-linewidth to be as small as possible, and at least a few orders of magnitude less than the width of the molecular absorption transitions once Doppler- and pressure-broadening have been accounted for.

Secondly, and perhaps most critically, is the magnitude of the intermode-spacing. The form of a MUMAS spectrum is very sensitive to the intermode-spacing. A small

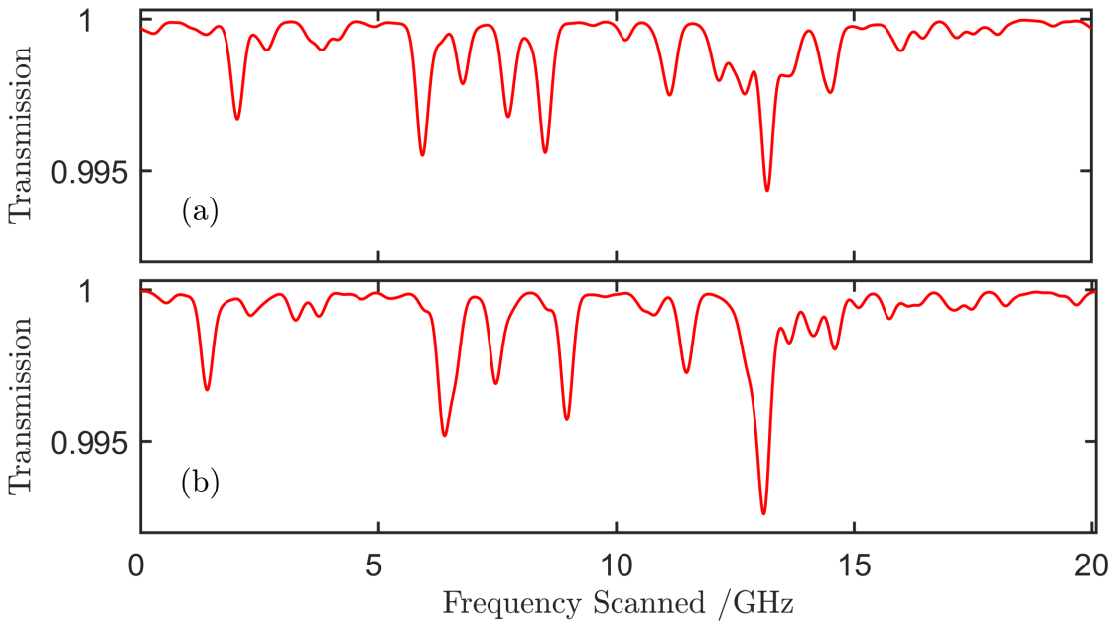

Figure 3.3: An illustration of the effect of the intermode-spacing on the form of MUMAS spectra of 5 mbar of CH_4 when using a laser spectrum centred around 3.7 µm. The laser spectra which give rise to both MUMAS spectra have identical properties, except for their intermode-spacing. The intermode-spacings of the lasers used to simulate the MUMAS spectra are 20 GHz and 20.1 GHz for panel (a) and (b), respectively. It is clear that a small change in the intermode-spacing causes a substantial change to the form of the MUMAS spectrum.

change in the magnitude of the intermode-spacing can substantially change the form of a MUMAS spectrum. This is illustrated in figure 3.3 where it is clear that a small change in the intermode-spacing from 20 GHz to 20.1 GHz causes the form of the MUMAS spectrum to change significantly.

The width of a MUMAS absorption feature is independent of the intermode-spacing, and therefore a smaller intermode-spacing means that MUMAS absorption features cover a wider proportion of a MUMAS spectrum. This leads to congested spectra that risk becoming featureless due to the high density of MUMAS absorption features for polyatomic molecules. Therefore, it is desirable to have devices with a wide intermode-spacing so as to avoid congestion of too many features. A wider intermode-spacing has

the potential added benefit of it being more likely to have a point along the scan with full transmission of all modes which aids in determining the zero-absorption baseline of the spectrum.

There are physical limitations on the maximum intermode-spacing that is achievable. A larger intermode-spacing requires a shorter laser cavity and there are manufacturing limitations on how short a cavity can be made. Furthermore, a larger intermode-spacing means that the indices of the lasing modes are smaller, which means that in order to cover a full intermode-spacing during a scan, there must be a larger proportional change to the cavity length of the laser. Changes in the cavity length are effected by altering the driving current of the laser and the safe operating conditions of the laser might restrict the range of cavity length achievable by the laser, meaning that the cavity length cannot be changed sufficiently in order for the modes to scan across a full intermode-spacing. Finally, as with single-mode lasers, there is typically a finite MHF tuning range of a multi-mode laser. If the intermode-spacing becomes too large, it might surpass the MHF tuning range meaning that the laser will not scan predictably across a full intermode-spacing.

Thirdly, the bandwidth of the laser intensity envelope will affect the form of the MUMAS spectrum. A larger bandwidth will mean that many more molecular absorption transitions will be accessible. This broader spectral coverage is the main advantage of MUMAS over single-mode absorption spectroscopy. However, if the spectral coverage is too large, there will be too many MUMAS absorption features and the MUMAS spectrum will become too congested. Furthermore, if the intermode-spacing is kept fixed, then increasing the bandwidth will mean that there will be more modes and each mode of the laser will have a smaller proportion of the total power in the laser. This will result in smaller MUMAS absorption features, decreased SNR, and hence decreased sensitivity.

In summary, the optimal form of the laser intensity will differ depending on the desired application. The target species, their approximate mixing ratios, and their line-strengths

will influence both the intermode-spacing and the bandwidth of the laser.

3.6 Summary

This chapter discussed the theory of MUMAS, which is the spectroscopic technique used for all the work presented in this thesis. The basic theory of operation of the technique was discussed and further insights were given on the theory of tuning. These insights exposed inadequacies of the previous model, the translation-model, and a new model, the expansion-model, was devised.

Details of the translation-model were presented and the limitations of this model were discussed. The expansion-model was described, and the ways in which it overcame previous limitations were explained. The MUMAS Equation, which defines the position of the MUMAS absorption features, and which is also the basis of the expansion-model, was presented.

Brief details were given on the spectroscopic data modelling. Thorough details were given on the new computational model used for the expansion-model, including: the structure of the computational modelling process, the computational representation of certain aspects of the model, computational efficiency considerations and the advantages of the new model over the computational model for the translation-model.

The chapter concluded with a discussion of the theoretical and performance requirements for a multi-mode laser source for a MUMAS application. Although there are many rules-of-thumb for a multi-mode laser, the exact form of the optimal laser spectrum will differ depending on the application requirements.

Chapter 4

MUMAS with Interband Cascade Lasers

4.1 Overview

This chapter describes the work that was carried out using Interband Cascade Lasers (ICLs). The chapter begins by briefly describing these lasers, which were provided by the Naval Research Laboratory. The experimental apparatus and procedure is outlined, before the steps which are undertaken during the data processing are described. The method for ensuring that the frequency scale of the MUMAS spectrum is linear is explained in detail.

A key part of the MUMAS technique is the modelling and fitting routine. Modelled spectra are generated using the new expansion-model, which was described in chapter 3, and the parameters of the model are varied to provide an optimised fit to the data. The model requires accurate and precise knowledge of the laser parameters and therefore an explanation of how these are obtained is given. Furthermore, the fitting routine must take account of a few characteristics of the experimental data, and this chapter includes

a discussion of these considerations.

Details of all the results follow, and they form the bulk of this chapter. The analytical procedure for determining the individual mode-linewidths of the laser is presented. The first demonstration of MUMAS using an ICL is reported. The data are investigated further with the new expansion-model being validated by a MUMAS spectrum of more than one repeat-unit. A demonstration of enhanced spectral coverage with a single device follows, before species concentration measurements using MUMAS are shown. The multi-species capability of MUMAS is demonstrated before some consideration is taken for the Minimum Detection Limit (MDL) of the technique. Finally, detection of trace species in an atmospheric buffer pressure using ICLs with wide intermode-spacings is reported.

The chapter concludes with a brief discussion of the limitations of the technique at this stage in the thesis.

4.2 Interband Cascade Lasers

Interband Cascade Lasers (ICLs) are a novel type of laser that can produce continuous radiation in the mid-infrared region. The ICL generates gain via band-to-band recombination of electrons and holes, using an architecture consisting of a staircase of multiple active stages connected in series. The device may therefore be considered a hybrid of a conventional diode laser and an inter-subband-based QCL. ICLs display many of the advantages of QCLs whilst also providing continuous wave outputs at room temperature in the $3-6$ µm range. In addition, they have much lower threshold drive powers whilst giving output powers exceeding 500 mW [106–111].

Multi-mode laser sources that operate in the $3-4$ µm have a few advantages over similar devices which operate at longer mid-infrared wavelengths. This range includes

the region of the fundamental X-H stretch mode of many molecules including that of the C-H bond characteristic of many important hydrocarbon species. Furthermore, these strong absorption bands tend to lie closer in frequency space in the $3-4$ µm range – a feature which facilitates simultaneous detection of several species with a single, wide bandwidth, multi-mode source.

There are practical reasons why mid-infrared laser sources are not as common as their near-infrared counterparts. The majority of development has been done in the near-infrared region due to this being the optimum region for telecommunications since it is where both the optimum transmission window for silica optical fibres and the operational wavelength of erbium fibre-amplifiers are found. However, there are also some fundamental difficulties with developing lasers at longer wavelengths that must be overcome. In particular, both the Auger non-radiative decay rate and the internal loss associated with free-carrier absorption scale rapidly with increasing wavelength [112]. In Auger recombination, an electron in the conduction band recombines with a hole in the valence band and a phonon is released. These both affect the performance of the laser by requiring higher threshold current density. Characteristic features, such as internal carrier generation and transport processes of an ICL are designed to overcome these challenges, and ICLs have been shown to be somewhat independent of threshold current density when operating between $3-6$ µm [113].

To understand the operation of ICLs, it is instructive to first consider the operation of both conventional diode lasers and QCLs. In conventional diode lasers, electrons are injected into the conduction band from one contact and holes are injected into the valence band at the opposite contact. The minimum threshold voltage, V_{th}, scales with the photon energy. In a QCL, the current flow is entirely due to electrons which pass through each active quantum well. This reduces the threshold current density at the expense of a higher threshold voltage which must exceed MV_{th}, where M is the number

of stages.

Like QCLs, ICLs employ the concept of band-structure engineering to achieve an optimised laser design and re-use injected electrons to emit multiple photons. However, in contrast to a conventional diode laser and a QCL, an ICL generates both electrons and holes internally at each successive stage. To replenish the carriers removed by the field, equal numbers of additional electrons and holes must be regenerated continuously at each successive stage. With this modification, ICLs are able to produce continuous wave radiation in the mid-infrared region, with low power requirements at room temperature [114]. These benefits have enabled a portable device using ICLs to be recently used for the detection of CH_4 at ppmv levels [115]. They also make ICLs a suitable option for use in MUMAS.

The work described in this chapter uses a multi-mode narrow-ridge ICL grown and processed by the Navel Research Laboratory (NRL). The ridge width of 10 µm and cavity length of 4 mm provide an intermode-spacing in the range $9.7 - 9.8$ GHz. With a voltage of 3.3 V driving a current of 500 mA, equivalent to a power consumption of 1.65 W, an output power of 90 mW is available. In practice, however, only 0.01 mW is used in experiments in order to avoid saturating the detectors. Temperature control to maintain the device at 30°C requires an additional power of about 1 W. Recent developments at NRL have demonstrated devices with power consumption up to 50 times lower than that of the device used here [113]. Thus, MUMAS-based detector systems using ICLs with low power requirements could be suitable for gas sensing applications in the field. They have also been demonstrated to have an exceptionally long lifetime at room temperature, a prerequisite for an inexpensive laser capable of operating without thermo-electric cooling in field environments [116].

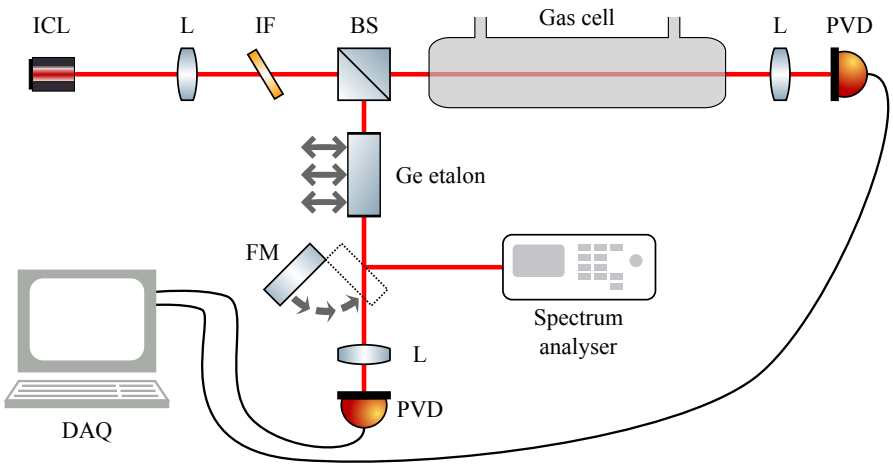

Figure 4.1: Experimental setup used for MUMAS with ICLs. L: lens, IF: interference filter, BS: beam splitter, FM: flip-mirror, PVD: photovoltaic detector, DAQ: data acquisition.

4.3 Experimental apparatus and procedure

The theory of operation of the MUMAS technique is described in section 3.2. This section describes the standard apparatus and procedure which is used to obtain experimental MUMAS spectra. The experimental details are given in section 4.3.1, before the data processing is described in section 4.3.2. This section concludes with a description of the method used to linearise the frequency scale of a MUMAS spectrum.

4.3.1 Apparatus

A standard optical setup is used to measure the transmission through samples of the target gases using direct absorption spectroscopy. A schematic of this experimental setup using ICLs is shown in figure 4.1.

The ICL is powered by a low-noise QCL current-driver (Wavelength Electronics QCL1000) and the temperature is maintained at 27.5°C by a TEC temperature controller (Thorlabs TED 200C).

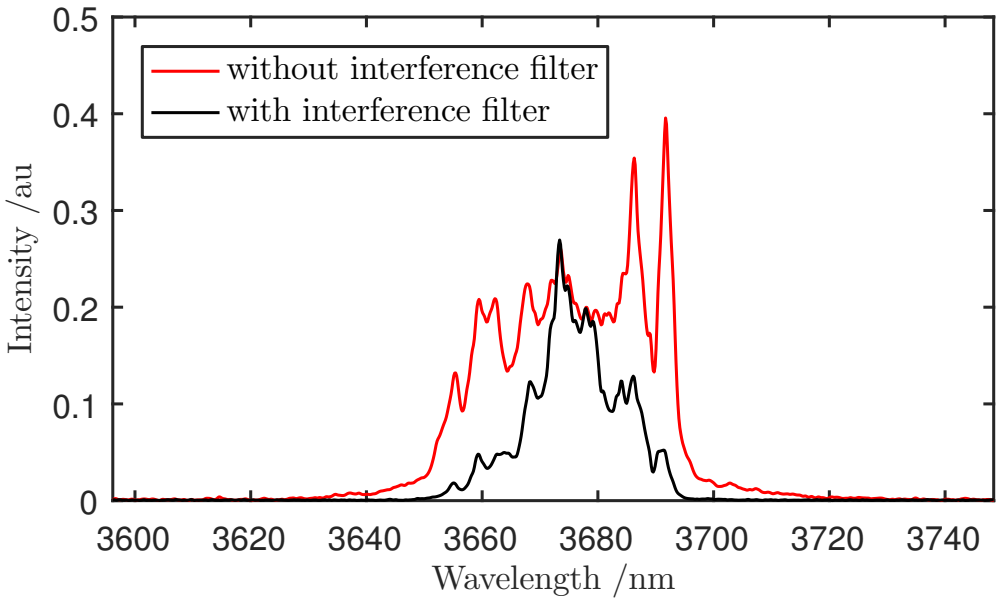

Figure 4.2: Intensity envelope of the laser spectrum with and without an interference filter. The intensity envelope has a much simpler form with the interference filter in place than it does without it. Note that the modes are not individually resolved as the resolution limit of the spectrum analyser is greater than the intermode-spacing.

The output of the ICL has a broad spectral range and it is not possible to represent the intensity envelope with a simple analytic function. In order to avoid the MUMAS spectrum becoming too dense with absorption features due to the surplus number of modes, an interference filter (Northumbria Optical Coatings) is used to select a small segment of the mode-spectrum. The centre of the band pass is adjusted by varying the angle of incidence of the filter. In the earlier versions of the modelling, this interference filter also enabled a simple analytical expression for the intensity envelope to be used. However, developments to the model allow the exact mode intensity envelope, recorded using a Michelson Interferometer, to be directly used for the laser intensity envelope in the model. The mode-spectrum, with and without the interference filter, is shown in figure 4.2. It is clear that the intensity envelope has a much simpler form with the interference filter in place than it does without it. The intensity envelope is centred

around ~ 3670 nm.

Despite the total intensity of the ICL being temporally stable (coefficient-of-variation $= 4.2 \times 10^{-4}$), the power in each mode fluctuates. Therefore when the interference filter is used, the total power of the modes passing through the interference filter also fluctuates, thereby adding noise to the signal. However, the magnitude of this noise is sufficiently low (coefficient-of-variation $= 3.7 \times 10^{-3}$) that it does not overwhelm the absorption features at the pressures of gases being detected in this experiment.

The output beam of the ICL, after being filtered by the interference filter, is split using a CaF_2 plate beam splitter (BSW510, 55:45 split ratio) to provide two beams: a probe beam and a reference beam. The reference beam is used to monitor the incident intensity on the absorption cell whilst the probe beam passes through a sample of gas contained in a pressure-controlled cell. Intensities of the probe and reference beams are measured using photo-voltaic devices (Vigo Systems, model PVI-2TE-4) and the time-varying intensity is recorded using a digital acquisition device (Handyscope HS5). The intensity of the reference beam is used to normalise the absorption signal for laser intensity variations. Two different single-pass gas cells are used for the work in this chapter: a stainless steel gas cell with a length of 0.8 m is used for the results in sections 4.5.2 and 4.5.3 and a glass gas cell with a length of 0.37 m is used for all other experiments.

In order to effect the scan of the multi-mode laser comb, a ramp current from a signal generator (Agilent 33500B Series) is applied to the ICL driver current. The modulation frequency of this scanning is different for each experiment and is noted in the corresponding sections. As described in section 3.3, this scanning originates from the modulation of the optical length of the laser cavity, and by extension, the modulation of the intermode-spacing. As the intermode-spacing increases, the mode structure expands and the modes are effectively swept across the frequency scale. All the modes of the laser are scanned across a full intermode-spacing, and a record of the variation of transmitted

power during this scan constitutes the MUMAS spectrum. In this way, the entire range of the spectrum covered by the broadband output of the laser is interrogated. However, as is shown in further work (chapter 6), it is also possible to record, and subsequently fit, a MUMAS spectrum corresponding to a scan across a part of an intermode-spacing.

Along with effecting the scan of the modes, the temperature and injection current settings of the laser also causes the gain curve of the laser to vary. Due to this, the interference filter is especially useful for maintaining a constant laser intensity envelope as the ICL driver current is scanned. The central wavelength of the ICL emission can be varied by a combination of temperature and injection current settings over a range from 3620 to 3770 nm. Thus, by a combination of current/temperature tuning and adjustment of the interference filter, different spectral envelopes can be selected.

As the response of the optical length of the cavity to the scanning-ramp of the ICL driver current is non-linear, it is necessary to monitor the frequency scan in order to produce a linear frequency scale for the MUMAS spectrum. A germanium etalon with a FSR of $\sim$ 500 MHz is used to produce a fringe pattern during the scan, the peaks of which act as markers with which to equally distribute and thus linearise the scan (section 4.3.3). The etalon is removed whilst performing MUMAS as it is used only for diagnostic purposes and does not form part of the apparatus required to perform MUMAS.

For further characterisation purposes, a Michelson Interferometer (Bristol Instruments, 721-B IR) is used to investigate the form of the intensity envelope during scanning, but does not form part of the apparatus required to perform MUMAS. The beam is directed into the Michelson Interferometer using a flip-mirror situated before the gas cell. As described above, developments to the model allow the exact mode intensity envelope, recorded using this Michelson Interferometer, to be used for the mode intensity envelope in the model. The measurement is made only once as the output spectrum is found to

be reproducible.

Before performing spectroscopy, the gas cell is repeatedly flushed with nitrogen and evacuated using a rotary vacuum pump (Edwards E2M5) to remove any traces of contaminating gases. Nitrogen does not absorb in this region. To produce a sample for measurement, different gases are added to the cell with low partial pressures. The pressure at each stage is recorded using a capacitance manometer (Setra 730, quoted accuracy 0.25% down to a pressure of 0.025 mbar). For all the partial pressure values presented in this chapter, the uncertainties in the measured pressures are derived from the uncertainties in the readings from the capacitance manometer, and the uncertainties in the fitted pressures are derived from the range of values corresponding to a $\pm 5\%$ deviation in χ^2 from the best-fit value.

4.3.2 Data processing

The data obtained from the experiment have to be processed before any model fitting can be performed. MUMAS spectra are calculated as the ratio of the measured intensity of the probe and reference beams. A subset of MUMAS spectra are averaged to reduce the impact of experimental fluctuations, with the exact number in each subset being noted in the corresponding sections. Sloping baselines or stable baseline artefacts, arising from differences in the beam paths after the beam splitter which are not attributable to the absorbing species, are removed by dividing the MUMAS transmission signal by the transmission signal of an empty gas cell. The data is recorded with a time basis. This time-basis is transformed to a frequency-scanned basis by using the etalon spectrum obtained with the germanium etalon, the method of which is described in section 4.3.3. This etalon spectrum also serves to 'linearise' the data so that the MUMAS spectrum is presented on a linear frequency-scanned scale. Finally, a Fourier low-pass frequency filter is applied to the data to attenuate high frequency detector noise. However, this

frequency filter is purely for aesthetic purposes and does not affect the values obtained from fitting to the data.

In practice, all the modes are allowed to exceed a scan of one intermode-spacing by a factor of approximately 1.5. This is because the scanning behaviour of the modes mostly deviates from linearity at the extremities of the scan, and a segment of length equal to one intermode-spacing can thus be chosen to mainly avoid these non-linear regions. Furthermore, identifying repeat MUMAS features between consecutive segments of one intermode-spacing aids in accurately selecting a MUMAS spectrum with a frequency scale which is one intermode-spacing in length. Although this is helpful, it is also possible to record, and subsequently fit, a MUMAS spectrum corresponding to part of an intermode-spacing, as shown in the work in chapter 6.

4.3.3 Linearisation of MUMAS frequency scale

In order to effect the scan of the multi-mode laser comb, the optical length of the laser cavity is scanned by applying a triangular wave modulation to the ICL current driver. Although this current modulation is linear, the frequency response to it by the multi-mode laser comb is not linear – the modes do not scan in frequency at a constant rate. As was described in section 3.3, a linear response is only expected to a first approximation due to the underlying physics, and this is one reason for some of the non-linear response. However, the main reasons for this non-linear response are the delayed response time of the laser cavity to the driver and hysteresis effects in the laser cavity.

In order to correct for this non-linear response, the fringe pattern of a germanium etalon is used to monitor the frequency scan of the laser. The peaks of the fringe pattern act as markers at constant wavenumber intervals with which to linearise the scan.

In order to utilise the spectrum obtained using an etalon, the theory of the etalon needs to be considered. The transmittance function, T, of an etalon is defined in equation 4.1,

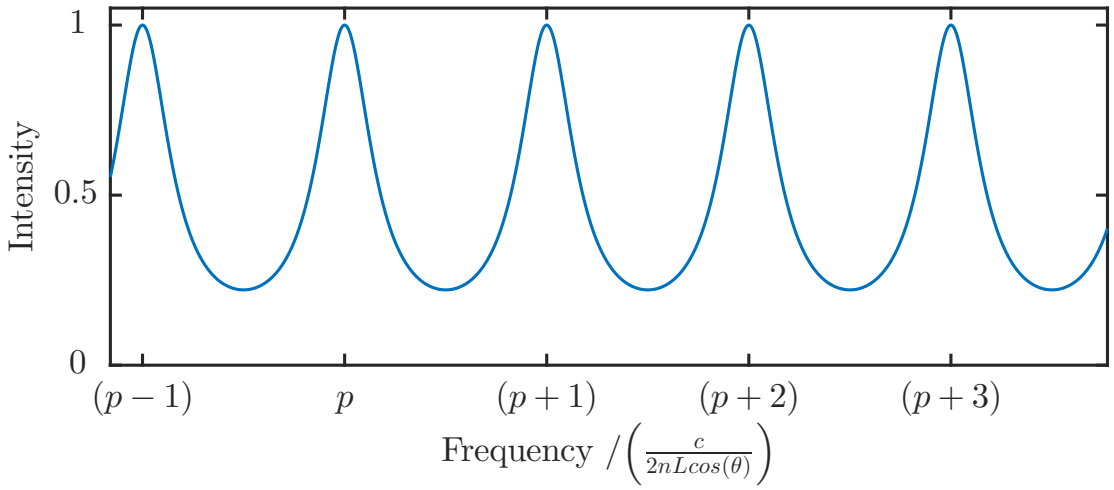

Figure 4.3: A Fabry-Perot fringe pattern for $R = 0.36$, using equation 4.1.

where δ is the net phase-difference between two adjacent beams and $\mathcal{F}$ is the finesse.

$$T = \frac{1}{1 + \mathcal{F}\sin^2\left(\frac{\delta}{2}\right)}\,. \tag{4.1}$$

The finesse is defined by the reflectance of the etalon surface, R, and is given by equation 4.2.

$$\mathcal{F} = \frac{4R}{(1-R)^2}\,. \tag{4.2}$$

The phase-difference is defined by equation 4.3, where ν is the frequency of light, n is the refractive index of the etalon, L is the length of the etalon and θ is the angle of refraction in the etalon.

$$\delta = \left(\frac{2\pi\nu}{c}\right) 2nL\cos\theta\,. \tag{4.3}$$

A Fabry-Perot fringe pattern is usually observed by varying either the optical length of the etalon or the frequency of the incident light. The Fabry-Perot fringe-pattern

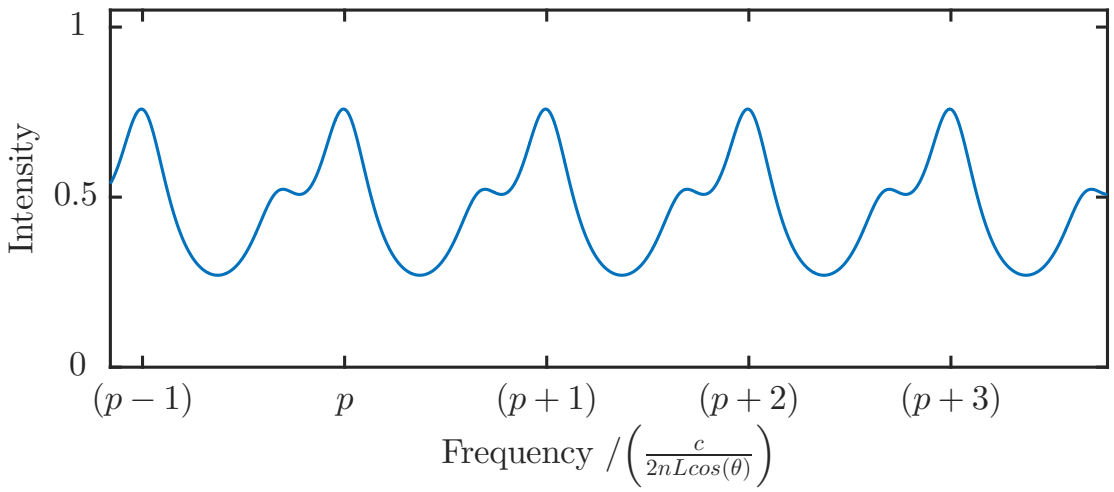

Figure 4.4: The etalon pattern which would result from two modes, one of which has twice the intensity of the other, and which also has a frequency offset equal to one third of the intermode-spacing.

formed by scanning the frequency of a single mode of light is shown in figure 4.3. where p indicates the index of the fringe. The separation of the fringes is known as the Free Spectral Range (FSR). The fringe-pattern illustrated in figure 4.3 is for a single-mode laser. However, in the case of a laser with multiple modes, such as the ICL used in this work, the resulting interferogram will be a superposition of the fringe pattern from each individual mode.

Figure 4.4 is the etalon pattern which would result from two modes, one of which has twice the intensity of the other, and which also has a frequency offset equal to one third of the intermode-spacing. It is clear that for the case of two modes, the resulting interferogram is more complicated than a simple fringe pattern. However, despite the peaks no longer being separated in frequency by the FSR of the etalon, this structure still provides information with which to linearise the scan. Further modes will produce an increasingly complicated interferogram.

Figure 4.5 is the etalon pattern which would result from 50 modes of equal intensity and with a frequency offset between consecutive modes which is equal to one third of the

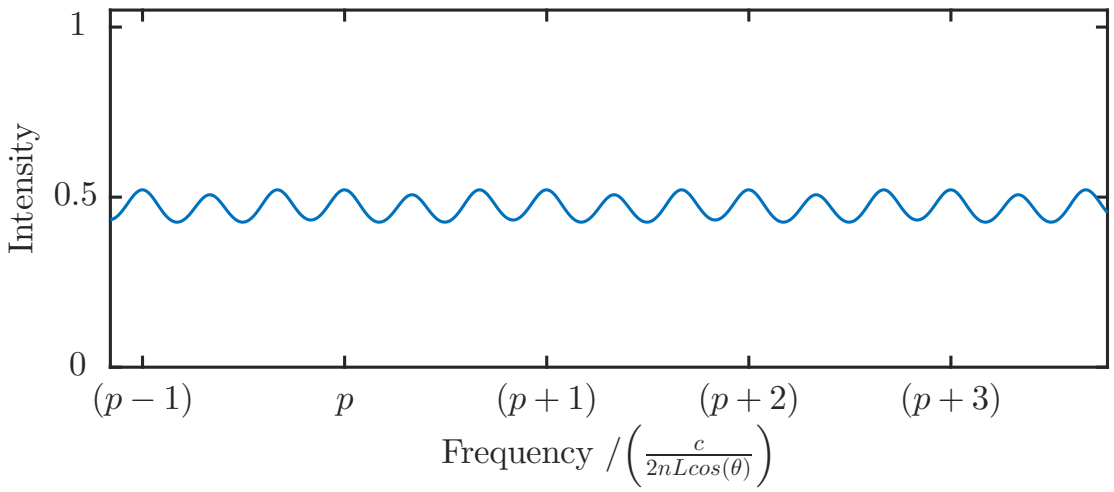

Figure 4.5: The etalon pattern which would result from 50 modes of equal intensity and with a frequency offset between consecutive modes which is equal to one third of the intermode-spacing.

intermode-spacing. As the intermode-spacing is uniform across the spectrum, the relative frequency offset of the fringe pattern for consecutive modes is the same. This results in the existence of a repeating structure in the interferogram. Despite the modulation depth of the repeating pattern decreasing and the peaks no longer being separated in frequency by the FSR of the etalon, this structure provides information with which to linearise the scan.

One method of using this experimental etalon spectrum to linearise the scan is to identify the fringes which are common to a particular mode, fit a polynomial through the position of these fringes and use this polynomial to linearise the data. This was the method used in previous work [7]. However, this only utilises a small amount of the information available. Alternatively, by using all the data in the interferogram, it is also possible to fully linearise the segments between each peak. For this new method, time-frequency analysis is used to calculate the dominant frequency in the power spectral density of a windowed segment of the total spectrum. The selected segment moves across the data and therefore the frequency of the interferogram across the pattern is extracted.

If the frequency of the modes were to scan linearly, the dominant frequency in each power spectral density would remain constant as the windowed section moves across the spectrum. However, as the scan is not linear, the dominant frequency will not be constant, and its variation will reflect the non-linearity of the scan. Thus, the resulting relationship between the dominant frequency and the position along the scan can be used to linearise the scan. This is the method used to linearise the MUMAS spectra reported in this thesis.

4.4 Fitting the model to experimental data

An experimental MUMAS spectrum encodes information on the identity of the species in the sample, its partial pressure and the temperature and ambient pressure of the bulk gas. By modelling a MUMAS spectrum and fitting to the experimental MUMAS spectrum, these various parameters can be inferred. For the work in this thesis, a new theoretical- and subsequent computational-model are developed in order to incorporate the new expansion-model and the MUMAS Equation, details of which are given in chapter 3.

To produce a fit of the model to the experimental data, the experimental process is forward-modelled and then fitted to the experimental data in an iterative manner. The parameters are inferred by those which produce a modelled MUMAS spectrum with the best-fit to the experimental data. The ultimate aim of the technique is to infer the partial pressure and temperature of the target species or bulk gas. A complete spectral database of the species being probed and a robust fitting algorithm are both necessary to infer these parameters. An initial estimate of the laser parameters is also useful in aiding the process. However, due to some of the laser and gas parameters being orthogonal in how they affect a MUMAS spectrum, precise, a priori values of the laser parameters are not strictly necessary.

4.4.1 Determing the laser parameters

In order to produce a model of the MUMAS spectrum, values for the parameters of the probing laser are necessary. Specifically, the laser parameters that determine the form of the laser spectrum are the absolute frequencies of the modes, ν_q, the intermode-spacing, $\Delta\nu_{\text{mode}}$, the individual mode-linewidth, $\delta\nu$, and the intensity envelope of the laser modes, $E(\nu)$. Each of these parameters can be measured by a spectrum analyser, and it has been found that these measurements only need to be measured once as the laser spectrum is reproducible. Although the spectrum analyser provides good knowledge of the laser parameters, the precision is normally insufficient to produce an accurate MUMAS spectrum. Fortunately, due to some of the laser and gas parameters being orthogonal in how they affect a MUMAS spectrum, these coarse measurements of the laser parameters can be refined by using the MUMAS model to fit them.

Intermode-spacing, $\Delta\nu_{\text{mode}}$

The most critical laser parameter is the intermode-spacing and the form of a MUMAS spectrum is very sensitive to it. A small change in the magnitude of the intermode-spacing can substantially change the form of a MUMAS spectrum. Commercial spectrum analysers are particularly inadequate for measuring the intermode-spacing to sufficient accuracy and precision as the resolution limit of typical commercial devices is larger than the intermode-spacing of the devices used for the work in this thesis. This is apparent in figure 4.2. Instead, an estimate for the intermode-spacing can be obtained by determining the optical length of the cavity and using equation 3.3 to convert this to an estimate of the intermode-spacing. This value can be refined by fitting an experimental MUMAS spectrum obtained from a calibrated sample, and using the intermode-spacing as one of the fitting parameters.

Intensity envelope, $E(\nu)$

In earlier work, the intensity envelope was modelled as a truncated Lorentzian and empirically defined by both the Lorentzian FWHM and the envelope-base-threshold, where the envelope-base-threshold is the fraction that is cropped from the bottom of the Lorentzian lineshape. This truncation ensured that the envelope had a finite extent in frequency, and was also found to provide a good fit to the intensity envelope of the mode spectrum. A form of this truncated Lorentzian was fitted to the intensity spectrum obtained from the spectrum analyser. However, developments to the model allow the exact laser mode intensity envelope, recorded using a Michelson interferometer, to be directly used for the mode intensity envelope in the model. As only the relative intensities of the modes are necessary for the model, the absolute intensity of the laser mode intensity envelope is not necessary. The precision in the relative intensity measurements of the Michelson interferometer is sufficient for measuring the laser mode intensity envelope, and this measured spectrum is used directly in the MUMAS modelling.

Mode-linewidth, $\delta\nu$

The mode-linewidth is the least critical parameter when modelling a MUMAS spectrum – it is usually much smaller than the other broadening mechanisms and will often have negligible effect on the overall MUMAS spectrum. However, it is still important to measure it for each device to ensure that the mode-linewidth of each device will have negligible effect on a MUMAS spectrum. The individual modes of the probing laser have a finite spectral width, and this in turn contributes to the spectral width of the measured MUMAS absorption features. In previous MUMAS work, a high-finesse etalon with a well defined FSR was used to determine the mode-linewidth. The individual modes of the laser produce their own etalon fringe pattern, and provided that the finesse of the etalon

is high enough, consecutive fringes from a single mode are resolved, and hence identified. The output from a spectrum analyser is on an arbitrary frequency scale. Therefore, the absolute mode-linewidth is calculated by determining the ratio of the FSR to the mode-linewidth on this arbitrary frequency scale, and comparing it to the same ratio on an absolute scale where the absolute value of the FSR is precisely known.

The low finesse of the germanium etalon used in this experiment coupled with the large number of modes for the laser means that the individual modes are not resolved. Therefore, due to overlapping fringes, individual fringes are not able to be identified. Consequently, in order to measure the mode-linewidth of the lasers used in the work in this chapter, an alternative method is used which involves measuring the spectral width of the MUMAS feature of a HCl spectrum and extracting the laser mode-linewidth contribution from this spectral width. It is described further in section 4.5.1, below. Using this method, the mode-linewidth is found to vary with injection current from 10 to 80 MHz. Beyond the work in this chapter, a further method is devised and it is described in chapter 5.4.

Mode frequencies, ν_q

The approximate value for the absolute frequencies of the modes can be found using a spectrum analyser. However, as described in section 3.2, due to the repetition inherent in a MUMAS spectrum, changing the exact spectral location of the modes does not change the form of the MUMAS spectrum, but instead only produces a cyclic shift of the MUMAS spectrum. Therefore, the exact spectral position of the modes is not necessary for the model.

4.4.2 Additional fitting parameters

Along with laser parameters, spectral information and gas parameters, there are a few additional 'technical' parameters which are necessary to consider in the computational model in order to accurately model experimental MUMAS spectra.

As mentioned above, due to the repetition inherent in a MUMAS spectrum, changing the exact spectral location of the modes does not change the form of the MUMAS spectrum, but instead only produces a cyclic shift of the MUMAS spectrum. To ensure that the modes for the experimental and modelled spectra have the same starting point, it is necessary to experimentally determine the exact starting position of the modes at the start of a scan. However, the experimental precision that is necessary for this is impractical. Therefore, when modelling a MUMAS spectrum, it is likely that the modelled MUMAS spectrum will have a frequency offset from the experimental MUMAS spectrum. This frequency offset is the difference between the experimental and modelled frequency positions of the modes at the start of the scan. To overcome this, when fitting an experimental MUMAS spectrum that is a scan over one intermode-spacing, the fitting routine will generate a modelled MUMAS spectrum that is a scan over two intermode-spacings. A cross-correlation between the experimental and modelled MUMAS spectra is subsequently used to determine the segment of the modelled MUMAS spectrum that corresponds to the experimental MUMAS spectrum.

In practice, MUMAS spectra are recorded by modulating the driving current of the laser and hence sweeping the set of laser modes. However, a positive increase in driving current does not necessarily correspond to a positive increase in frequency of the modes. For some devices, the intermode-spacing decreases with increasing driving current, and hence the frequency position of the modes decreases with increasing driving current. This results in a reversed MUMAS spectrum. To accommodate this, the cross-correlation

process described above is also repeated with the experimental data reversed on its frequency axis so as to determine the correct direction of the frequency scan in the experiments.

When processing the data, due to the imperfect linearisation process, it is difficult to select a spectrum which is exactly one intermode-spacing in length. This problem is exacerbated when fitting to determine the intermode-spacing – when doing so, it is necessary to select slightly different lengths of experimental data when comparing with different modelled MUMAS spectra which have different intermode-spacings in the fitting routine. The solution is to purposely select a spectrum which is slightly more than one intermode-spacing in length (usually about 2% more). Subsequently, when fitting to each modelled MUMAS spectrum, the portion of this experimental data which is selected is allowed to vary in the fitting routine (usually from 95% to 100%). In this way, a spectrum corresponding to exactly one intermode-spacing will be generated as it will produce the lowest error signal and the best-fit to the data.

Finally, as is common in absorption spectroscopy, determining the zero-absorption level of an experimental MUMAS spectrum is difficult. This is especially difficult for MUMAS due to the density of features in a MUMAS spectrum – it is often the case that there is no position in the spectrum with zero-absorption. Furthermore, experimental drifts can cause the ratio of the reference- to probe-intensities to drift slightly over time, and therefore the zero-absorption levels, modulo one, may not be at exactly zero. To account for this, a small offset value (typically within the range $\pm 10^{-3}$) is added to the experimental MUMAS spectrum and allowed to vary in the fitting routine.

4.4.3 Fitting procedure

Knowledge of the laser parameters combined with a spectral database of the species of interest enables a MUMAS spectrum to be modelled. This modelled MUMAS spectrum

can be fitted to the data in order to infer properties of the gas sample. In order to measure the quality of a fit to experimental data, a metric must be devised. This metric is known as an error-signal. The properties of the laser and the gas sample can be varied in the model in order to minimise the error-signal, and hence improve the quality of the fit.

In this work, the error-signal is defined as the least-squares difference between the experimental- and modelled-spectra. For a given set of laser and gas parameters, $\mathbf{x}$, the difference between an experimental MUMAS spectrum, T^E, and a modelled MUMAS spectrum, T^M, for a given point, j, is given by a residual vector, r_j, as shown in equation 4.4. The index, $j = 1, 2, \ldots m$, runs over a discrete set of points which are the sampling points of both the experimental and modelled MUMAS spectra.

$$r_j(\mathbf{x}) = T_j^M(\mathbf{x}) - T_j^E . \tag{4.4}$$

The error-signal, $\mathcal{E}$, is defined as the weighted sum of the square of these residuals divided by the sum of the weightings, as given in equation 4.5. The weighting factor of each element, w_j, allows for the importance of certain features in the MUMAS spectrum to be specified. The default setting is to have no weighting, and therefore they are all set to one. The division by the sum of the weightings is required in order to enable the error-signal to be compared between data sets with different sampling rates.

$$\mathcal{E}(\mathbf{x}) = \frac{\sum_{j=1}^{m} w_j r_j^2(\mathbf{x})}{\sum_{j=1}^{m} w_j} . \tag{4.5}$$

The fit to the data is optimised by varying the parameters to minimise the error-signal. This minimisation is a non-linear least squares problem. In general, the fitting surface of such a problem will contain many local minima in addition to the global minimum, and finding the global minimum is therefore difficult.

The fitting surface for the partial pressure of the sample species tends to be monotonically varying. It is only when fitting the laser parameters, and the intermode-spacing in particular, that a fitting surface with local-minima results. When fitting laser parameters, it is therefore necessary to have an exhaustive search of the parameters, and accordingly, a finely-sampled grid of points of the parameters are probed with the error-signal being calculated for each point. In this way, the fitting routine will be immune to any local minima and will find the global minimum provided that it exists within the grid of probed points. This method is inherently time-consuming, yet robust, and therefore it is useful for characterising the laser parameters to a high precision.

When using the model to fit the partial pressure of a sample of gas, it is more efficient to use an optimised minimisation algorithm. The work in this thesis uses a non-linear least squares fitting algorithm, *fminsearch*, available in MATLAB, which is optimised to efficiently find the minimum of monotonically varying fitting surfaces [117]. It samples fewer points than the exhaustive method and it therefore takes less time.

Despite being much faster than an exhaustive parameter search, when fitting a large set of spectra, the *fminsearch* fitting algorithm is still time consuming. This is particularly problematic when analysing the spectra for the Allan variance studies in section 4.5.7, in which thousands of spectra need to be analysed. The most time consuming part of the fitting is the process of generating the modelled MUMAS spectra for each probed set of parameters. By using the *fminsearch* fitting algorithm for many spectra, similar modelled MUMAS spectra would be repeatedly generated, fitted, and subsequently discarded. An alternative fitting routine is developed to avoid this repetitive modelling. A large dataset of modelled MUMAS spectra, each with a different sets of parameters, is generated and saved for all future fitting. This dataset acts as a lookup table. The error-signal for the experimental MUMAS spectrum and each of the modelled spectra in the dataset can therefore be quickly generated and the global minimum easily found. This same

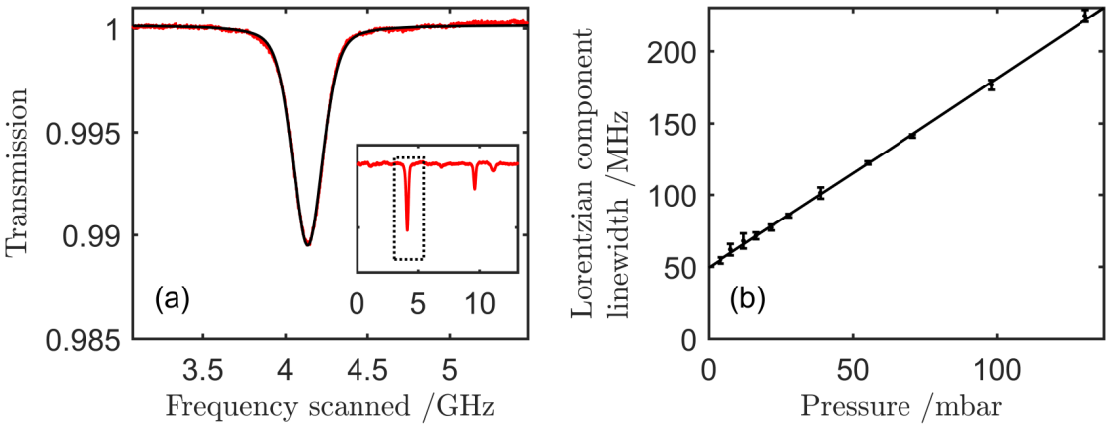

Figure 4.6: The inset of panel (a) shows the entire MUMAS spectrum of HCl using the filtered output of the ICL – two well-isolated lines are observed. The main figure shows an enlarged view of the single feature highlighted by the dashed box in the inset together with with a fitted Voigt lineshape. The red line is the experimental data, and the black line is the fitted Voigt profile. Panel (b) shows a plot of the Lorentzian component of the MUMAS absorption feature linewidth versus pressure. A line-of-best-fit through these points is used to determine the linewidth at zero pressure and hence the laser mode-linewidth, $\delta\nu$.

dataset is used for multiple sets of experimental spectra, hence avoiding repeatedly generating similar MUMAS spectra. The lookup operations are based on linear algebra, which MATLAB is optimised for, and therefore this fitting routine is exceptionally faster than both the exhaustive and non-linear least squares fitting routines. When the laser parameters are found, this lookup method is the fitting method of choice for gas sensing with MUMAS.

4.5 Results

4.5.1 Linewidth measurements

The mode-linewidth contributes towards the spectral width of measured MUMAS absorption features and it limits the ultimate spectral resolution of the MUMAS technique. However, in practice, the mode-linewidth is usually much smaller than the spectral

width of the MUMAS absorption features being detected and so its value is not critical. Nonetheless, it is important to measure it for the ICL used for the work in this chapter to ensure that it has negligible effect on MUMAS spectra. The mode-linewidth is measured using MUMAS spectra of a molecule with widely spaced absorption lines so that a feature can be identified as arising from the interaction between a single individual mode and one spectral line. At the operating wavelength of the ICL used, HCl provides a suitable, open absorption spectrum. Thus, the mode-linewidths are found by measuring lineshapes of single isolated absorption features of HCl in the region $3.6 - 3.7$ µm. Conventional MUMAS absorption spectra are recorded by measuring the ratio of transmitted to incident intensity of the ICL radiation through a glass gas cell of length 0.37 m containing HCl broadened by various buffer pressures of N_2. The bandwidth of the ICL emission is limited by transmitting the beam through an interference filter to produce a spectrum of width ~ 27 cm^{-1}. Since the absorption spectrum of HCl in the region of $3.6 - 3.7$ µm is fairly open, only two, widely separated, and hence isolated, absorption lines lie within the bandwidth of the filtered laser emission, as shown in the inset of figure 4.6a. Thus, when all the longitudinal modes of the ICL are scanned across the intermode-spacing, $\Delta\nu_{\text{mode}}$, only two absorption lines are observed, each probed by a different longitudinal mode of the laser. The two features in this simplified MUMAS spectrum are sufficiently well separated that no overlap occurs to distort the individual lineshapes.

The main plot in figure 4.6a shows a single feature in the MUMAS spectrum of HCl together with a fitted Voigt profile. The fitted Voigt lineshape, after deconvolution of the Gaussian, Doppler component, is assumed to be the result of a Lorentzian mode-lineshape and a Lorentzian pressure broadened lineshape. The natural width (of order 1 Hz) is insignificant relative to the pressure-broadened and Doppler widths. The Gaussian component is calculated from Doppler broadening of the HCl absorption line at room temperature, and is found to be 166 MHz. The width of the Lorentzian component is

measured, for a fixed injection current, as a function of N_2 buffer pressure between 5 and 130 mbar. An example of these data is shown in figure 4.6b for a drive current of 476 mA. The limit of the Lorentzian linewidth as the pressure tends to zero is found in this way to vary with injection current from 10 to 80 MHz. By tuning the spectral envelope, it is possible to verify that the mode-linewidth is not significantly different for the modes at the centre and edges of the mode spectrum. For the work reported in this chapter, the current is set to $\sim$ 550 mA with a corresponding mode-linewidth of about 20 MHz.

4.5.2 Mid-infrared MUMAS spectrum of methane

The red line in figure 4.7a shows the experimental MUMAS spectrum of methane obtained using a multi-mode ICL centred at 3.7 µm. This is the first demonstration of MUMAS using ICLs. Methane is chosen as it has sufficiently strong transitions in the spectral range of this device, and therefore provides a suitable species for this proof-of-concept demonstration. In this experiment, the modes are scanned at a rate of 10 Hz and a single-pass stainless steel absorption cell of length 0.8 m is used. In addition to a trace amount (0.2 mbar) of N_2, the partial pressure of CH_4 permitted into the cell is 2.89 ± 0.01 mbar. The mode spectrum of the ICL contains over 65 modes and the experimentally determined envelope covers a range of 30 nm. As described in section 4.4, an estimate for the intermode-spacing is obtained by determining the optical length of the cavity and using equation 3.3 to convert this to an estimate of the intermode-spacing. The cavity length is approximately 4 mm and the manufacturer estimates the refractive index of the standard structure of the gain medium to be $\sim$ 3.57, thus giving an approximate value for the intermode-spacing of 10 GHz. This value is refined by fitting an experimental MUMAS spectrum obtained from a calibrated sample, and using the intermode-spacing as one of the fit parameters. It is found to be 9.7972 ± 0.0003 GHz. The uncertainty value is based on the range giving 5% deviation from the minimum of the χ^2 in the fitting

procedure.

The best-fit modelled MUMAS spectrum is also shown in figure 4.7a as a black line. The residuals for this fit are shown in figure 4.7b. The modelled spectrum allows identification of the transitions of CH_4 which contribute to each feature in the experimental spectrum. For illustrative purposes, these transitions are displayed as a more conventional spectrum in figure 4.7c, which is shown together with a schematic representation of the multi-mode ICL spectrum used to record the spectrum. Due to the large bandwidth of the ICL, transitions of methane spanning a range of ~ 40 nm (~ 1 THz) are detected. This wide laser spectrum illustrates the ability of MUMAS to record widely separated spectral features, a property which allows detection of multiple species having widely separated absorption lines.

The concentration, or partial pressure, of the sample of CH_4 is determined to be that giving the best-fit to the data. Using this method, the CH_4 partial pressure is determined to be 3.03 ± 0.13 mbar, which agrees within experimental uncertainty with the value of 2.89 ± 0.01 mbar measured using the capacitance manometer. Systematic errors in the derived absolute concentration, such as the presence of residual air in the gas-handling system, can be reduced by a calibration procedure.

Although some sensing applications allow analysis at low pressure, it is instructive to consider detection of species with congested spectra at atmospheric pressure. The work in this section uses low pressure to illustrate the spectral resolution but also because the ICL device available has a relatively narrow intermode-spacing of approximately 10 GHz. With such a small value for $\Delta\nu_{\text{mode}}$, the pressure broadening of a congested spectrum by atmospheric pressure would result in a generally featureless MUMAS spectrum. The solution to this problem is to use an ICL with a wider intermode-spacing. This will decongest the MUMAS spectrum, and hence will enable a MUMAS spectrum with distinctive features to be obtained at atmospheric pressure. In section 4.5.8 it is shown

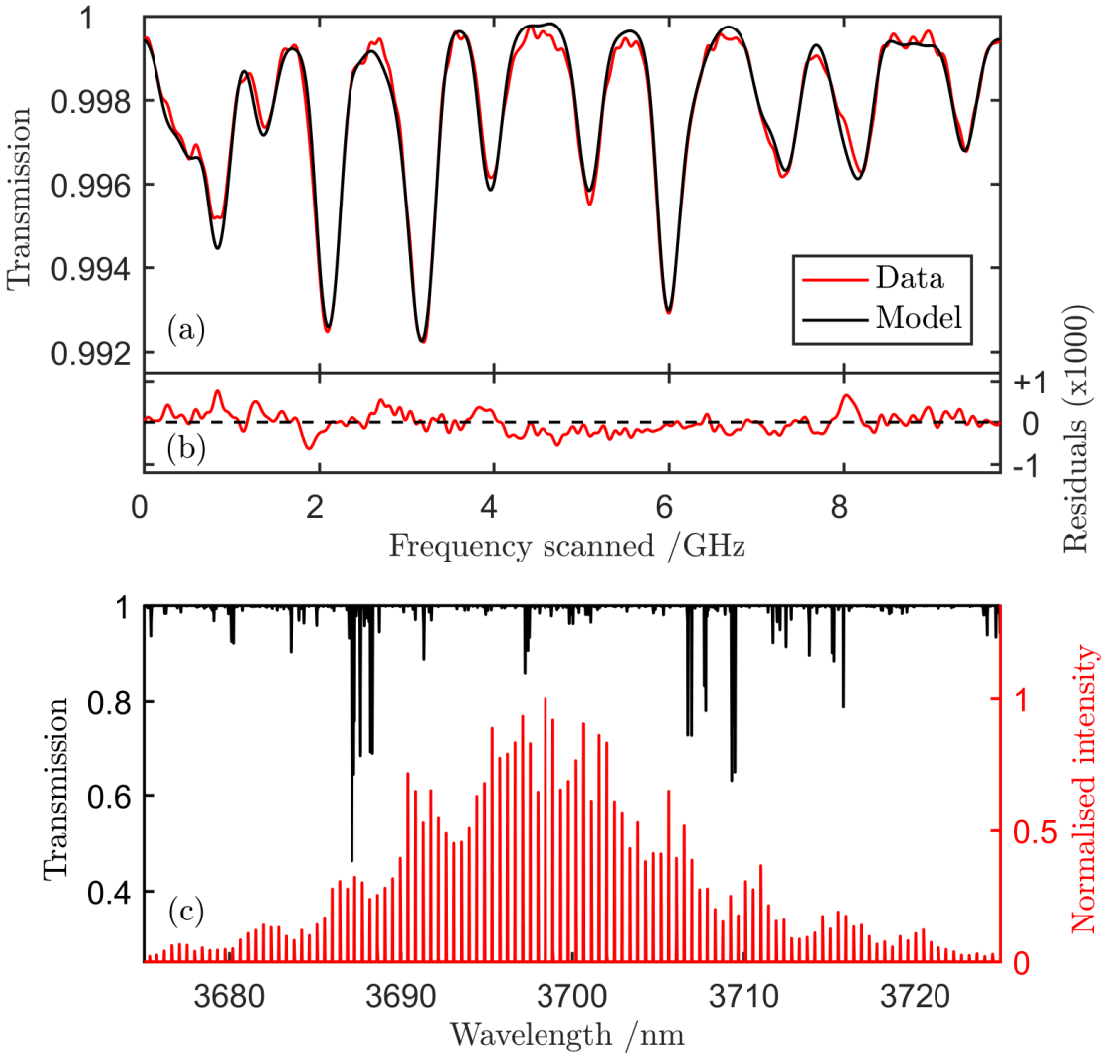

Figure 4.7: Panel (a) shows a MUMAS spectrum of CH_4 in the region of 3.7 µm. The experimental data which is an average of 94 scans at 10 Hz is shown as a red line, and the modelled fit is shown as a black line. Panel (b) shows the residuals between data and fit. Panel (c) shows a reconstructed CH_4 absorption spectrum of lines contributing to the MUMAS spectrum (black lines) and a simulation of the ICL's mode spectrum, containing over 65 modes under the experimentally determined envelope over a range of 30 nm (red lines).

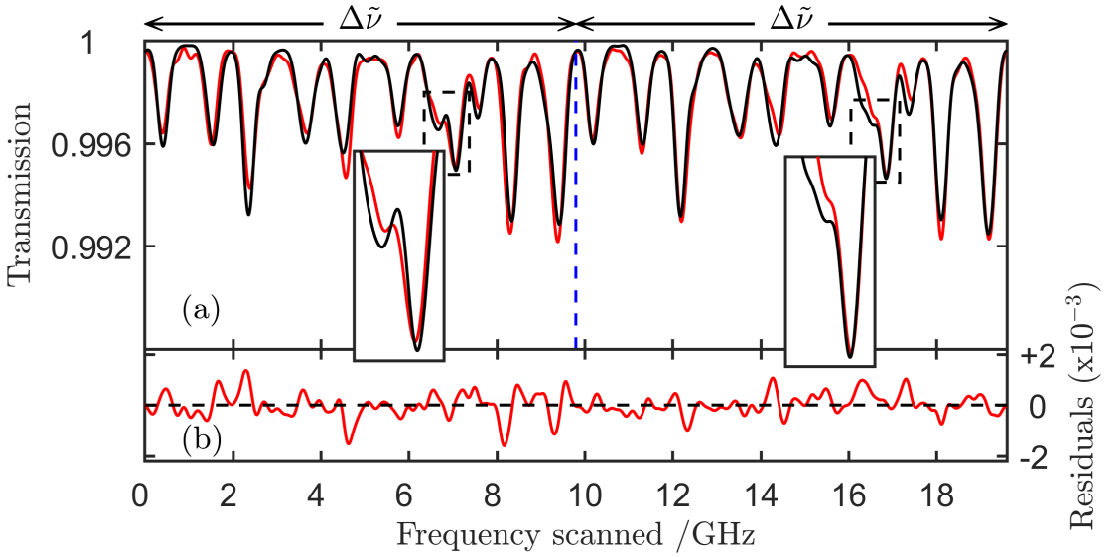

Figure 4.8: Panel (a) shows the experimental MUMAS spectrum (red line) of methane at 2.21 mbar covering two pseudo-repeat-units, which are separated by a blue dashed line, and the modelled fit to the data (black line). The residuals of this fit are shown in panel (b). The insets highlight the main profile difference between consecutive pseudo-repeat-units and the modelled spectra illustrate how this phenomenon is accurately modelled using the expansion-model. The length of each pseudo-repeat-unit, $\Delta\tilde{\nu}$, is represented by the arrows above the spectrum.

that by using an ICL with an intermode-spacing of $\sim$ 75 GHz, a distinctive spectrum can be obtained at atmospheric pressure, therefore showing that with a suitably chosen ICL, species with dense spectra can be detected at high pressure.

4.5.3 Fitting sequential pseudo-repeat-units

As was described in chapter 3, the work in this thesis involves the development a new model, the expansion-model, to more accurately describe the scanning of modes during the operation of MUMAS. This replaces the translation-model which was used in all previous work. As was described in section 3.3, the expansion-model results in the position of the MUMAS absorption features shifting slightly between consecutive scans of one intermode-spacing, and therefore consecutive segments of the MUMAS spectrum of

length equal to one intermode-spacing are not exactly identical repetitions. However, the overall profile of the MUMAS spectrum for consecutive scans of one intermode-spacing is approximately similar, and therefore each of these scans of one intermode-spacing is defined as a pseudo-repeat-unit, $\Delta\tilde{\nu}$. The work in this section demonstrates this phenomenon.

The experimental MUMAS spectrum of two pseudo-repeat-units of methane is shown in figure 4.8 as a red line. The modelled fit to these two pseudo-repeat-units is shown as a black line. The length of each consecutive pseudo-repeat-unit, $\Delta\tilde{\nu}$, is represented by the arrows above the spectrum. The CH_4 partial pressure is determined to be 2.14 ± 0.16 mbar, which agrees within experimental uncertainty with the value of 2.17 ± 0.13 mbar measured using the capacitance manometer. It is clear from the insets that at $\sim$ 6.8 GHz, two absorption features are clearly discernible, whereas at $\sim$ 16.6 GHz, these features merge into what appears to be a single absorption feature. The expansion-model is able to accurately model this appreciable change in the profile of the MUMAS spectrum at $\sim$ 6.8 GHz and $\sim$ 16.6 GHz, and is also able to accurately model some slight changes between the exact spectral positions of the MUMAS absorption features between sequential pseudo-repeat-units. This would be impossible with the translation-model as it would generate identical repeat-units.

A purported drawback of MUMAS is that sometimes it is possible for two absorptions from different molecular transitions to coincidentally occur at the same location in a MUMAS spectrum. One way in which this ambiguity can be removed is by using a laser with a slightly different intermode-spacing. Alternatively, due to the varying position of absorption features in a MUMAS spectrum between sequential pseudo-repeat-units, this ambiguity can instead be easily removed by scanning across multiple pseudo-repeat-units and consequently separating overlapping absorption features.

4.5.4 Enhanced spectral coverage with a single device

In section 4.5.2, it was shown that it is possible to detect transitions of methane spanning a range of ~ 1 THz using a single ICL at particular operating conditions. By varying the operating conditions of the laser and the angle of incidence of the interference filter, it is possible to further extend the spectral coverage of this single device to ~ 3 THz.

The central wavelength of the ICL emission can be varied by a combination of temperature and injection current settings over a range from 3620 to 3770 nm. As explained previously, the bandwidth of the output is narrowed using an interference filter, and the centre of the band pass is adjusted by varying the angle of incidence of the filter. Thus, by a combination of current/temperature tuning and adjustment of the interference filter, different spectral envelopes can be selected. Figure 4.9a shows three such envelopes within the wavelength range $3630 - 3760$ nm. The spectral location and intensity envelopes are measured using the Bristol Instruments Michelson interferometer. The upper trace in figure 4.9a shows the conventional methane absorption spectrum in this range, derived from the HITRAN database [103].

Having selected the spectral range to be probed, the mode spectrum is scanned over one intermode-spacing to record the MUMAS spectrum. MUMAS spectra of methane are recorded for each of the three spectral regions indicated in figure 4.9a. Figure 4.9b shows the resulting MUMAS spectra, together with modelled spectra fitted to the data, and the residuals of these fits. These data show that MUMAS spectra for methane can be recorded across the spectral range covered by the broad bandwidth available from the ICL. All the spectra are recorded at approximately 5 mbar of CH_4.

The intermode-spacing varies between each of these spectral recordings as a result of changes in the ICL's refractive index and temperature-dependent cavity length at different operating currents and temperatures. The precise values of the intermode-spacing are

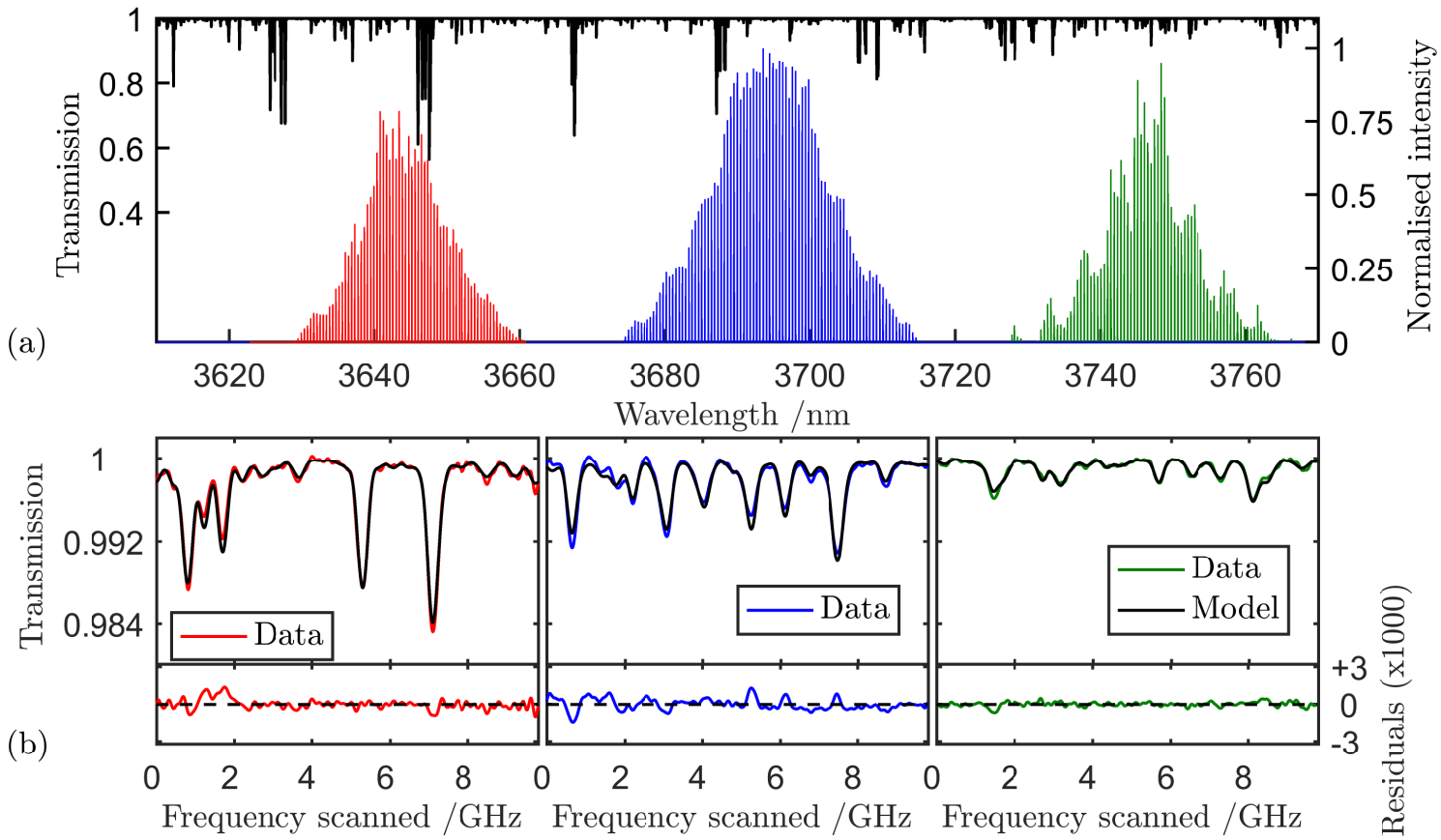

Figure 4.9: Panel (a) shows three different mode envelopes centred at 3645 nm, 3695 nm and 3750 nm, obtained by adjusting the laser drive parameters and interference filter band pass. Individual modes are shown schematically under the experimentally determined envelope. Panel (b) shows MUMAS spectra of CH_4 recorded at each of the three spectral locations shown in panel (a). The red, blue and green lines are experimental data, whilst the black lines are modelled MUMAS spectra.

determined by using this as a fitting parameter to MUMAS spectra obtained under known conditions of concentration, pressure and temperature. Using the spectral location of each absorption feature that is accurately and precisely known from the database, values of the intermode-spacing are found to be 9.803 ± 0.003, 9.785 ± 0.001 and 9.771 ± 0.001 GHz for each of the three spectral envelopes shown in figure 4.9a. The uncertainty value is based on the range giving 5% deviation from the minimum of the χ^2 in the fitting procedure.

It is worth noting the high precision attainable for intermode-spacing measurements using MUMAS. This is a result of measuring over a frequency range covering many multiples of the intermode-spacing, and reference to many frequency markers provided by the spectral database. Although not identical, it is similar to a vernier scale, whereby the precision of a measurement is improved by considering fractional divisions between the major markers of a measurement scale. The high precision is obtained by considering the positions of MUMAS features originating from a single interacting mode, whose separations in absolute frequency are accurately and precisely known, and comparing their relative positions in a MUMAS spectrum to MUMAS absorption features arising from other interacting modes, as a fraction of the intermode-spacing.

Ultimately, the data shown in figure 4.9 further illustrate the potential for using a single ICL device for multi-species detection. It is simply necessary to tune to a selected part of the absorption spectrum of the target species and to define a band of sufficient spectral width that contains absorption lines of each of these molecules.

4.5.5 Species concentration measurements

As was demonstrated in section 4.5.2, it is possible to use MUMAS to obtain a characteristic spectrum of a particular species, and hence identify that species. In addition, it is also possible to use MUMAS to measure the concentration, or partial pressure, of a species.

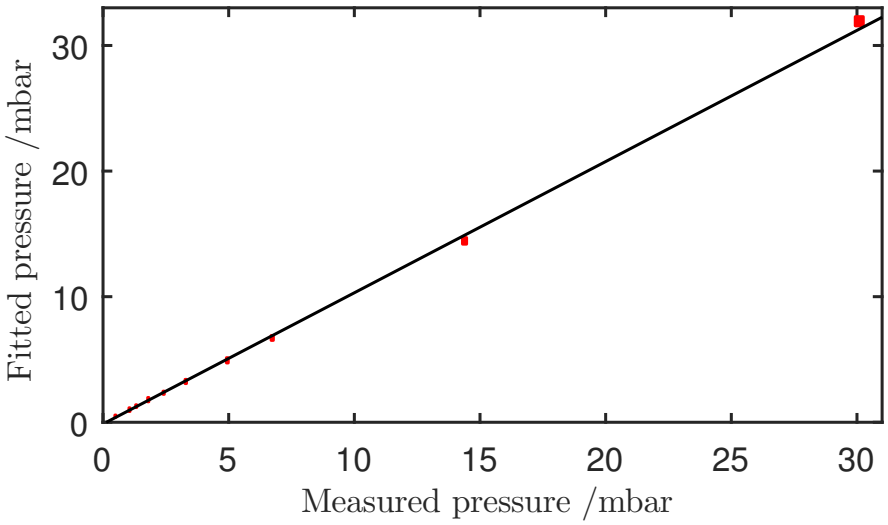

Figure 4.10: Concentration of CH_4 derived from fits to MUMAS spectra versus values measured by a capacitance manometer. The line-of-best-fit has a gradient of 1.04. The errors are indicated by the size of the plotted data points. The uncertainties in the measured pressures are derived from the uncertainty in the reading from the capacitance manometer, and the uncertainties in the fitted pressures are derived from the range of values corresponding to a $\pm 5\%$ deviation in χ^2 from the best-fit value.

Having determined the value of the intermode-spacing of an ICL, data obtained under unknown concentration conditions can be analysed using concentration as the fitting variable. In this way, the partial pressure of the species can be determined quantitatively and compared with measurements using the capacitance manometer. A typical data set for methane pressures derived from fits to the MUMAS spectra is compared with manometer values in figure 4.10. In the case presented here, the MUMAS data provide a linear relationship to the manometer values with a gradient of 1.04 ± 0.011. The uncertainties in the measured pressures are derived from the uncertainty in the reading from the capacitance manometer, and the uncertainties in the fitted pressures are derived from the range of values corresponding to a $\pm 5\%$ deviation in χ^2 from the best-fit value. This plot provides a means of calibrating the MUMAS data so that absolute values of the methane pressure can be derived. The slight deviation from the correct gradient of

1.00, corresponding to a small systematic error, is thought to be due to a small amount of residual air present in the gas handling system of the absorption cell. The uncertainty in the gradient of 1.1% reflects the standard error and represents the precision of the measurements.

Thus MUMAS has been demonstrated to provide an accurate measurement of the concentration of a particular species in a sample.

4.5.6 Multi-species detection

From section 4.5.2 and 4.5.4, it is clear that due to the large spectral coverage achievable with single ICL devices, MUMAS lends itself to detecting multiple species with a single device. In addition to methane, several other hydrocarbons exhibit absorption spectra in the emission wavelength range of the ICL used for the work in this chapter. In particular, both acetylene and formaldehyde have absorption lines with strengths of order 10^{-21} cm^{-1}/(molecule $\times$ cm^{-2}) and 10^{-20} cm^{-1}/(molecule $\times$ cm^{-2}), respectively, compared with those of methane around 10^{-21} cm^{-1}/(molecule $\times$ cm^{-2}) .

Figures 4.11a-c show MUMAS spectra recorded at 3727 nm of samples consisting of pure acetylene, pure methane and pure formaldehyde, respectively, together with fitted modelled spectra. A glass absorption cell of length 0.37 m is used. The acetylene and methane samples are derived from gas bottles (BOC Research grade) of purity 99.995% for methane and 98.5% for acetylene. The formaldehyde is extracted from the vapour above a liquid solution, hence its concentration is more uncertain. The values of partial pressure, i.e. concentration, for each of the pure samples as derived from the MUMAS fits are 3.04 ± 0.16 (2.96 ± 0.04), 1.99 ± 0.12 (1.93 ± 0.06) and 0.0693 ± 0.0052 mbar for methane, acetylene and formaldehyde, respectively. The values in brackets are the partial pressures measured using the capacitance manometer with errors due to the combination of the quoted accuracy of the manometer and the uncertainty in the gas purity quoted by

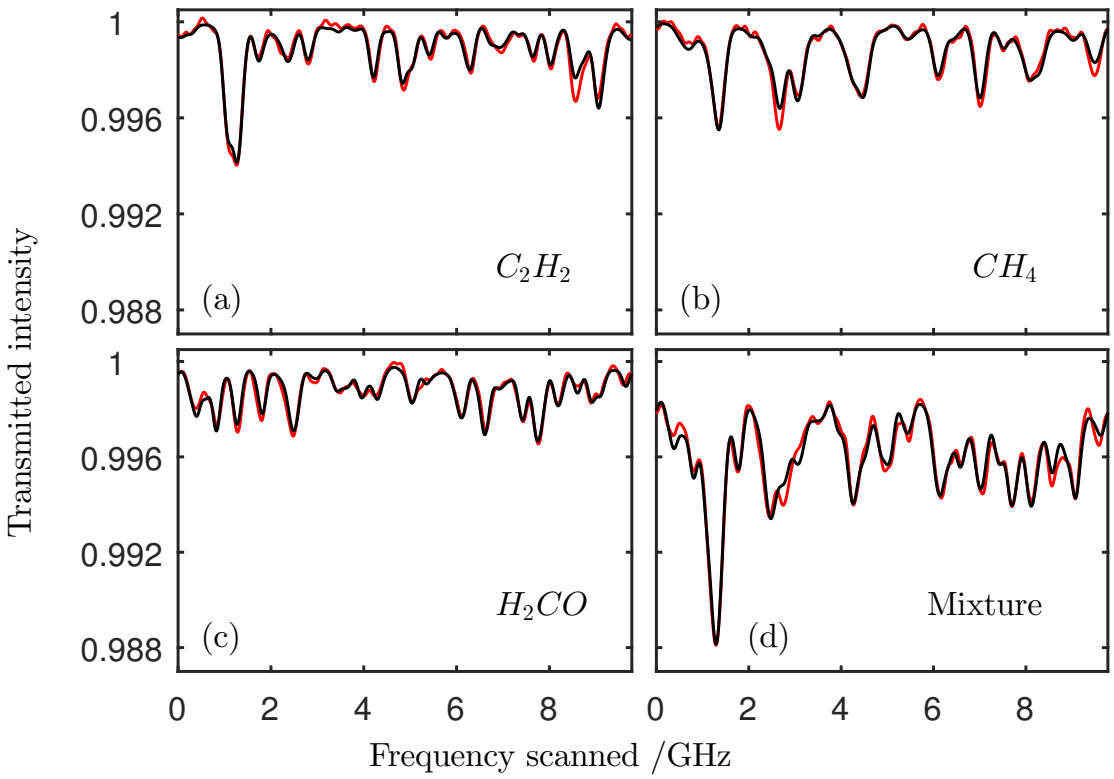

Figure 4.11: MUMAS spectra recorded using a mode envelope centred at 3727 nm and width 27 cm^{-1} of acetylene in panel (a), methane in panel (b) and formaldehyde in panel (c). Panel (d) shows the MUMAS spectrum of a mixture of all three gases from which the individual partial pressures are derived from the model fit. Red lines are the experimental data and black lines are best-fits of the modelled MUMAS spectra using partial pressure as the fitting parameter.

the manufacturer. The precision of the values derived from the MUMAS data is specified, again, as the range defined by a $\pm 5\%$ deviation in χ^2 from the best-fit value. As the formaldehyde is derived from the vapour above an aqueous solution, it is not possible to get an accurate measurement of its partial pressure from the capacitance manometer.

The potential of MUMAS for simultaneous multi-species detection is illustrated by the spectrum shown in figure 4.11d of a mixture containing methane, acetylene and formaldehyde. Concentrations are derived from the fitted model spectrum. All the features in the resulting data are accounted for by transitions in each of the constituent

molecules of the mixture, thus giving unambiguous detection of each species. From the modelled fit, the partial pressures of the methane and acetylene in the mixture are found to be 2.69 ± 0.26 (3.01 ± 0.10) and 1.93 ± 0.16 (2.01 ± 0.11) mbar, respectively, where the values in brackets are the partial pressures measured using the capacitance manometer with errors, again, due to the combination of the quoted accuracy of the manometer and the uncertainty in the gas purity quoted by the manufacturer. The partial pressure of formaldehyde (derived from the vapour above an aqueous solution) determined from the fitting procedure is 0.0891 ± 0.0094 mbar. The uncertainties of the derived partial pressures are 9.6% for methane, 8.3% for acetylene and 10.5% for formaldehyde. These uncertainties are slightly larger than the uncertainties found for the measurements of pure samples of each gas. The relatively large uncertainty in derived concentrations, arising in this case from excessive overlap of lines from different species, could be reduced by probing a different spectral region and with a different intermode-spacing to improve discrimination. In the cases of methane and acetylene, where measured partial pressures are available, the values derived from the MUMAS data are within experimental error of the values measured using the manometer.

It is worth noting that the, somewhat arbitrary, choice of 5% deviation in χ^2 for the fitting to experimental data is justified in the sense that it brings the uncertainty of derived values within experimental error (10%) of the values 'known' from the independent manometer measurements in the cases of acetylene and methane. In the absence of an independent measurement of the formaldehyde partial pressure, it is not possible to validate the accuracy of the formaldehyde measurement using the present data. However, since the partial pressures in the mixture are adjusted to give similar absorption signal amplitudes in the resulting MUMAS spectrum, it seems reasonable to ascribe similar experimental uncertainties to the measurements of each individual component of the mixture in this case.

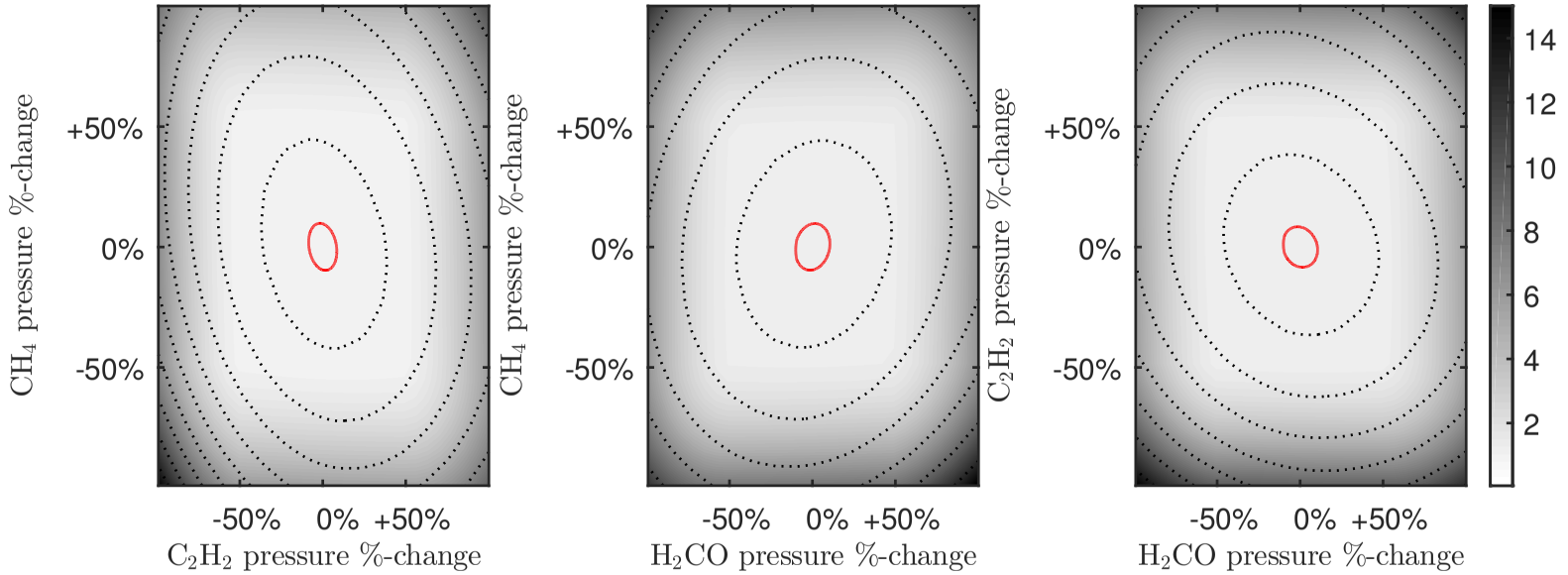

Figure 4.12: Sections through the error-surface around the single global minimum in the 3-dimensional space of the partial pressures of the three gases in the mixture. The error-surface is constructed from values of χ^2 derived from model fits to experimental data. Panels a-c show the variation of χ^2 arising from variation of partial pressures whilst that of H_2CO, C_2H_2 and CH_4, respectively, are held constant at the best-fit value. The uncertainties are defined by the 1.05 contour indicated as a red line. The dotted contour lines are to aid with the illustration of the error-surface. The legend indicates the multiplicative-deviations of the least-squares values from the best-fit value.

As the MUMAS spectra for the individual gases indicate, in this spectral region the spectral features from more than one species may overlap in some portions of the scan, thus leading to potential ambiguity in the proportions of each species present. The analysis of the data uses fitting of modelled MUMAS spectra to the data including the noise from all sources. The model has been validated both by the data of figure 4.7 and figures 4.11a-c, and by other multi-species measurements in previous work [5–7]. The statistical errors derived from the least squares fitting procedure assume the same variance on each distribution of the individual proportions in the mixture, i.e. the individual partial pressures. This is a reasonable assumption, given that the data on all the gases are acquired using the same laser and hence the same intensity distribution of the modes and common values of parameters determining spectral line broadening, etc. This assumption is validated in the present work by finding that the residuals of fits to each spectral scan and on derived partial pressures show a normal distribution with similar values for the coefficient-of-variation of around 5×10^{-2}. Hence, by using an exhaustive search approach to finding the global minimum, in the parameter space of the three partial pressures, it is possible to find errors on the individual partial pressures. Unambiguous values of the partial pressures are therefore derived, within the stated uncertainties given above. This is illustrated in figure 4.12 which shows sections through the 3-dimensional error-surface centred on the global minimum found by the least-squares fitting procedure. This surface is constructed by plotting the value of the normalised χ^2 representing the goodness-of-fit to the data and its associated noise, where the normalisation sets the χ^2 of the best-fit value to 1.0. The experimental error, defined as stated above as the range of values within which χ^2 is less than 5%, is represented on the figures by the contour with value 1.05 (solid red line). The results shown in figure 4.12 clearly indicate no other local minima in the fits. Therefore, it is shown that the spectra for each species are orthogonal and there is no ambiguity in the derived proportion of each species.

4.5.7 Minimum Detection Limit (MDL)

The primary aim of MUMAS is the simultaneous detection of multiple species using a single laser and a single detector system. In particular, the results in section 4.5.6 have demonstrated the potential of ICLs for multi-species detection in the mid-infrared using MUMAS. Nonetheless, it is also important to determine the Minimum Detection Limit (MDL) for a particular species or combination of species. Moreover, sensing applications, particularly those for process control, often involve a compromise between measurement time and detection sensitivity, or MDL, and this is considered when analysing the Allan variance measurements below.

It is difficult to assign an absolute value for the MDL since it will depend on many independent factors. The MDL for a given species depends on several species-dependent factors including the line-strengths, spectral structure (i.e. degree of spectral congestion) and whether other species are present as background absorbers. However, of equal significance for determining the MDL of a particular species will be the specific characteristics of the laser mode structure. MUMAS spectra consist of the measured decrease in total transmitted intensity of all the modes present as individual modes are absorbed by specific molecular absorption transitions. With each mode making up a portion of the total transmitted intensity of a multi-mode laser, then clearly, the maximum sensitivity and lowest MDL value will occur when only a single laser mode is used, as in TDLAS. On the other hand, as the number of modes increase, the effect on total transmitted intensity of only one of those being absorbed by a molecular transition will tend to zero. This inevitably presents a trade-off between reducing the MDL and enhancing the multi-species capability, since the bandwidth and number of modes employed affect the dynamic range of the spectral absorption features in a MUMAS spectrum.

The number of modes itself, however, is not the only important factor of the laser spectrum since the overall spectral width of the multi-mode envelope and the intermode-spacing are also critical in spectrally discriminating the contributing absorption features. This ability to distinguish different contributions also strongly influences the species selectivity, detection sensitivity and MDL. A narrow intermode-spacing and higher number of modes will tend to produce more blended spectral features as more transitions are detected within a given scan. Blending of the spectral features will be exacerbated by pressure broadening of the features, which ultimately leads to a featureless MUMAS spectrum at high pressure. In practice, the value of the intermode-spacing for typical ICLs lies in the range $10-80$ GHz. The overall bandwidth of the laser spectrum should include transitions from all the target species, and the number of modes will be determined by the intermode-spacing. The value of the intermode-spacing, however, is also limited by the device's ability to provide continuous tuning across the required range without mode-hops or instability. Given these factors, a compromise must be found which provides sufficient spectral coverage to capture each of the target species, yet with as few modes as possible to provide adequate dynamic range, whilst also being consistent with the device's MHF tuning capability. Ultimately, the SNR is the limiting factor, and this will depend upon the degree of averaging used and the time taken to acquire the data. In the work which has been presented thus far, the value of the key parameter, the intermode-spacing, has been pre-determined by the physical parameters of the device which is available. As the range of choices improves, however, the choice of intermode-spacing of the laser will become important.

In order to obtain an indication of the MDL and potential for SNR improvement for the available device and a given measurement time, the Allan variance of the derived concentration, using a sample of 2.61 mbar of methane, is determined for a particular setting of the ICL. That is, a particular set of absorption lines is probed by a laser with

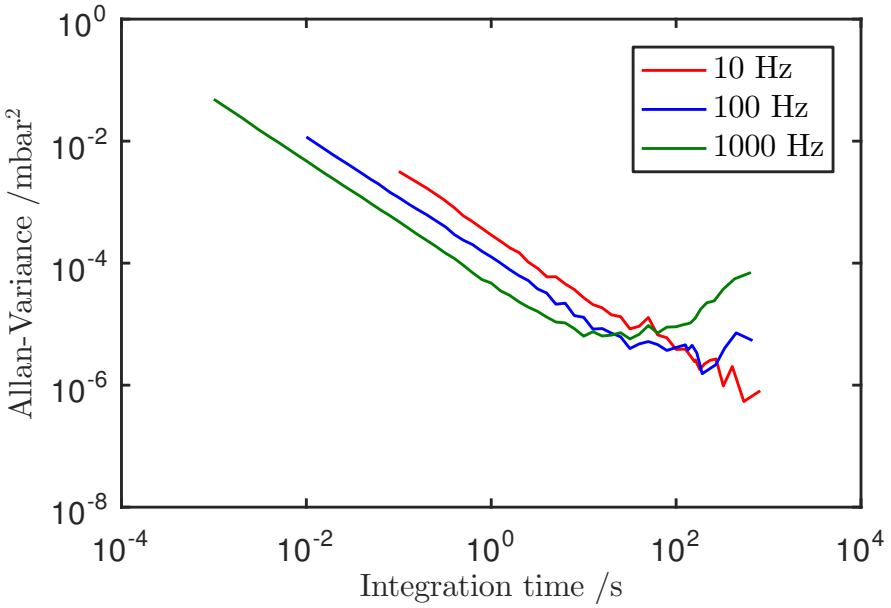

Figure 4.13: Allan variance plots for derived CH_4 concentrations from MUMAS spectra at 3.68 µm at scan rates of 10 Hz, 100 Hz and 1000 Hz, shown as red, blue and green lines, respectively.

a specific mode structure. Using a bandwidth centred at 3.68 µm and envelope width of 33 nm, which corresponds to approximately 75 modes with an intermode-spacing of $\sim$ 10 GHz, the Allan variance of the derived pressure of methane is determined for a range of scan rates between 10 Hz and 1 kHz. The strongest lines in this region of the methane spectrum have a strength of 9.81×10^{-22} cm^{-1}/(molecule $\times$ cm^{-2}). The spectra obtained at these fast scan rates demonstrate the potential for rapid monitoring with MUMAS. The maximum scan rate is limited by the bandwidth of the data acquisition system to about 1 kHz, although the ICL is capable of scanning at a much higher rate. From the data shown in figure 4.13, it can be seen that under these operating conditions and timescales the variance trends downward for up to approximately 15 minutes of recording time at the lower scan rates of 10 Hz and 100 Hz. However, the variance begins to increase at a scan rate of 1 kHz for measuring times above $\sim$ 1 minute. These data seem to indicate that at higher scan rates the ICL's output characteristics experience a

relatively slow drift. Since the effect does not appear until the averaging time exceeds ~ 10 s, it may not present a serious issue because process control applications usually demand response times of < 1 s.

Since applications in process control usually require a reasonably short measurement time, the present data indicate that increasing the scan rate above 1 kHz would improve the detection limit for measurement times of order 1 s. As noted above, the present work is restricted to scan rates of < 1 kHz owing to the limited bandwidth of the available data acquisition hardware. Using a scan rate of 100 Hz, the minimum pressure of methane in a pure sample that could be detected with a SNR of one for a 1 s measurement time is 0.18 mbar in the single-pass absorption cell of length 0.37 m. This figure indicates the minimum pressure required to detect a pure sample of this species in this path length. Whilst the trace detection levels of a species in a background gas are usually specified in ppmv at atmospheric pressure, with the device used here having an intermode-spacing of ~ 10 GHz, the MUMAS spectrum of CH_4 in 1 bar of total pressure would be essentially featureless. Therefore this particular ICL, although being able to detect multiple species, would not be suitable for performing highly sensitive detection.

As discussed in section 3.5, an effective way of avoiding a congested MUMAS spectrum, and subsequent featureless spectrum when pressure broadened, is to use a multi-mode laser with a wider intermode-spacing. Before being tested experimentally, simulations are performed to determine whether ICLs with a wider intermode-spacing would be able to perform highly sensitive measurements. In these simulations, the only laser parameter which is changed from those used in this section is the intermode-spacing – it is increased to 80 GHz. The simulated MUMAS spectra are shown in figure 4.14. Using such a device and assuming similar noise levels as obtained in the work in this section, the wide intermode-spacing provides sufficient spectral structure to allow identification of methane at 1 bar pressure of air, and a MDL of order 100 ppmv is estimated for a

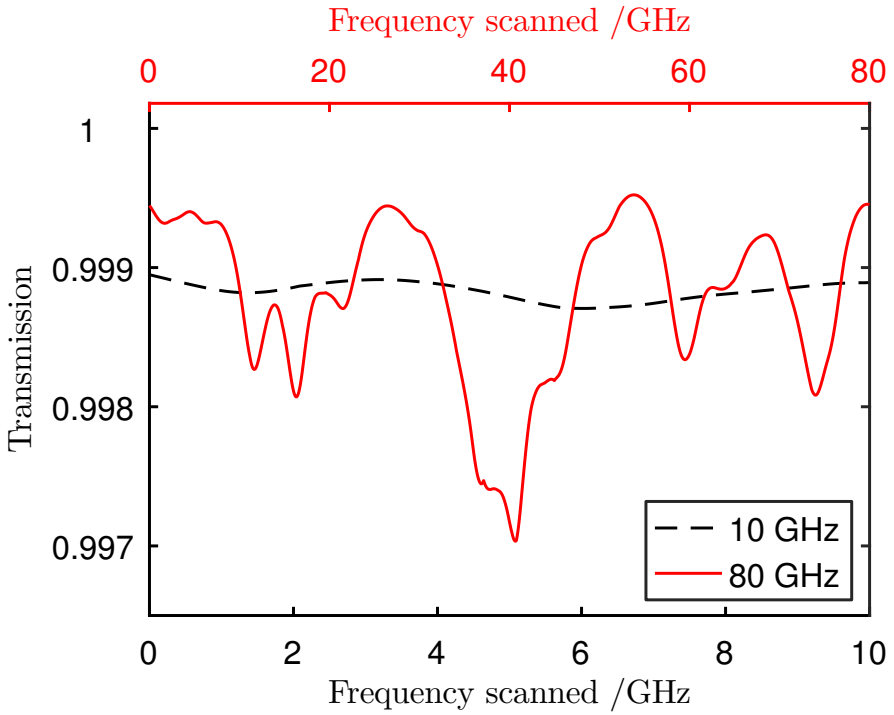

Figure 4.14: Modelled MUMAS spectrum of CH_4 (1000 ppm) in air at 1 bar for a laser with an intermode-spacing of 10 GHz (dashed black line) or 80 GHz (solid red line). Unique features for species identification are apparent only when using the laser with a wide intermode-spacing.

measurement time of 1 s at 100 Hz scan rate. Detection of CH_4 at typical atmospheric concentrations of 1.7 ppm would require significant improvement to the MDL but not for other applications such as process control where concentrations may be significantly higher [118]. This limit could be improved to allow detection of atmospheric methane by using an ICL emitting in the range $3.2 - 3.4$ µm, where the methane transitions are significantly stronger, and use of SNR enhancement strategies such as WMS or cavity enhancement, both of which have been demonstrated with MUMAS [4]. However, when comparing the MDLs of TDLAS and MUMAS it is worth noting that, although the former provides a lower MDL, a MUMAS spectrum gives additional information such as on populations of other quantum states – from which temperature can be derived, or the

presence of interfering species. MUMAS achieves detection limits adequate for a range of sensing applications with its advantage being its multi-species capability rather than ultimate sensitivity.

4.5.8 Atmospheric pressure sensing

In all previous work on MUMAS, pure samples of the target species were probed. The intermode-spacing of the multi-mode laser sources used for all previous MUMAS work in the mid-infrared region have typically been small (< 20 GHz). As was discussed in section 3.5 and simulated in figure 4.14, the high spectral congestion in a MUMAS spectrum renders it featureless when the target species are broadened by atmospheric pressure. This has limited MUMAS to the detection of pure samples, rather than trace amounts in atmospheric pressure. An effective method of enabling trace detection in atmospheric pressure is to use a multi-mode source with a wider intermode-spacing. In this way, the spectral density of features in the MUMAS spectrum would be less and once broadened by atmospheric pressure, the resulting MUMAS spectrum would have unique features for species identification.

The work described in this section uses a second ICL provided by NRL, which is centred at 3.27 µm. The cavity length of ~ 0.5 mm is approximately 8 times shorter than the initial batch of ICLs, and hence provides an intermode-spacing 8 times larger (~ 75 GHz). The measurement of the intermode-spacing is refined by fitting an experimental MUMAS spectrum obtained from a calibrated sample, and using the intermode-spacing as one of the fitting parameters. It is found to be 75.960 ± 0.013 GHz. Again, the uncertainty value is based on the range giving 5% deviation from the minimum of the χ^2 in the fitting procedure.

The MUMAS spectrum of CH_4 obtained using this laser is shown in figure 4.7a (red line) along with the fitted MUMAS spectrum (black line). The modelled spectrum agrees

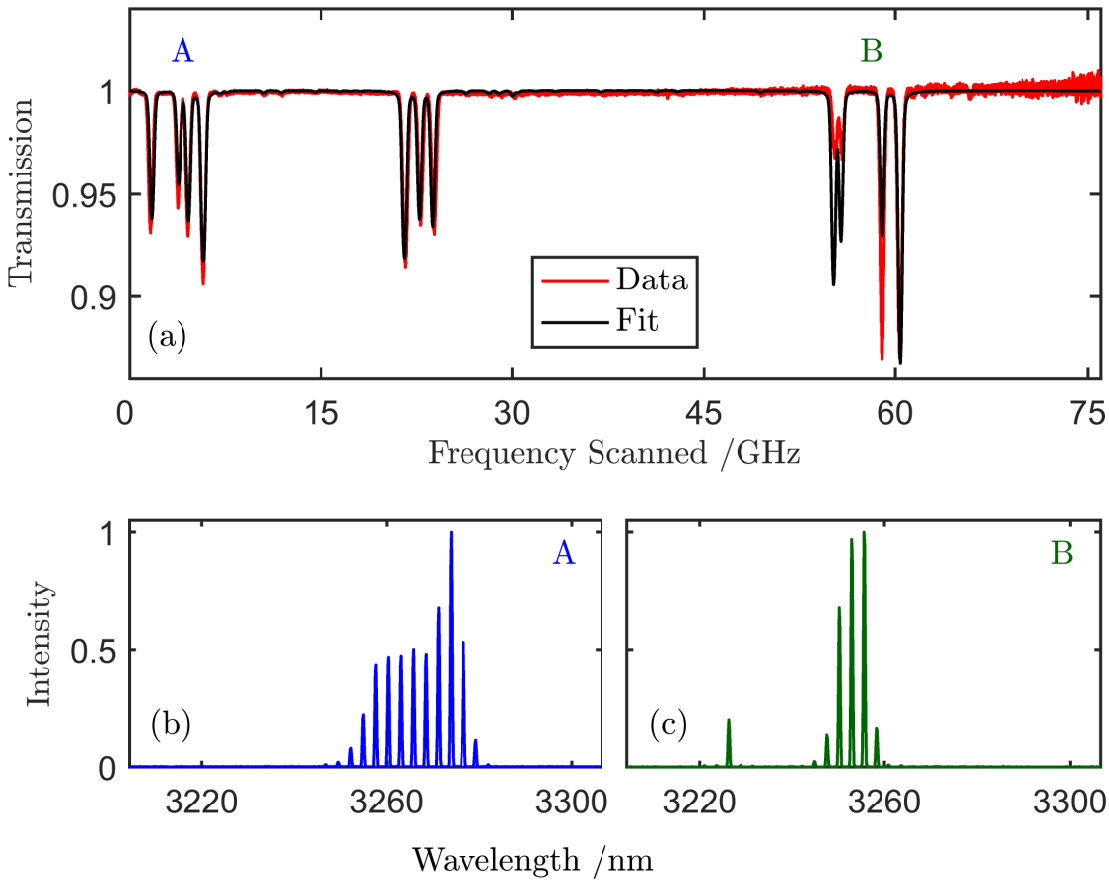

Figure 4.15: Panel (a) shows a MUMAS spectrum of CH_4 using an ICL with a wide intermode-spacing. The experimental spectrum is shown in red and the modelled fit is shown in black. Panel (b) and (c) show laser spectra taken at points 'A' and 'B' along the scan, correspondingly labelled in panel (a).

well with the experimental data between 0 GHz and 45 GHz, whereas the height of the absorption features beyond this region appear to be poorly modelled. The reason for this poor agreement is due to the laser spectrum not being accurately represented by a fixed intensity envelope for the entirety of the scan.

The laser spectra in figure 4.15b ('A') and 4.15c ('B') are measurements of the laser spectra at the corresponding positions, 'A' and 'B', along the scan in figure 4.15a. It is clear that, with this particular device, the laser spectra change appreciably during the scan. In general, there are of order 10 modes in the laser spectrum and it covers

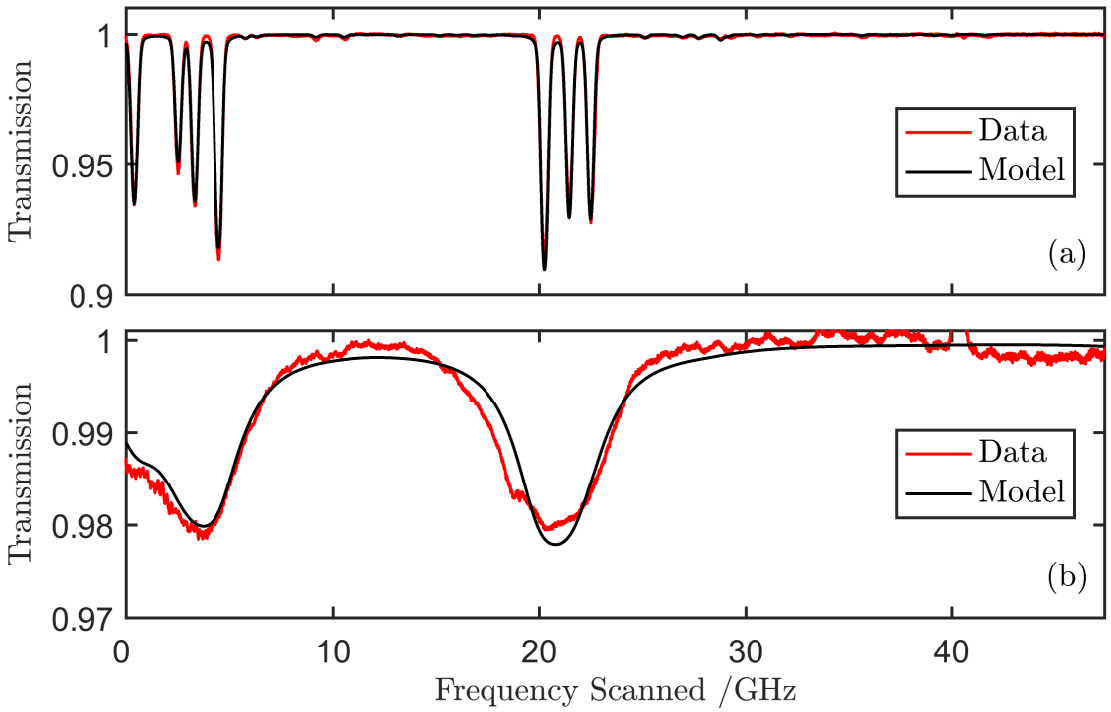

Figure 4.16: Panel (a) shows the 0 GHz to 45 GHz region of the MUMAS spectrum of figure 4.7a. Panel (b) shows the MUMAS spectrum of the same sample of methane, but broadened by 1 atm of N_2. In both panel (a) and (b), the experimental MUMAS spectrum is shown as a red line and the modelled MUMAS spectrum is shown as a black line.

a spectral range of $\sim$ 40 nm. It is found that between 0 GHz and 45 GHz on the MUMAS spectrum, the laser spectrum is approximately constant and is given by the laser spectrum in figure 4.15b. However, the laser spectrum begins to vary appreciably beyond 45 GHz. This is also apparent in the quality of the fit in figure 4.15a. The height of the absorption features appear to be modelled accurately between 0 GHz and 45 GHz, where the envelope of the laser spectrum is constant. However, beyond this region, the height of the absorption features are poorly modelled.

In later work, the modelling code is modified in order to be able to incorporate data from a varying laser mode intensity envelope as the modes are scanned (section 6.4). However, for the present work, only the spectrum between 0 GHz and 45 GHz is considered

for analysis, as the laser spectrum for this region is known to be constant.

Figure 4.16a is the 0 GHz to 45 GHz region of the MUMAS spectrum of figure 4.7a. Again, it is clear that the model (black line) agrees well with the data (red line) as all the features are accurately modelled. Using the partial pressure as a fitting parameter, the CH_4 partial pressure is determined to be 117 ± 4 µbar, which agrees within experimental uncertainty with the value of 114 ± 2 µbar measured using the capacitance manometer. Given the wide intermode-spacing, there is less spectral congestion of MUMAS features than was present in spectra recorded with earlier lasers. Furthermore, there is also a zero-absorption baseline for the majority of the spectrum. The spectrum in figure 4.16b is a MUMAS spectrum with the same quantity of methane as in figure 4.16a, but broadened by 1 atm of N_2. Rather than being featureless, a distinctive MUMAS spectrum results, with the two broad features at ~ 5 GHz and ~ 20 GHz being characteristic of methane. They are comprised of the two bunches of features in figure 4.16a. Therefore, with a suitably chosen ICL, species with dense spectra can be detected when broadened by high pressure.

This is the first demonstration of MUMAS for species detection at atmospheric pressure. Further development and availability of multi-mode lasers with wide intermode-spacing will open up the possibility of highly sensitive, multi-species detection of trace species in high buffer pressures.

4.6 Current limitations of ICLs for MUMAS

This chapter demonstrated the potential for using ICLs to detect multiple species using MUMAS. However, during the work, a few limitations of the technique were identified.

Currently, the main limitation is the restricted availability of ICLs. Until recently, these devices were only available from the group who developed them, the Naval Research

Laboratory. However, ICLs have begun to become commercially available (from both Thorlabs and Nanoplus). Being novel devices, they are still expensive when purchased individually. However, with large quantities of identical devices being made in a single batch process, the cost of multiple devices will only be marginally more expensive than a single device, thus reducing the unit cost. Continued development of ICLs will make them more robust and less expensive, thus increasing their potential for use in a portable MUMAS device.

The primary aim of MUMAS is the simultaneous detection of multiple species using a single laser and a single detector system. However, this limits the ultimate sensitivity of the technique. As was discussed in section 4.5.7, with each mode constituting a fraction of the total transmitted intensity of a multi-mode laser, the maximum sensitivity and lowest MDL will occur when only a single laser mode is used, as in TDLAS. However, reducing the number of modes effectively reduces the spectral coverage of the device, thus presenting a trade-off between enhancing the MDL and reducing the multi-species capability. Despite this trade-off, MUMAS achieves detection limits adequate for a range of sensing applications and its advantage is its multi-species capability rather than ultimate sensitivity.

An enduring limitation of MUMAS is the poor dynamic range of the detection scheme. As each mode contains only a portion of the total transmitted intensity of the light, the observed signals as a reduction in the total transmission are subsequently small. When recording the transmitted intensity, these small absorption signals will appear on a large DC offset. Therefore the majority of the measured transmission provides no information, hence resulting in poor dynamic range. This has further consequences on the data acquisition equipment since the large vertical resolution which is necessary is mostly used on the large DC offset of the signal.

An alternative detection scheme has been designed to solve the problem of this poor

dynamic range [119]. The solution is to use a balanced ratiometric detection scheme which divides the transmission signal by the reference signal in circuitry. The logarithm of this analogue ratio, modulo one, is given as the output of the device. The dynamic range is consequently significantly improved (section 6.3.1). In addition, the effect of the majority of the noise sources are mitigated using this detection scheme. Such a balanced ratiometric detection scheme is employed in the work in the near-infrared region described in chapter 6. However, at present, there are no such detection schemes available for use in the mid-infrared region.

4.7 Conclusion

This chapter has demonstrated the first mid-infrared MUMAS spectrum obtained using an ICL. A MUMAS spectrum of 2.89 ± 0.01 mbar of methane was obtained with an ICL that has a spectral bandwidth of 30 nm.

The ICLs used in this work were provided by the Naval Research Laboratory. These devices are physically small and have low power requirements, thus making them suitable for gas sensing applications in the field.

To acquire MUMAS spectra with these ICLs, a standard direct absorption spectroscopic technique was employed. A new method was used for linearising the frequency scale of the MUMAS spectrum. A fitting routine was developed to fit a modelled MUMAS spectrum, which was derived using the new expansion-model, to the experimental data, and hence allowed analysis of the MUMAS spectrum. This fitting routine enabled the parameters of the multi-mode laser to be determined to a high level of accuracy and precision. The fitting routine was ultimately used for identification and quantification of the sample species.

The new analytical procedure for determining the individual mode-linewidths of

the laser was presented, and the Lorentzian linewidth of the laser modes was found to vary with injection current from 10 to 80 MHz. In addition, by varying the operating conditions of the laser, the spectral coverage of this single device was extended to $\sim$ 3 THz. The broad spectral coverage of the technique was subsequently exploited to demonstrate multi-species detection using a single device. Trace amounts of methane, acetylene and formaldehyde were simultaneously detected using a single device. Individual partial pressures of the three gases were derived from best-fits of modelled MUMAS spectra to the data with an experimental error of 10%. The MDL of the technique was investigated. Using a scan rate of 100 Hz, the minimum pressure of methane in a pure sample that could be detected with a SNR of one for a 1 s measurement time was found to be 0.18 mbar in the single-pass absorption cell of length 0.37 m. It was noted that this was for detection of a pure gas and that these spectra would become featureless when broadened by atmospheric pressure. To alleviate this problem, ICLs with a wide intermode-spacing were used to obtain MUMAS spectra of trace amounts of methane in atmospheric pressure, thus demonstrating the potential for highly sensitive, multi-species detection using a single multi-mode laser source.

The chapter concluded with a brief discussion of the limitations of the technique at this stage in the thesis.

Chapter 5

MUMAS with Quantum Cascade Lasers

5.1 Overview

This chapter documents the use of Quantum Cascade Lasers (QCLs) for MUMAS. The previous chapter, which presented the results of MUMAS using ICLs, highlighted a few of the limitations of the technique (section 4.6). Some of these limitations are addressed in this chapter. In particular, the ICLs used for the work in chapter 4 were not commercially available, whereas the experiments presented in this chapter were conducted using a commercially available multi-mode QCL. Therefore, potential users will not be required to construct custom lasers or use relatively complex DFG systems, thus facilitating the widespread use of MUMAS.

Until the work described in this chapter, the longest wavelength at which MUMAS had been demonstrated was 3.7 µm using an ICL (chapter 4). Extending the spectral coverage of MUMAS provides access to other species with transitions at higher wavelengths. Furthermore, the use of wavelengths in the spectral range $4 - 10$ µm is advantageous

since many important molecular species exhibit strong, well-resolved absorption features in this range. The $4 - 10$ µm has become more accessible in recent years through the use of commercially available QCLs such as those used for the work in this chapter.

This chapter describes the first demonstration of MUMAS using a QCL and the first application of MUMAS to detect NO. In addition, data are obtained clearly distinguishing the presence of H_2O in laboratory air, hence showing the ability of MUMAS to identify a common interfering species. Although the QCLs used in this work have the advantage of being commercially available, the intensity envelope of their laser spectrum is highly irregular and variable. Nonetheless, even with an irregular and spectrally structured multi-mode envelope, which also varies during the spectral scanning, it is shown that all the features of experimentally recorded MUMAS spectra can be modelled with sufficient accuracy to achieve good fits to the data. This demonstrates that commercially available multi-mode lasers can be used for MUMAS in spite of the far from optimal spectral characteristics of their output.

A new technique is developed that shows that the spectral width of the longitudinal modes of the multi-mode output of the QCL can be determined using measurements of pressure broadening of the MUMAS spectra. Finally, MUMAS spectra are obtained at laser scan rates of 10 kHz, thus demonstrating the potential for short measurement times using QCLs for MUMAS.

5.2 Experimental details

The experimental apparatus and procedure used for the work in this chapter is similar to that used for all previous MUMAS work, and is described in detail in section 4.3. A standard optical setup is used to measure the transmission through samples of the target gases using direct absorption spectroscopy. A schematic of this experimental setup using

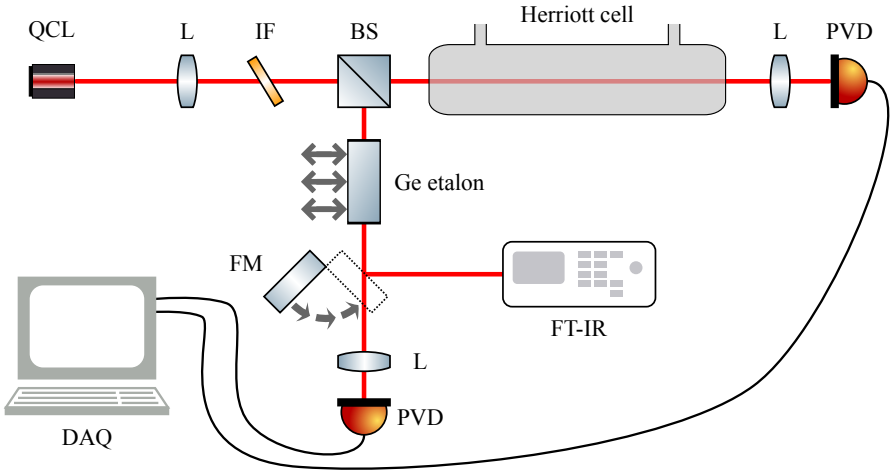

Figure 5.1: Schematic of the experimental layout for MUMAS using QCLs. The spectrum of the output of the QCL is conditioned by the optical (interference) filter prior to being measured by the FTIR instrument. The flip-mirror is removed during the MUMAS experiment in which the beam splitter reflects a small fraction of the beam to a photovoltaic detector to measure the intensity of the reference beam, I_0, and the remainder passes through the multi-pass Herriott cell containing the absorbing gas to the other photovoltaic detector to measure the intensity of the probe beam, I_T. The data acquisition system records the intensities. L: lens, IF: interference filter, BS: beam splitter, FM: flip-mirror, PVD: photovoltaic detector, DAQ: data acquisition.

QCLs is shown in figure 5.1.

For the work in this chapter, the multi-mode laser used is a commercially available Fabry-Perot QCL (Thorlabs QF5300CM1) which provides 80 mW of power at 5.3 µm using a commercial driver (ILX-Lightwave LDX 3232) and a temperature controller which is built in-house. Scanning is effected using a function generator to control the drive current (TTi TG230 2 MHz). The output radiation is passed through an optical interference filter (Spectrogon NB-5360-078 nm) to remove some of the irregular spectral structure, and the spectrum of the resulting output is measured using a Fourier Transform Infrared spectrometer, FTIR (Perkin Elmer Spectrum 100 FTIR). This measurement is made only once as the output spectrum is found to be reproducible. The laser beam is directed to the FTIR by a flip-mirror which is retracted after these measurements

are taken in order to allow the beam to propagate to the absorption cell and detectors. Measurement of the mode-linewidth is described in section 5.4 below. Nitric oxide is admitted into a multi-pass Herriot cell with CaF_2 windows and which has an effective path length of 26 m. Pressure in the cell is monitored using different gauges for low and high pressures (Leybold vacuum CTR90 and 600A-1000T-R12-H21X-X, respectively) with an uncertainty of 0.2% at the lower pressures. For all the partial pressure values presented in this chapter, the uncertainties in the measured pressures are derived from the uncertainties in the readings from the pressure gauges, and the uncertainties in the fitted pressures are derived from the range of values corresponding to a $\pm 5\%$ deviation in χ^2 from the best-fit value. Incident and transmitted laser intensities are measured using separate photodetectors (Vigo Systems, model PVM-2TE-10 and Vigo Systems, model PVI-2TE-6, respectively) and digitally recorded (Handyscope HS4).

5.3 MUMAS spectrum of nitric oxide

Using the experimental setup described in section 5.2, a MUMAS spectrum of NO recorded using a measured pressure of 2.79 ± 0.01 µbar is shown in figure 5.2a as a red solid line. As with all MUMAS spectra, these data represent the effect on the total transmitted power as all the modes are scanned across the intermode-spacing, $\Delta\nu_{\mathrm{mode}}$. In a congested spectrum, such as that of NO (which has a rotational constant of similar magnitude to $\Delta\nu_{\mathrm{mode}}$), absorption of several modes, each by a different NO absorption line can contribute to one of the observed MUMAS features in the transmission. In particular, the large feature at 4.2 GHz is caused by the superposition of MUMAS features from multiple transitions. A modelled fit to the data is shown in figure 5.2a as a black line. All the main MUMAS absorption features are present in the modelled spectrum. In order to find the best-fit to the data the laser parameters need to be determined.

These include the intermode-spacing, the intensity envelope of the laser spectrum and the individual mode-linewidth.

As was described in section 4.4.1, previous MUMAS experiments have used mode envelopes that could be modelled with reasonable accuracy by a simple analytical function. In these cases, the laser provided a smooth and symmetric mode envelope or the output was modified by transmission through an interference filter in order to provide a more regular spectral profile. For the work presented in this chapter, the QCL used is a commercially available device which emits a broadband output with an irregular spectral profile that is not amenable to modelling by a simple analytical function. Some of the spectral intensity variations are removed by passing the laser output through an interference filter. This also serves to narrow the spectral coverage so as to limit the number of transitions probed thus enhancing the relative absorption signals and reducing the number of overlapping transitions recorded. Nonetheless, the resulting spectrum still exhibits significant spectral variation in intensity across the transmitted bandwidth. Consequently, the spectral envelope is measured using the FTIR instrument, for input into the model. The shape of the spectrum, however, is found also to change as the modes are scanned across a single intermode-spacing, $\Delta\nu_{\mathrm{mode}}$. Figure 5.2b shows the FTIR measurement of the envelope at seven locations along the scanned range. For preliminary studies, the intensity envelope is taken to be a constant equal to the average of the spectra measured at these locations and this average function is used to calculate the modelled MUMAS spectrum in figure 5.2a. Errors associated with assuming a constant spectral profile for the envelope will be discussed in section 5.6, below.

In practice, the most critical parameter for accurate modelling is the intermode-spacing, $\Delta\nu_{\mathrm{mode}}$, and, as described in section 4.4.1, it is most accurately determined from fits of modelled MUMAS spectra to MUMAS data of a known species recorded under known conditions of concentration, temperature and pressure. For the QCL used in this

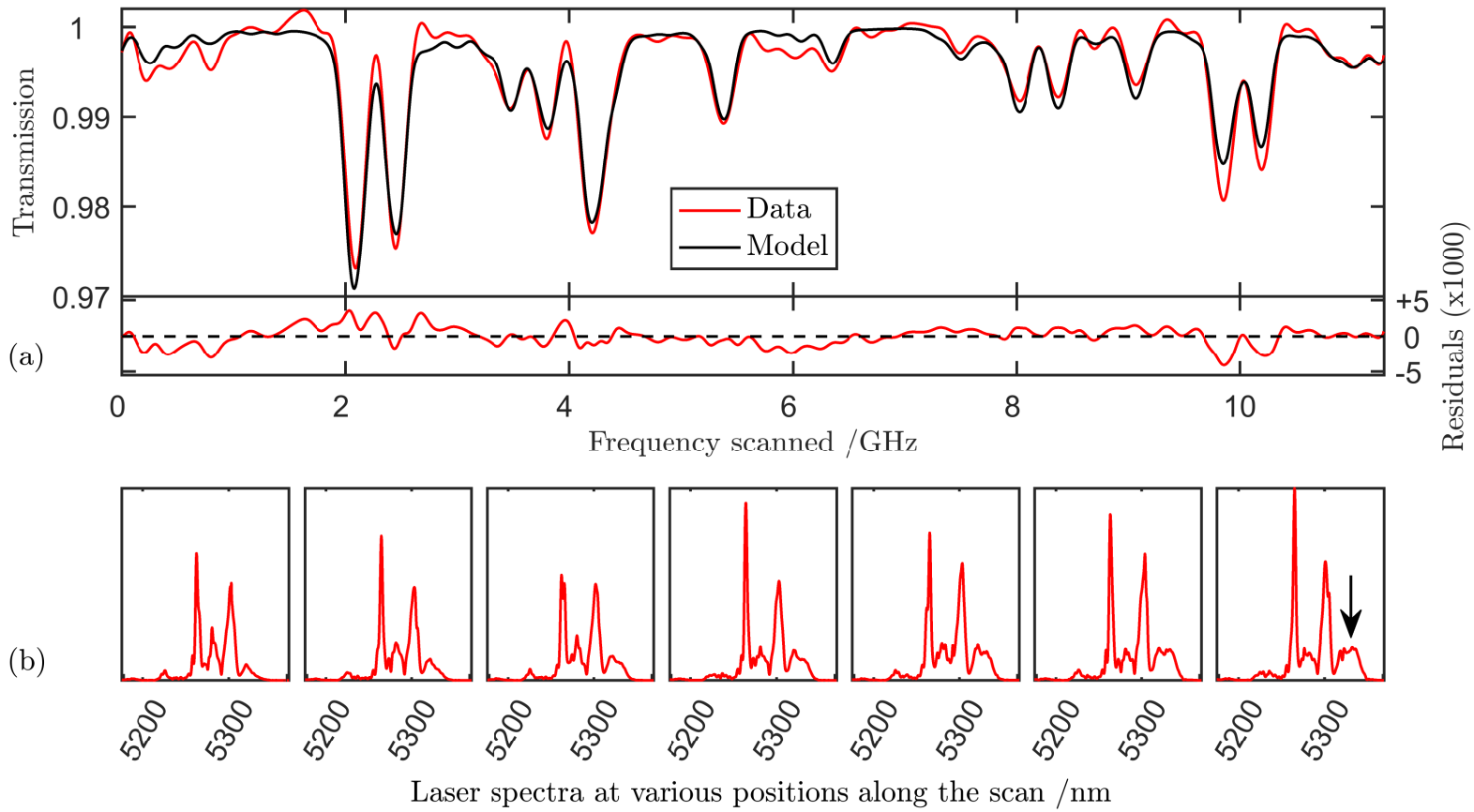

Figure 5.2: Panel (a) shows a MUMAS spectrum of NO (red line) with a fitted model spectrum (black line) assuming a constant mode envelope which is calculated as the average of the laser spectra in panel (b). The lower plot shows the residuals between the data and best-fit model spectrum. Panel (b) shows spectral envelopes measured using the FTIR instrument at different locations in the $\sim$ 11 GHz-wide frequency scan of the modes. Note the change in relative intensity of the narrow peaks in the mode spectrum and the growth of the wide 'lobe' beyond 5300 nm towards the end of the scan indicated by the arrow.

work, the intermode-spacing is determined from fits to MUMAS spectra of NO recorded at a low pressure of 2.79 µbar in order to maximise spectral resolution. In this way, the intermode-spacing is found to be 11.295 ± 0.001 GHz. The uncertainty value is based on the range giving 5% deviation from the minimum of the χ^2 in the fitting procedure.

The NO partial pressure is determined to be 2.74 ± 0.35 µbar, which agrees within experimental uncertainty with the value of 2.79 ± 0.01 µbar measured using the pressure gauge. Thus, even with an irregular and spectrally structured multi-mode envelope, which also varies during the spectral scanning, it is possible to accurately model all the features of experimentally recorded MUMAS spectra and to obtain an accurate measure of the partial pressure of the absorbing species.

It is also interesting to note that 'strong' absorption features are detected even at the low partial pressure of 2.79 µbar. These features arise from the cumulative effect of many 'weak' transitions being interrogated by multiple modes such that they occur at approximately the same location in the scan across the intermode-spacing.

5.4 Linewidth measurements

For the multi-mode lasers used for previous demonstrations of MUMAS, the mode-linewidth, of the order of several MHz, was insignificant compared with the Doppler- and pressure-broadened absorption line linewidths (of order GHz) and so was not a critical parameter in the model [7–9].

As described in section 4.5.1, in the case of a multi-mode ICL, the mode-linewidth was measured using MUMAS spectra of a molecule with widely spaced absorption lines so that a feature could be identified as arising from the interaction between a single individual mode and one spectral line. At the operating wavelength of the ICL device used, HCl provided a suitable, open absorption spectrum. The pressure broadening of an isolated

line was measured, and the residual width, found by extrapolating to zero pressure, was assigned to that of the mode responsible. In order to find the mode-linewidth for the QCL used in the work in this chapter, an alternative method is employed since no species with a suitable uncongested spectrum is available at 5.3 µm. This new method again uses measurements of the pressure broadening of absorption features in a MUMAS spectrum. It is assumed that the lineshape of the individual modes can be well-approximated by a Lorentzian of fixed width, $\delta\nu$. Pressure broadening of the absorption lines is also taken to give a Lorentzian profile with a pressure-dependent width, $\delta\tilde{\nu}(p)$. In the usual fitting procedure, values are assigned to both the mode-linewidth, $\delta\nu$, and the pressure-broadened width, $\delta\tilde{\nu}(p)$. However, it is not possible to distinguish, a priori, how much of the resulting width, $\delta\nu_{\mathrm{Total}}(p) = \delta\nu + \delta\tilde{\nu}(p)$, is due to pressure broadening or to the mode-linewidth. The following method is adopted to determine the mode-linewidth.

MUMAS spectra are recorded of a species which absorbs in the region of the laser output, with the partial pressure of the absorbing species held constant and the pressure of the buffer gas varied between different spectra. Modelled MUMAS spectra are fitted to this data. In the model, the mode-linewidth is set to zero, in effect, assigning all the Lorentzian contribution of the feature-linewidth to pressure broadening, $\delta\nu_{\mathrm{Total}}(p) = \delta\tilde{\nu}(p)$. The pressure determined from the apparently pressure-broadened linewidths derived from these fits, i.e. the 'fitted pressure', is plotted versus the 'measured buffer pressure'. Extrapolating the data to zero measured pressure determines the intercept on the 'fitted pressure' axis. This is the pressure that would give a Lorentzian broadening equal to the mode-linewidth at zero pressure. It is necessary to determine the conversion factor that relates this apparent pressure to the corresponding mode-linewidth.

To find the conversion factor, MUMAS spectra are simulated for a range of buffer gas pressures using a mode-linewidth set to zero. For each resulting spectrum, the simulation is repeated but instead setting the buffer gas pressure to zero and adjusting

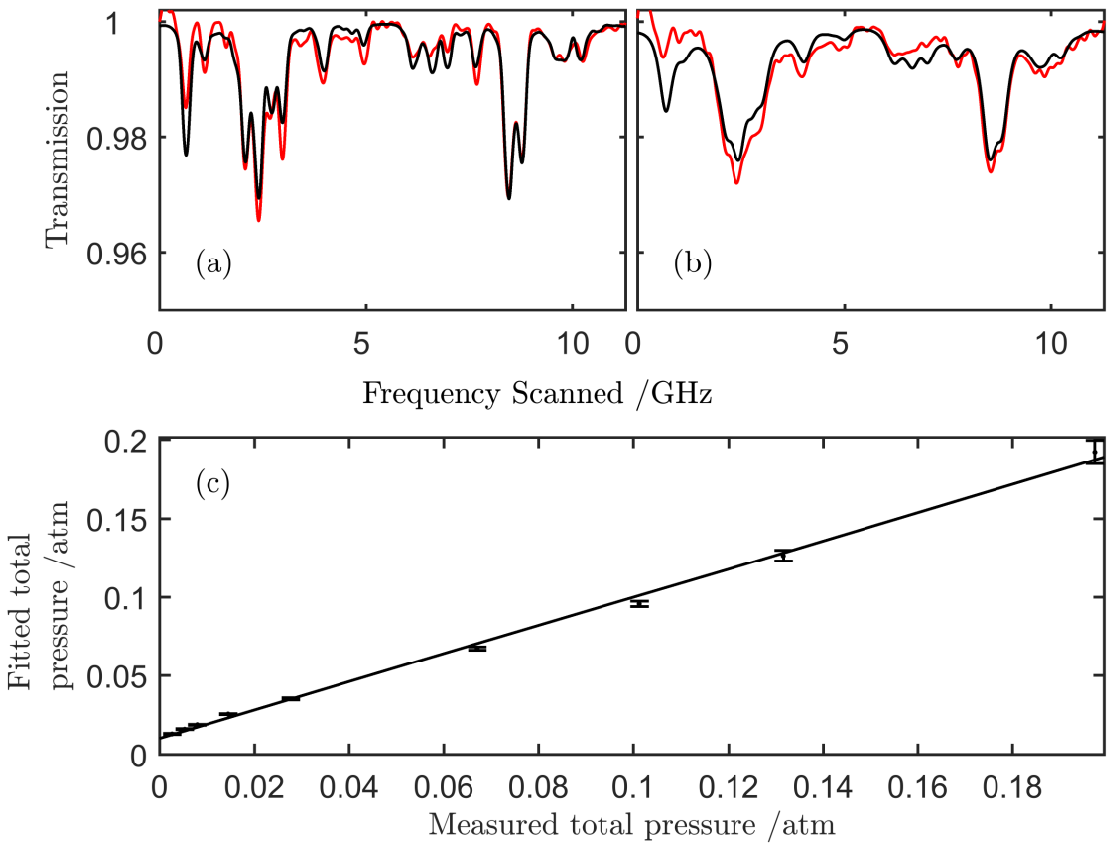

Figure 5.3: MUMAS spectra of NO at 6.7 µbar with N_2 at pressures of 0.94 mbar in panel (a) and 68 mbar in panel (b), respectively. Panel (c) shows a plot of the pressures derived from fits to the data using pressure-dependent broadening as the fit parameter versus the corresonding measured pressures.

the mode-linewidth to give an equivalent spectrum matching the original. A plot of the equivalent mode-linewidth versus the simulated buffer pressure gives the conversion factor. Thus, by using this conversion factor, the mode-linewidth, $\delta\nu$, can be derived from the fitted pressure intercept at zero measured pressure.

Using this method for the laser used in this work, MUMAS spectra are recorded using a partial pressure of 6.7 µbar of NO and variable pressures of N_2 buffer gas. Figure 5.3a and 5.3b show examples of MUMAS spectra recorded with N_2 pressures of 0.94 mbar and 68 mbar, respectively. Figure 5.3c shows the 'fitted pressure' plotted versus

the 'measured buffer pressure' for each spectrum, where the error bars represent the standard deviation of the fitted pressures for 10 sequentially recorded MUMAS spectra. Extrapolating the data to zero measured pressure gives an offset on the 'fitted pressure' axis of 10.3 ± 0.6 mbar, and this is the pressure that would give a Lorentzian broadening equal to the mode-linewidth at zero pressure. The error on the intercept is determined by taking consideration for the uncertainty of each data point on the line [120]. A plot of the equivalent mode-linewidth versus the simulated buffer pressure yields a line-of-best-best whose gradient gives a conversion factor of 6.35 mbar MHz^{-1}. Thus, the mode-linewidth, $\delta\nu$, derived from the fitted pressure intercept at zero measured pressure is found to be 37.62 ± 2.20 MHz. Confirmation of the accuracy of this measurement is obtained by fixing the mode-linewidth at this value and deriving the buffer gas pressure from fits to the same data using the pressure-broadened width as the fit parameter. A plot of derived pressure versus measured pressure yields a straight line with an intercept of 0.06 ± 0.66 mbar, i.e. zero within experimental error. The gradient of the line is 0.9 rather than 1.0 and this deviation is ascribed, as in previous work, to the presence of residual air in the gas-handling system that is not detected by the MUMAS absorption [9].

5.5 Detection of an interfering species

Water vapour is a common 'interfering' species in optical gas sensing owing to both its presence in the atmosphere and having absorption lines across a wide range of the infrared region, including the region of the NO spectrum studied here. To examine its effect, a MUMAS spectrum is first recorded for pure NO at a pressure of 6.7 µbar in the absorption cell. In addition, a small amount, 13.3 mbar, of laboratory air is admitted and a second MUMAS spectrum is recorded. The laboratory air is measured, using a hygrometer, to have a relative humidity of 24.6% and a temperature of 26°C

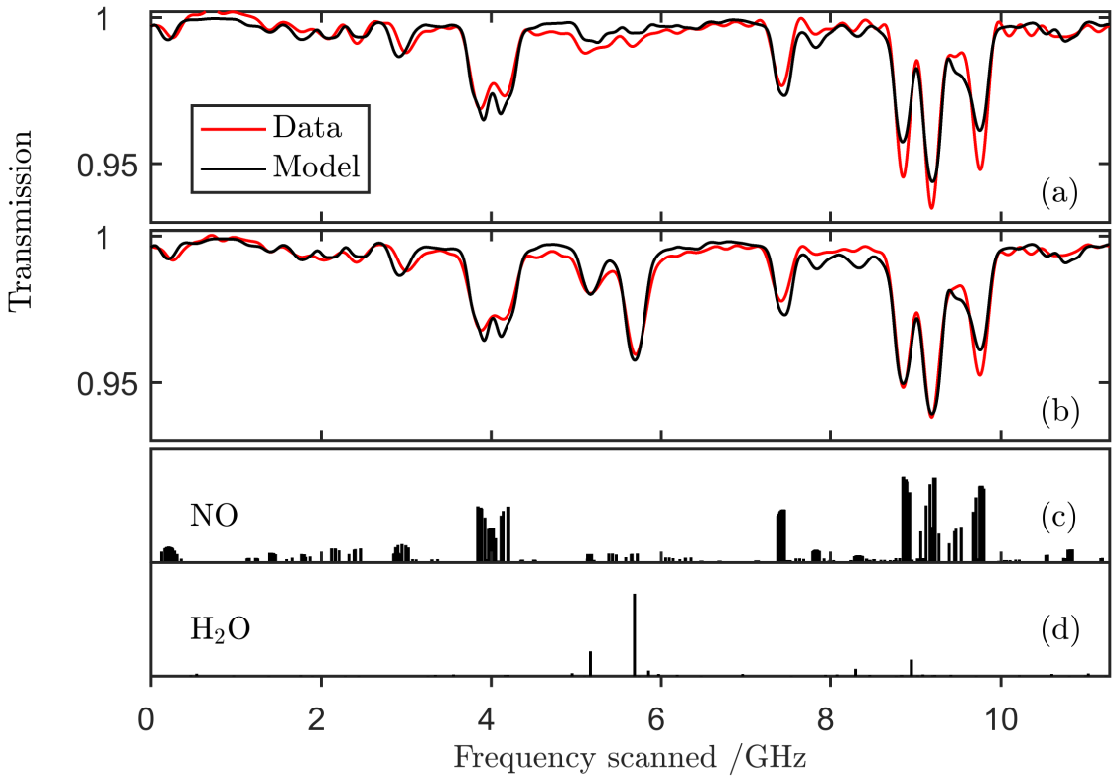

Figure 5.4: Panel (a) shows a MUMAS spectrum of NO at 6.7 µbar (red line) with model fit (black line) using a constant mode envelope calculated from the average of all spectra recorded at seven locations in the scan shown in figure 5.2b. Panel (b) shows a MUMAS spectrum of NO as in panel (a) but with 13.3 mbar of laboratory air added which includes 0.11 mbar of water vapour. Panel (c) and (d) show markers indicating the position of NO and H_2O absorption lines, respectively, where they occur during the scan over the intermode-spacing of ~ 11 GHz.

thus providing a water partial pressure of 0.11 ± 0.01 mbar in the cell [121]. Using the partial pressure as one of the fitting parameters, the H_2O partial pressure is found to be 0.09 ± 0.02 mbar, which agrees within experimental uncertainty with the measured value.

A MUMAS spectrum of pure NO is shown in figure 5.4a (red line) together with a modelled fit (black line). The MUMAS spectrum recorded in the presence of the laboratory air is shown in figure 5.4b where some of the additional features arising from H_2O are clearly distinguishable. The lower panels of figure 5.4 show the position of the

NO and H_2O absorption lines, (c) and (d), respectively, where they occur in the scan across the intermode-spacing. This figure does not represent the spectrum of NO or of H_2O as would be displayed conventionally as a function of wavelength or frequency. Instead, this figure shows a 'stick' feature corresponding to a particular transition where it would occur in a MUMAS spectrum in the scan across an intermode-spacing as one of the longitudinal modes encounters it.

These data illustrate the potential for MUMAS to distinguish background 'interference' from water, or other species, since additional information on the target species being detected is provided at locations where overlapping of absorption lines is less severe or absent. This information allows the relative contributions of a target species, such as NO, to be distinguished from those of an interfering species such as H_2O. This is a particularly advantageous property of MUMAS as H_2O is a common interfering species in many environments.

5.6 Laser intensity envelope effects on data analysis

The data and model fits shown in figure 5.2 and 5.4 show reasonable agreement. However, closer examination reveals some discrepancies, mainly in the relative intensities of absorption features at different positions along the scan across the intermode-spacing. These slight discrepancies are accounted for by the variation in the shape of the mode intensity envelope as the laser modes are scanned across an intermode-spacing as shown in figure 5.2b. As noted above, the analysis of the data and model fitting assume a constant, averaged intensity envelope of the laser modes so that the MFP of each mode in the incident light is assumed to remain constant during the scan.

The Mode Fractional Power (MFP), which was described in section 3.2, is the amount of power in a particular mode as a fraction of the total power in all the modes. The MFP

of the modes varies as the distribution of intensity of the modes changes during the scan. Consequently, the contribution of each mode to the total MUMAS signal will depend on how much its fractional power differs from the assumed, average value when it encounters an absorption line. It is noted, however, that the variation in the mode intensity envelope is correlated with the modulation of the drive current and is not randomly varying – the reproducibility of these variations allows for them to be accounted for in the model and in fitting to the data. In practice, this may be carried out by performing measurements of the laser mode intensity envelope throughout the scan. Moreover, such measurements are often broadened by the finite resolution of the instrument used and so it is also necessary to measure the relevant instrument function.

Inspection of figure 5.2b shows that, for the laser used for this work, the intensity envelope develops a broad 'lobe' at the long-wavelength end of the distribution as the modes are scanned across the intermode-spacing (indicated by an arrow in figure 5.2b). The overall output power also changes but, as this is accounted for using the reference beam, the important issue is that the fraction of the total power contained in any individual mode changes as this lobe develops. The MFP of a mode can increase or decrease during the scan and so its contribution to the total MUMAS signal can increase or decrease correspondingly relative to that predicted for the assumed average value of the envelope. It is possible, in principle, to calculate the contribution of each mode as its MFP changes during the scan. However, this would be computationally expensive and require accurate, high-resolution measurements monitoring the continuous variation of the envelope during a scan. In later work, the modelling code is modified to incorporate data from such a varying laser mode intensity envelope as the modes scan (section 6.4). However, for the present work, the intensity envelope is modelled to be constant. The range of uncertainty introduced by variation of MFP may be estimated by calculation of the fitted modelled MUMAS spectra that would arise if the MFP varied between

the maximum and minimum possible values. Alternatively, the fit may be adjusted at particular locations in the scan to take account of significant changes in the MFP since the effect of such changes will depend on the strength of any known absorption features occurring at that point.

5.6.1 Inaccurate measurement of intensity envelope

As noted above, measurement of the spectral distribution of intensity across the mode envelope needs to account for the finite resolution of the instrument used, in this case an FTIR. The recorded FTIR intensity spectrum of the mode envelope is a convolution of the mode spectrum with the instrument function of the FTIR instrument. Thus, the relative intensities of individual modes can be recovered fully only if the instrument function is de-convolved from the measured data.

This is of particular importance for the work in this chapter as the instrument function of the FTIR instrument ($\sim$ 15 GHz) is similar to the intermode-spacing of the laser ($\sim$ 11 GHz). This results in the individual modes only partially being resolved in the FTIR data and hence their relative intensities are distorted by the inadequate resolution of the instrument.

As the mode-linewidth is much smaller than the FWHM of the instrument function, each mode is simply represented by the instrument function in an FTIR spectrum, and the overall FTIR spectrum is made up of these overlapping instrument functions for each mode. As the wings of the instrument functions contribute to the cumulative intensity at the positions of the adjacent modes, this gives an inaccurate measure of the relative intensities of these adjacent modes. If the intensity envelope were to increase continuously to a peak and then decrease continuously, without any 'dips', then this would not be a significant issue as the intensity of all modes would be approximately overestimated by the same amount, and when the envelope is normalised it would give a reasonably

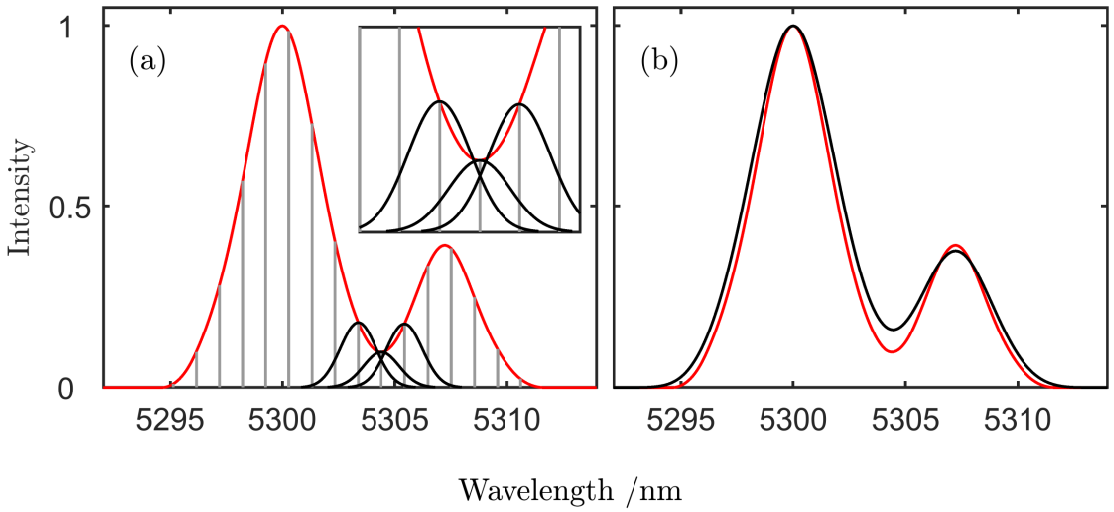

Figure 5.5: An illustration of the inaccuracy in intensity envelope measurements caused by overlapping instrument functions. Panel (a) shows the true mode intensities (grey sticks) of a simulated laser spectrum which has a dip in the middle (red line). The instrument functions of the three modes around the dip in the envelope are also shown (black lines). Panel (b) shows both the true mode intensity envelope (red line), and the normalised mode intensity envelope that would be caused by convolving the true mode-structure with the instrument function of the FTIR. Note that the relative mode-intensity of the mode in the dip has been overestimated by the poorly resolved spectrum.

accurate estimation of the intensity envelope of the laser spectrum. However, if one side of the intensity envelope were not to monotonically increase, but instead had a dip in the middle, then the relatively wide instrument function would be problematic. This is illustrated in figure 5.5 for an intensity envelope with a dip in the middle. Figure 5.5a shows the true mode intensities (grey sticks) of this simulated laser spectrum (red line). Also shown in figure 5.5a are the instrument functions of the three modes around the dip in the envelope (black lines). Figure 5.5b shows both the true mode intensity envelope (red line), and the normalised mode intensity envelope that would be caused by convolving the true mode-structure with the instrument function of the spectrometer. Note that the relative mode-intensity of the mode in the dip has been overestimated. To correct for this inaccuracy the FTIR spectrum is de-convolved with the instrument function.

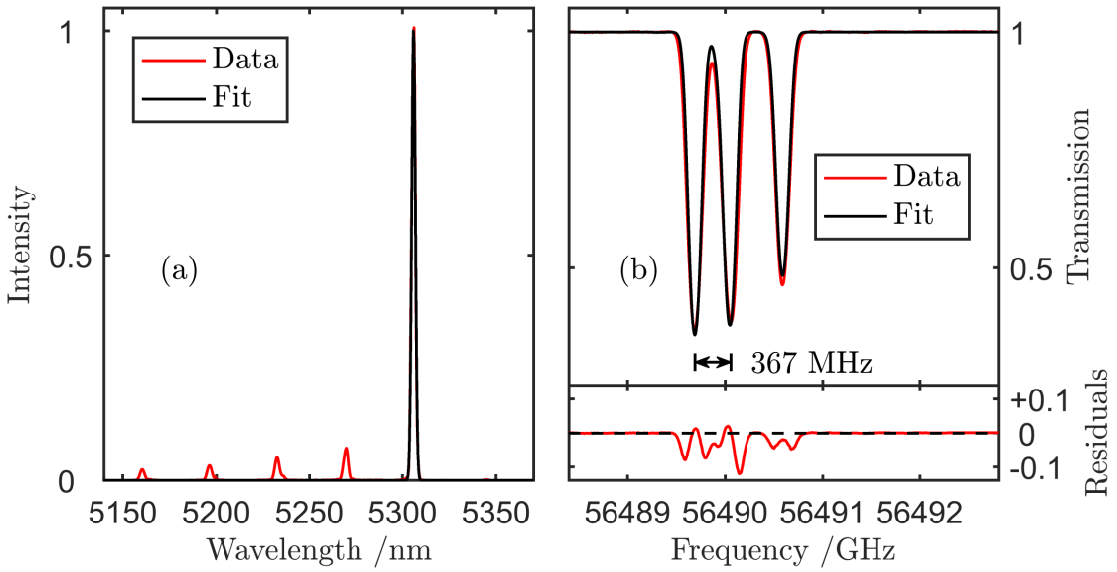

Figure 5.6: Panel (a) shows an FTIR spectrum (red line) of the QCL output at high drive current which results in the output being dominated by a single mode. The black line indicates a Gaussian fit to the dominant single mode and represents the instrument function of the FTIR spectrometer. Panel (b) shows a MUMAS spectrum of the $R(1.5)$ $\nu = 1 \leftarrow 0$ ro-vibrational transitions in NO recorded using the QCL operating in a single longitudinal mode. Data is shown as a red line and the modelled fit is shown as a black line.

The instrument function of the FTIR spectrometer is measured by recording the spectrum of a monochromatic source. A suitable source is produced by increasing the QCL drive current to induce single mode operation. Figure 5.6a shows the FTIR spectrum of the laser output under these operating conditions and shows it to be dominated by a single mode at around 5300 nm. To gain an estimation of the mode-linewidth, the laser is used to record an absorption spectrum of both Λ-doublet components of the $R(1.5)$ $\nu = 1 \leftarrow 0$ ro-vibrational transitions within the $\Omega = 3/2$ and $1/2$ spin-orbit manifolds of NO. The spectrum shown in figure 5.6b (red line) is obtained using 2.63 µbar of NO in the Herriot cell and scanning the laser over 6 GHz. Also shown is a modelled spectrum fitted to the experimental data (black line). The relatively large residual is ascribed to the uncertainty arising from the frequency calibration of the spectrum

using fringes formed by a germanium etalon (as described in section 4.3.3). Since the laser is scanned across this relatively narrow spectral range, there is a relatively large uncertainty in the frequency scale. Nonetheless, the main point of this figure is to show the high spectral resolution provided by the laser operating in a single mode. The spectrum consists of well-resolved Doppler limited features in which the splitting of the e/f Λ-doublet components within the $\Omega = 1/2$ manifold of 367 MHz is readily resolved, indicating that the linewidth of the mode has an upper limit of about 10 MHz and considerably narrower than the nominal 0.5 cm^{-1} (15 GHz) resolution of the FTIR spectrometer. This indicates that this source is sufficiently monochromatic to accurately resolve the FTIR instrument function.

This data shows that, even if some additional longitudinal modes are activated, the vast majority of the output under these drive conditions resides in a single mode as the modelled spectrum, assuming a single mode, accounts for practically all of the measured absorption. Note that when the laser is operated in multi-mode with lower drive current, and lower gain, the mode-linewidth is increased to $\sim$ 37 MHz as reported in section 5.4.

The measured instrument function at 5.3 µm, shown in figure 5.6a, is found to be well-fitted by a Gaussian function. Using this analytical function, the FTIR spectra recorded at each of the different locations in the scan across the intermode-spacing are de-convolved to yield a more accurate representation of the spectral shape of the mode intensity envelope. Such an FTIR spectrum of the QCL operating in multi-mode is shown in figure 5.7a as the red line. The de-convolved spectrum is shown as the black line in figure 5.7b and exhibits several sharp dips where the actual mode intensity is effectively zero. This is in contrast to an assumed non-zero value based on the un-deconvolved, averaged spectrum shown as a red line (see inset to figure 5.7b).

A MUMAS spectrum of H_2O from a sample of laboratory air at 0.11 mbar is shown in figure 5.7c as the red line. A modelled MUMAS spectrum is indicated in the figure as

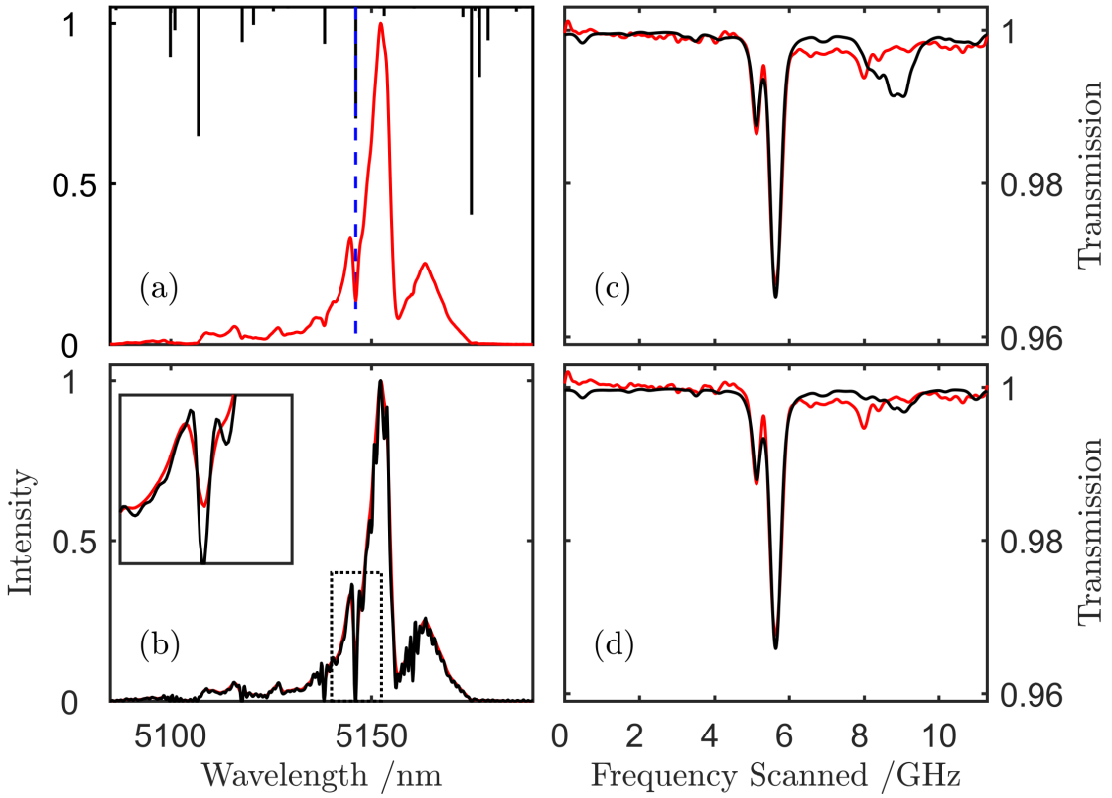

Figure 5.7: Panel (a) shows an FTIR spectrum of a QCL laser output with stick spectra (upper plot) indicating positions of spectral lines of H_2O in this region. Note the strong feature lying at the location of the pronounced dip in the spectrum near 5150 nm indicated by a blue dotted line. Panel (b) shows the output laser spectrum when the instrument function is deconvolved from the data in panel (a). Note that the dip around 5150 nm reaches zero intensity whereas the un-deconvolved spectrum in panel (a) incorrectly indicates a finite intensity at this spectral location. Panel (c) shows a MUMAS spectrum of H_2O (red line) with model fit (black line) showing over-prediction of the contribution of the transition highlighted by a blue dashed line in panel (a) around 8 GHz in the scan when the un-deconvolved laser intensity envelope is used in the model. Panel (d) shows the same MUMAS data as shown in panel (c) but with the model re-calculated using the deconvolved FTIR spectrum of panel (b) showing reduction in the feature at 8 GHz, in better agreement with the data.

a black line which has been calculated using the mode intensity envelope derived using the averaged FTIR spectrum, without deconvolution. This modelled MUMAS spectrum shows some features between 8 and 9 GHz which do not appear in the experimental data. In figure 5.7a, several water transitions lying within the un-deconvolved mode intensity envelope are shown in the upper part of the figure. The vertical blue dotted line in figure 5.7a indicates the position of a particularly strong transition of H_2O which coincides with the pronounced dip in the mode envelope. Since the un-deconvolved envelope assumes a greater MFP in the mode or group of modes interacting with these absorption lines than is actually the case, the model will predict the features shown between 8 and 9 GHz as seen in figure 5.7c. However, when the de-convolved envelope spectrum is used to construct the model MUMAS spectrum, these features are significantly suppressed as shown in figure 5.7d where the model is seen to have a better fit to the data across the entire scan range.

5.6.2 Effect of a varying MFP on MUMAS spectra

The effect of a varying MFP is apparent in the MUMAS spectrum of a mixture of NO and H_2O. Figure 5.8a shows an experimental MUMAS spectrum of the mixture (6.7 µbar NO and 0.44 mbar H_2O) together with a modelled MUMAS spectrum fitted to the data using the un-deconvolved mode intensity envelope. The residuals of the best-fit model, shown in figure 5.8b, show a particular discrepancy around 8 GHz in the scan. The transitions contributing to the signal at this point in the scan are indicated by the red lines in figure 5.8c and are mostly due to H_2O with some contribution from clusters of weaker NO lines. In figure 5.8d, the averaged mode intensity envelope, as measured by the FTIR instrument, is shown as the solid red line. The two envelopes indicated by the dashed and dotted lines show the spectra at the beginning and end of the scan, respectively, from which it can be seen that a significant lobe on the intensity envelope

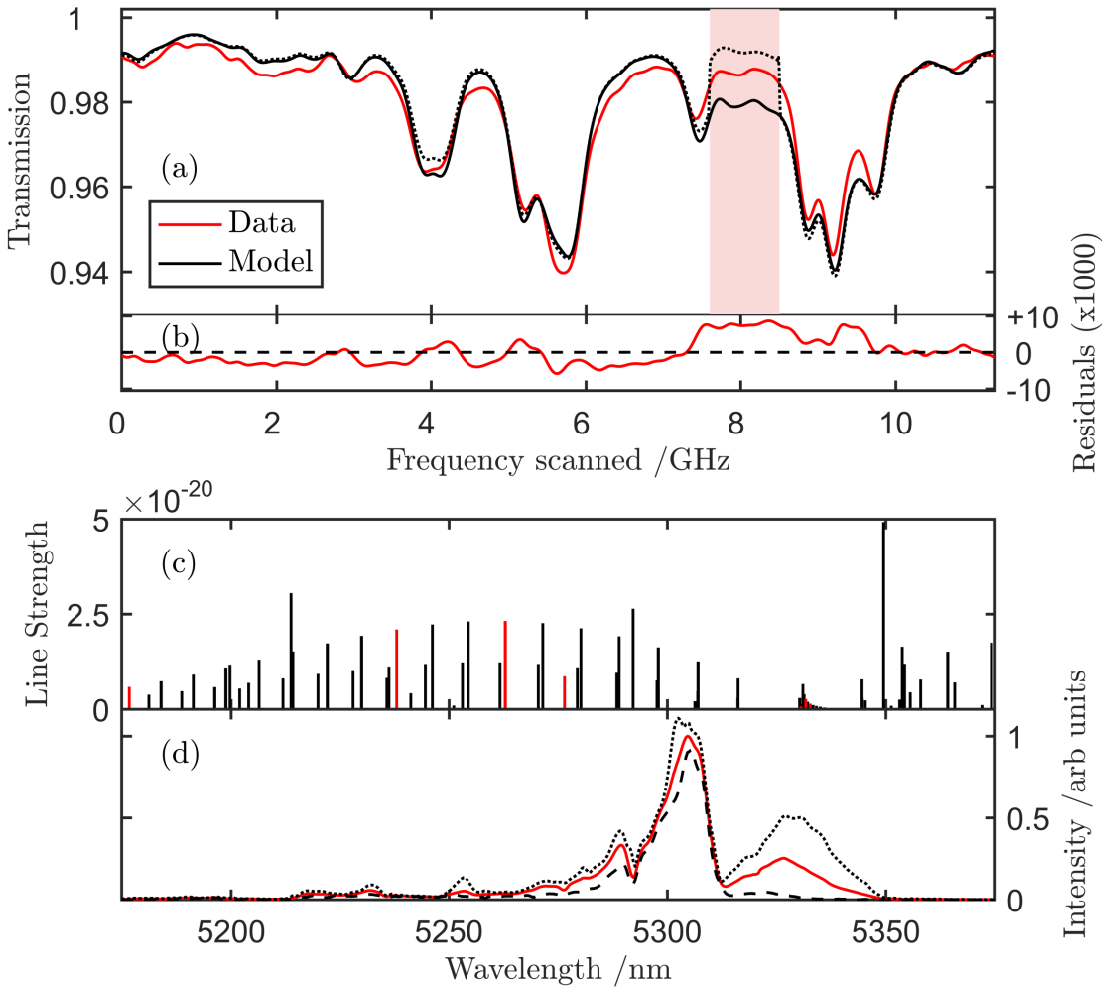

Figure 5.8: A MUMAS spectrum of NO and H_2O illustrating the effect of a changing MFP. In panel (a), the experimental MUMAS spectrum is shown as a red line with a modelled fit using the averaged mode intensity envelope shown as a continuous black line. Panel (b) shows the residuals of the fitted spectrum and highlights the increased discrepancy around 8 GHz. Panel (c) is a stick spectrum indicating the lines in NO and H_2O that contribute to the spectrum in panel (a) as a function of wavelength. The line-strength is given in units of $cm^{-1}/(molecule \times cm^{-2})$. The features marked as red lines are the H_2O lines responsible for the features at ~ 8 GHz in the scan. Panel (d) shows an FTIR spectrum of the QCL output. The solid red line is the averaged laser intensity envelope over the scan. The dashed and dotted lines indicate the spectral shape at the beginning and end of the scan, respectively, and shows the increasing intensity of the lobe between 5300 and 5350 nm. The modelled MUMAS spectrum calculated using the mode intensity envelope appropriate to this part of the scan, which includes the lobe, results in the dotted line shown in panel (a) at ~ 8 GHz. This region is highlighted by a red band.

develops around 5330 nm during the scan. This variation leads to a change in the MFP of those modes responsible for the features at 8 GHz. The modelled MUMAS spectrum is re-calculated for the part of the scan indicated by the shaded column in figure 5.8a around 8 GHz, using the form of the mode intensity envelope appropriate to this part of the scan. The result is that the over-prediction of the MUMAS signal in this region is reduced and the modelled MUMAS spectrum, shown by the dotted line in figure 5.8a, in the region of 8 GHz, is in much better agreement with the data. It is worth noting that, as indicated in red by their spectral location as seen in figure 5.8c, the H_2O lines responsible for the feature at 8 GHz do not lie in the region where the mode intensity envelope changes most dramatically. The change in their contribution arises from the change in their MFP as the growing lobe at 5330 nm accounts for more of the total power of the laser.

5.7 Fast scan rates

All MUMAS data shown in earlier sections in this chapter were recorded whilst scanning the longitudinal modes at a rate of 51 Hz across the intermode-spacing of approximately 11 GHz. The laser used in these studies is capable of being scanned at significantly faster rates. However, the amplitude of the frequency scan is found to decrease at higher scan rates owing to limitations imposed by the drive electronics available. Figure 5.9a and 5.9b show data recorded over a spectral range of 6 GHz at scan rates of 100 Hz and 10 kHz, respectively, from which it can be seen that the resolution of the spectra is not significantly reduced at these faster scan rates. At a scan rate of 50 kHz the spectral range reduced to only 2 GHz. This limited range is still sufficient to include the cluster of features arising from several absorption lines at different 2 GHz wide MUMAS sections within the total bandwidth of the laser. It can be seen in figure 5.9a that some

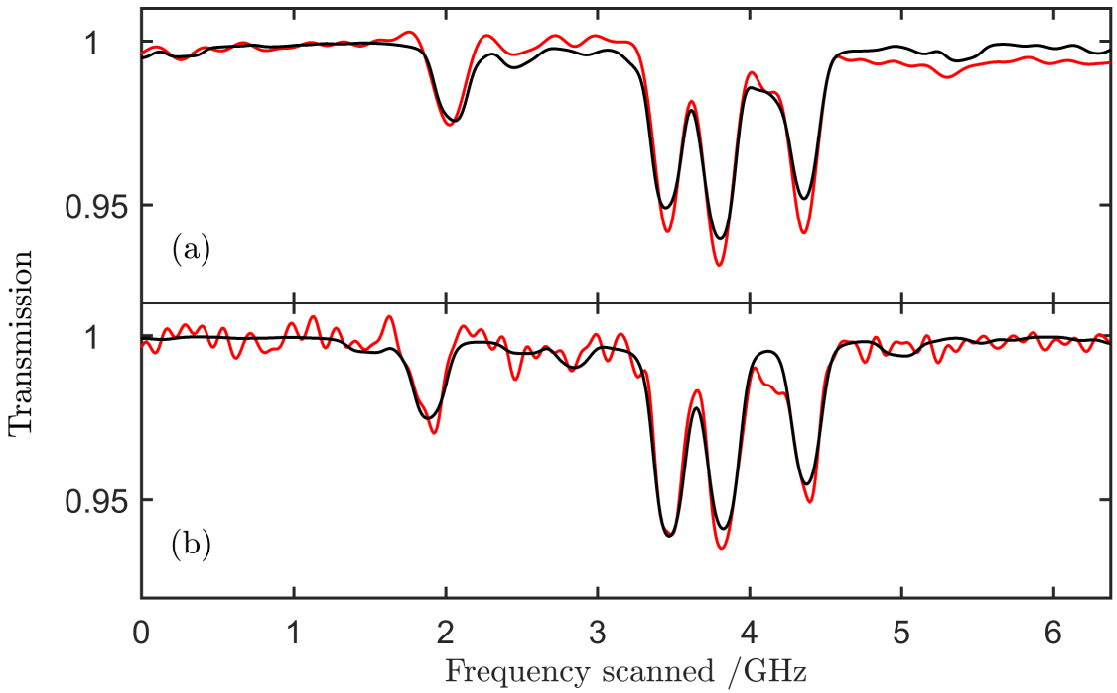

Figure 5.9: MUMAS of NO at scan rates of 100 Hz in panel (a) and 10 kHz in panel (b). The features lying between 2 and 3 GHz in the scans show slightly different profiles owing to the slight change in intermode-spacing arising from a small change in drive current used.

features in the data and fitted MUMAS spectrum between 2 and 3 GHz do not appear at the higher scan rate in figure 5.9b. These differences are accounted for by the slightly different laser drive current used at the higher scan rate which resulted in a slightly altered intermode-spacing. The drive current is adjusted between the two scan rates in order to avoid some transient features that appear at the start of the scan at the faster scan rate. Thus, some extra absorption features are detected at 100 Hz that are absent at 10 kHz. These results, however, demonstrate the potential for gas sensing with fast response times. Drive electronics with a higher bandwidth should allow an increase in scan rate with consequent decrease in measurement times. In process control applications or studies of rapidly varying molecular concentrations, fast response times ($\sim$ 10s of µs) will be advantageous.

5.8 Conclusions

The work in this chapter demonstrated the first application of a QCL to MUMAS in the mid-infrared region of the spectrum. Multiple transitions of the NO molecule were detected over a bandwidth of 50 cm^{-1}, which was determined by the transmission of the interference filter. In addition, in the presence of laboratory air containing water vapour, transitions of H_2O were simultaneously recorded, thereby demonstrating the ability to distinguish interfering species in the gas sample. A new method was developed for measuring the individual mode-linewidths, which uses pressure broadened MUMAS spectra, and the mode-linewidth of the QCLs used in this chapter was measured to be 37.62 ± 2.20 MHz.

It was observed initially that the fits to the data were not optimal, and in particular, the relative intensities of MUMAS absorption features were not accurately modelled. The source of this inaccuracy was found to arise from the erroneous assumption that the intensity envelope of the laser modes was constant during the scan. Hence, the effect of a varying intensity envelope was investigated with the aim of gaining further understanding with which to ultimately improve the MUMAS modelling. In addition, the effect of the instrument function on the measured intensity envelope was considered, and was corrected in order to give more accurate representations of the intensity envelope of the laser modes in the modelling process.

A key demonstration of the work in this chapter is that MUMAS can be applied using a commercially available QCL device which exhibits not only strong variations across the spectral intensity distribution when the modes are not being scanned but also significant changes to the MFP during the scan over one intermode-spacing. It has been shown that including such variations of the QCL output, measured independently, in the modelling procedure allows more accurate fits to experimental data. Further analysis of

the intensity envelope of the laser spectrum provided further understanding of how to accurately model a MUMAS spectrum.

Finally, it has been shown that MUMAS data can be obtained at fast scan rates, up to 10 kHz, and beyond if a suitable driver is available. This enables gas sensing with short measurement times, which is important for applications in rapidly changing environments or for active process control.

Chapter 6

Development of MUMAS in the near-infrared region

6.1 Overview

The work reported in this chapter extends previous MUMAS studies which were performed in the near-infrared region of $1-2$ μm [5]. It addresses some of the limitations of MUMAS which were highlighted in section 4.6.

The previous work used a custom-built diode-pumped Er:Yb:glass laser because, at that time, the diode lasers operating in the near-infrared region exhibited unstable mode behaviour that made accurate modelling of the data difficult. In addition, the detection system, a simple ratio monitor, had a relatively high noise level. Furthermore, the intermode-spacing and scan rate of the laser limited its use to low pressures. However, in the work described in this chapter, commercially available diode lasers which have a sufficiently large intermode-spacing are used to obtain MUMAS spectra at atmospheric pressures.

Until the work described in this chapter, the detection scheme used for MUMAS was

that used for conventional absorption spectroscopy in which the intensity of the probe and reference beams were measured using two independent detectors and the ratio of the two was taken post-acquisition. An alternative detection scheme, *balanced ratiometric detection*, is developed for the work in this chapter. There are a number of advantages of this alternative over the standard scheme, including both an improvement in the noise characteristics and the operation of the technique. These advantages are explored in this chapter.

One of the practical issues of MUMAS has been obtaining a laser whose mode intensity envelope remains constant as the laser modes scan. In previous work, efforts were made to suppress variations in the mode intensity envelope as the modes scan by using a suitably chosen filter. However, for the lasers used for the work in this chapter, a suitable filter is not found. Instead of trying to control the mode intensity envelope, the issue is solved by incorporating data of the variation of the mode intensity envelope into the modelling process. By relaxing the restriction on the mode intensity envelope, it opens up the possibility of having a much wider selection of multi-mode lasers available for performing MUMAS.

The absorption strengths of molecular transitions are temperature dependent, and the rate of change of the absorption strength with temperature differs for different molecular transitions. Therefore, as MUMAS detects multiple transitions, the technique can be used as a thermometer. This capability is demonstrated by using a commercially available diode laser to measure the temperature of CO_2 in a gas cell. Potential improvements in the temperature sensitivity are subsequently investigated.

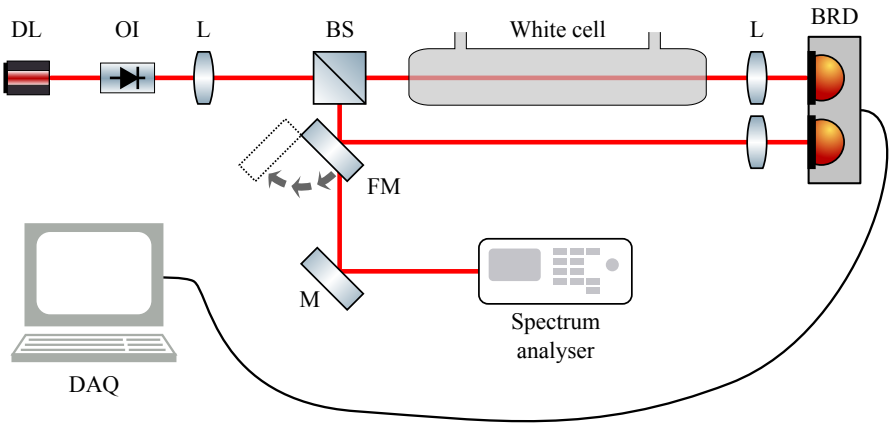

Figure 6.1: A schematic of the experimental setup used for MUMAS with the near-infrared diode laser (DL). L: lens, OI: optical isolator, BS: beam splitter, FM: flip-mirror, M: mirror, BRD: balanced ratiometric detector, DAQ: data acquisition.

6.2 Experimental details

For the work described in this chapter, the experimental apparatus and procedure are similar to that used for all previous MUMAS work, and are described in detail in section 4.3. A standard optical setup is used to measure the transmission through samples of the target gases using direct absorption spectroscopy. A schematic of this experimental setup using the near-infrared diode lasers is shown in figure 6.1.

The multi-mode laser used is a commercially available, pig-tailed diode laser (Q-Photonics QFLD-1570-10S) which provides 9 mW of power at 1.57 µm. A fibre coupled optical isolator (Thorlabs IO-H-1550APC) is connected in series to the diode laser and is necessary to avoid parasitic feedback into the diode laser. The diode laser is powered using a current-driver (Thorlabs LDC 205B) and the temperature is maintained at 32.2°C by a TEC temperature controller (Thorlabs TED 200C). Scanning is effected using a function generator to control the drive current (Agilent 33500B Series). Unlike in previous MUMAS work, an optical interference filter is not used to remove some of the irregular spectral structure of the laser spectrum. Instead, as will be described in section 6.4, the

modelling code is modified to incorporate data describing the varying laser mode intensity envelope as the modes scan. The intensity envelope of the laser spectrum is measured at various points along the scan using a Michelson Interferometer (Bristol Instruments, 721-B IR). These measurements are made only once as the output laser spectra are found to be reproducible. The mode-linewidth is measured using the same technique as that used in chapter 5, and it is described briefly in section 6.5.1. For the work in this chapter, two different gas cells are used. Gas mixtures are either contained in a multi-pass White cell (Specac, Tornado 20) with an effective path length of 16 m, or in a double-pass custom-built stainless-steel gas cell with angled windows. It is possible to insert the stainless-steel gas cell into a tube furnace (Carbolite CTF-1200) to perform temperature measurements of a heated sample of gas. A thermistor is located at the centre of this gas cell to measure the temperature, but does not obstruct the beam path, and the temperature is monitored using a digital multimeter (Caltek Instrument CM1200T). Pressure in both cells is monitored using a capacitance manometer (Setra 730, quoted accuracy 0.25% down to a pressure of 0.025 mbar). For all the partial pressure values presented in this chapter, the uncertainties in the measured pressures are derived from the uncertainties in the readings from the capacitance manometer, and the uncertainties in the fitted pressures are derived from the range of values corresponding to a $\pm 5\%$ deviation in χ^2 from the best-fit value. Incident and transmitted laser intensities are measured using two different detection schemes, *standard detection* and *balanced ratiometric detection*, and digitally recorded using the same data-acquisition device (Handyscope HS4). In the standard detection scheme, individual photodiodes (Thorlabs DET-10C) are used for each channel. An alternative detection scheme, based on a balanced ratiometric circuit and incorporating two photodiodes (Thorlabs FDGA05), is developed and is described in section 6.3.

As in previous work, the intermode-spacing is determined from fits of modelled

MUMAS spectra to MUMAS data of a known species recorded under known conditions of concentration, temperature and pressure. For this laser, 20.5 mbar of CO_2 is used. The intermode-spacing is found to be 69.487 ± 0.012 GHz, however, it is only possible to scan the laser modes across a frequency range of ~ 46 GHz. The uncertainty value is based on the range giving 5% deviation from the minimum of the χ^2 in the fitting procedure. The narrow scanning range is due to the limited range of driving currents which can be applied to the device, which are between the lasing threshold at the lower drive currents and potential output facet damage at higher drive currents.

6.3 Balanced ratiometric detection scheme

Balanced ratiometric detection is a detection scheme which is able to effectively cancel laser intensity noise. This leads to an improved SNR which results in sensitivity enhancements.

In the standard detection scheme, the intensity of the probe and reference beams are measured using two independent detectors. Both of these measurements are independently recorded with a digital data acquisition system. Post-acquisition, MUMAS spectra are calculated as the ratio between the measured transmitted intensity of the probe and incident, or reference, beams. However, in the balanced ratiometric detection scheme, two detector elements, one each for the probe and reference beams, are embedded into a single detection device. The circuitry of this detection device electronically 'balances' the intensity of the probe and reference beams before electronically calculating the ratio of the two intensities. There is a single output from the device, corresponding to the ratiometric operation of the balanced probe and reference beams. In effect, the division of the probe and reference beams is done in circuitry rather than computationally at the processing stage.

There are a number of advantages of a balanced ratiometric detection scheme over

a standard detection scheme. One way of enhancing the sensitivity of a MUMAS measurement is to reduce the noise of the signal, and hence increase the SNR. Excess noise, spurious modulation, and power drift or power supply ripple in lasers are common problems in optical measurements, and these all result in increased noise in the MUMAS signal. A balanced ratiometric detection scheme is able to significantly reduce these sources of noise and hence increase the SNR of the signal. The circuit works by subtracting photocurrents directly, and ideally, the excess noise and spurious modulation will cancel at all frequencies.

Alongside the improved noise characteristics, there are additional operational benefits of a balanced ratiometric detection scheme. In order to record a MUMAS signal, it is only necessary to record a single channel, rather than both the intensity of the probe and reference beams, thereby relaxing the requirements of the data acquisition device. In the standard detection scheme, sloping baselines or stable baseline artefacts, arising from differences in the beam paths after the beam splitter which are not attributable to the absorbing species, are removed by dividing the transmission signal by that of the empty gas cell. However, in the balanced ratiometric detection scheme, the circuitry effectively eliminates these sloping baselines and stable baseline artefacts, thus a transmission signal of the empty gas cell is no longer necessary. Instead, only a single measurement of the zero-absorption level is necessary for calibrating the zero-absorption baseline of the MUMAS spectrum. Both of these operational benefits also result in simpler data processing. Furthermore, in the standard detection scheme, the MUMAS signal that is recorded of the empty gas cell for correcting the baseline is typically recorded a few minutes before the MUMAS signal of the gas sample. As well as complicating the operation of the MUMAS technique, the non-simultaneity of these measurements coupled with slow laser drift results in an imperfect correction of the sloping baseline when using this method. This is not an issue for the balanced ratiometric detection scheme as the

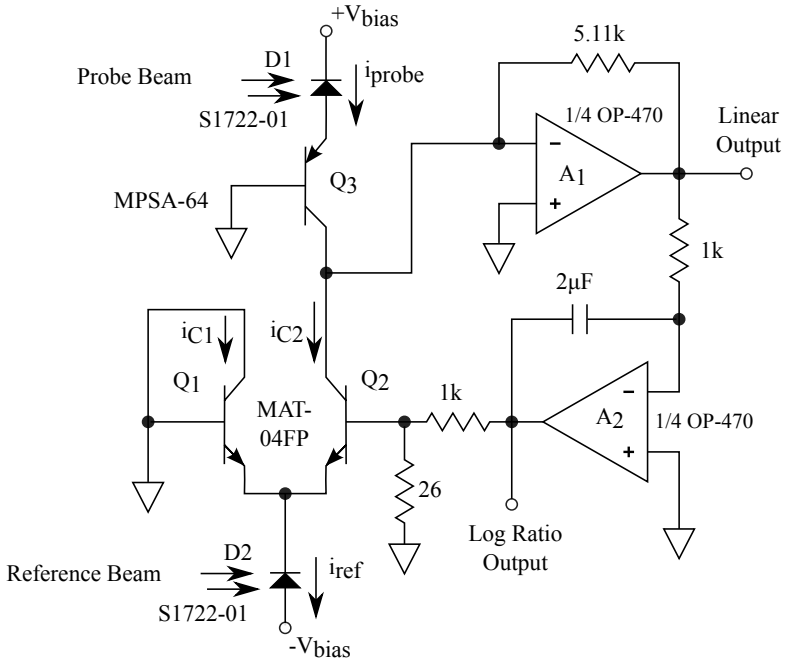

Figure 6.2: Schematic diagram of the circuit used for the basic noise canceller, from [122].

baseline is continually corrected in real-time.

A schematic of the circuit used for the balanced ratiometric detection scheme is shown in figure 6.2 and is described more fully in [122]. The key innovation of this method over other electronically-ratioed techniques is to replace the optical balancing necessary in these techniques with electronic balancing. Electronic balancing is achieved by balancing the photocurrents of the probe and reference photodiodes at the summing junction of the operational amplifier, A_1, so that its output is nulled. In operation, if the photocurrent of the reference beam exceeds the photocurrent of the probe beam, the reference beam photocurrent is split across the differential bipolar junction transistors, Q_1 and Q_2, to regain balance. This is effected by using the integrating feedback amplifier, A_2, to hold the output of A_1 at zero by adjusting the base-emitter voltage of the transistor pair. Two noise-canceled outputs are available: a high-pass filtered voltage proportional to the

signal photocurrent and a low-pass filtered voltage related to the log ratio of the probe and reference photocurrents. The voltage proportional to the log ratio, $V_{\log}$, is given by equation 6.1, where i_{probe} and i_{ref} are the photocurrents of the probe and reference beams, respectively.

$$V_{\log} = -\log\left(\frac{i_{\text{ref}}}{i_{\text{probe}}} - 1\right). \tag{6.1}$$

The photocurrents of the probe and reference detectors are proportional to the beams' intensities. Therefore the MUMAS signal, T^E, is given by the ratio of the photocurrents of the probe and reference beams. Re-arranging equation 6.1 provides the transformation necessary to convert the recorded signal from the balanced ratiometric detection scheme into a MUMAS signal (equation 6.2).

$$T^E = \frac{i_{\text{probe}}}{i_{\text{ref}}} = \frac{1}{\exp\left(-V_{\log}\right) + 1}. \tag{6.2}$$

6.3.1 Dynamic range improvements

As outlined in section 4.6, an enduring limitation of MUMAS is the poor dynamic range of the detection scheme. As each mode only represents a portion of the total transmitted intensity of the light, the absorption signals of the total transmission are therefore small. These small absorption signals will appear on a large DC offset, and so most of the vertical resolution of the data acquisition device is unused, resulting in poor dynamic range.

The balanced ratiometric detection scheme solves the problem of poor dynamic range. For this work, the absorption depth of a MUMAS absorption feature as a proportion of the zero-absorption value is used as the definition of the dynamic range of a particular detection scheme. For the standard detection scheme, the dynamic range is given by

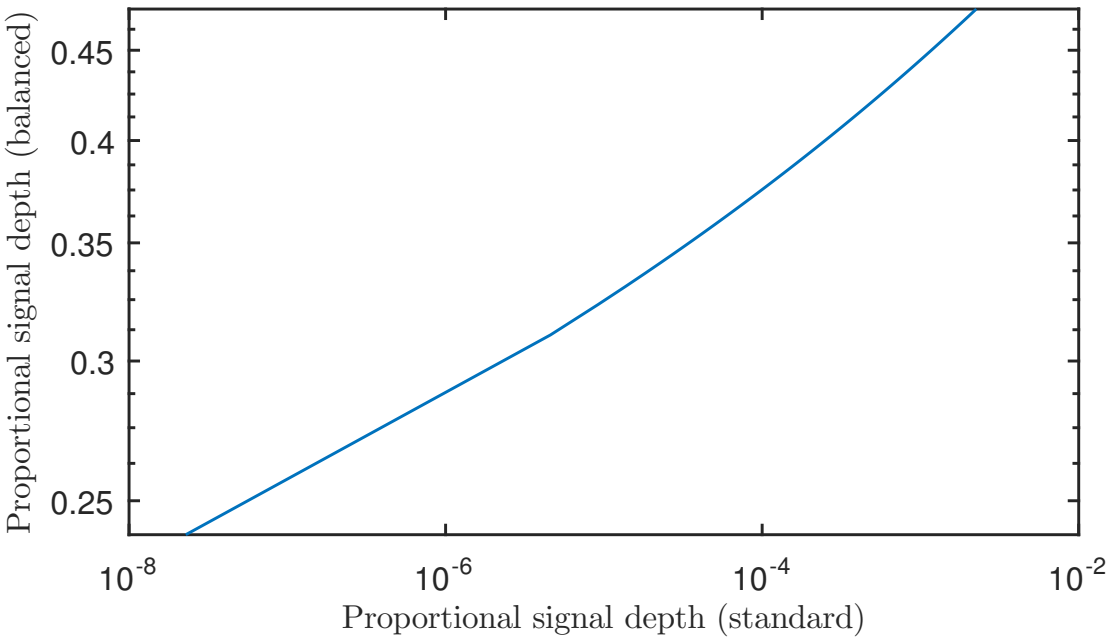

Figure 6.3: Comparison of the proportional signal depths between a balanced ratiometric detection scheme and a standard detection scheme.

$(1 - T^E)$, whereas for the balanced ratiometric detection scheme, the dynamic range is given by $V_{\log}$. Figure 6.3 is a plot of the dynamic range of the standard detection scheme against the dynamic range of the balanced ratiometric detection scheme, for various absorption depths of a MUMAS absorption feature. For small absorption depths, the gradient of this relationship is 2×10^4. Therefore a small absorption feature recorded using the standard detection scheme would have a dynamic range approximately 2×10^4 larger when recorded using the balanced ratiometric detection scheme. Consequently, the dynamic range is significantly improved with the balanced ratiometric detection scheme, hence relaxing the vertical resolution requirements of the data acquisition system.

6.3.2 Comparison of detection schemes

A MUMAS spectrum of 34.2 mbar of CO is recorded using both detection schemes. The MUMAS signals from each scheme are shown in figure 6.4. Each signal is taken as the

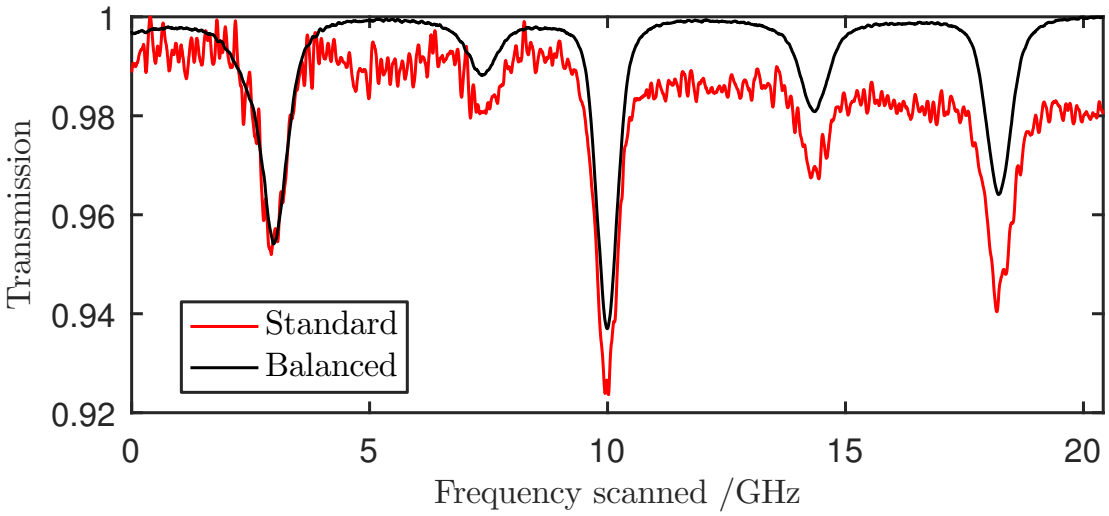

Figure 6.4: MUMAS spectra taken using the standard detection scheme (red line) and the balanced ratiometric detection scheme (black line).

average of 100 individual spectra. It is clear from the figure that, when compared with the standard detection scheme, the noise on the MUMAS signal is significantly less when recorded with the balanced ratiometric detection scheme. Furthermore, the MUMAS signal recorded using the standard detection scheme has a sloping baseline which is unable to be corrected for by a MUMAS signal recorded of an empty gas cell. This is likely due to the drift in the laser between when the MUMAS signal is recorded for the empty cell and when the MUMAS signal is recorded for the cell containing the gas sample. As the baseline is continuously corrected in real-time for the balanced ratiometric detection scheme, the laser drift is not an issue and the resulting baseline is flat.

Due to the enhanced noise performance and the improved operational characteristics, the balanced ratiometric detection scheme is used for the rest of the work in this chapter.

6.4 Computational modelling of a varying laser intensity envelope

One of the practical limitations of MUMAS is obtaining a laser whose mode intensity envelope remains constant as the modes scan. This has been especially true for commercial lasers where it seems that there has been no engineering effort focussed on controlling the mode intensity envelope as the modes are scanned.

In previous work, it has been possible to suppress the variations in the mode intensity envelope as the modes scan by using a suitably chosen filter. However, for the lasers used for the work in this chapter, a suitable filter is not found. Furthermore, the variations in the mode intensity envelope are so drastic that the mode intensity envelope is significantly different at the start and end of a scan of one intermode-spacing. Therefore, a filter would be ineffective at suppressing variations. Instead of trying to control the mode intensity envelope, the issue is solved by incorporating data of the variation of the mode intensity envelope into the modelling process.

In order to incorporate the variation of the mode intensity envelope into the model, it is necessary to know the position along the MUMAS spectrum at which a particular measurement of the mode intensity envelope occurs. In order to do this, an 'anchoring', or reference, feature is necessary. For each measured mode intensity envelope, the laser is tuned to each of the corresponding anchoring features before the mode intensity envelope is measured. The anchoring features used for this work are the MUMAS absorption features of both CO_2 and CO, as shown in figure 6.5b, labelled 'A' to 'I'. The mode intensity envelopes that correspond to each of these features are shown in figure 6.5a in the correct position along the frequency scanned scale, and are correspondingly labelled 'A' to 'I'. It is clear from this figure that the mode intensity envelope changes significantly

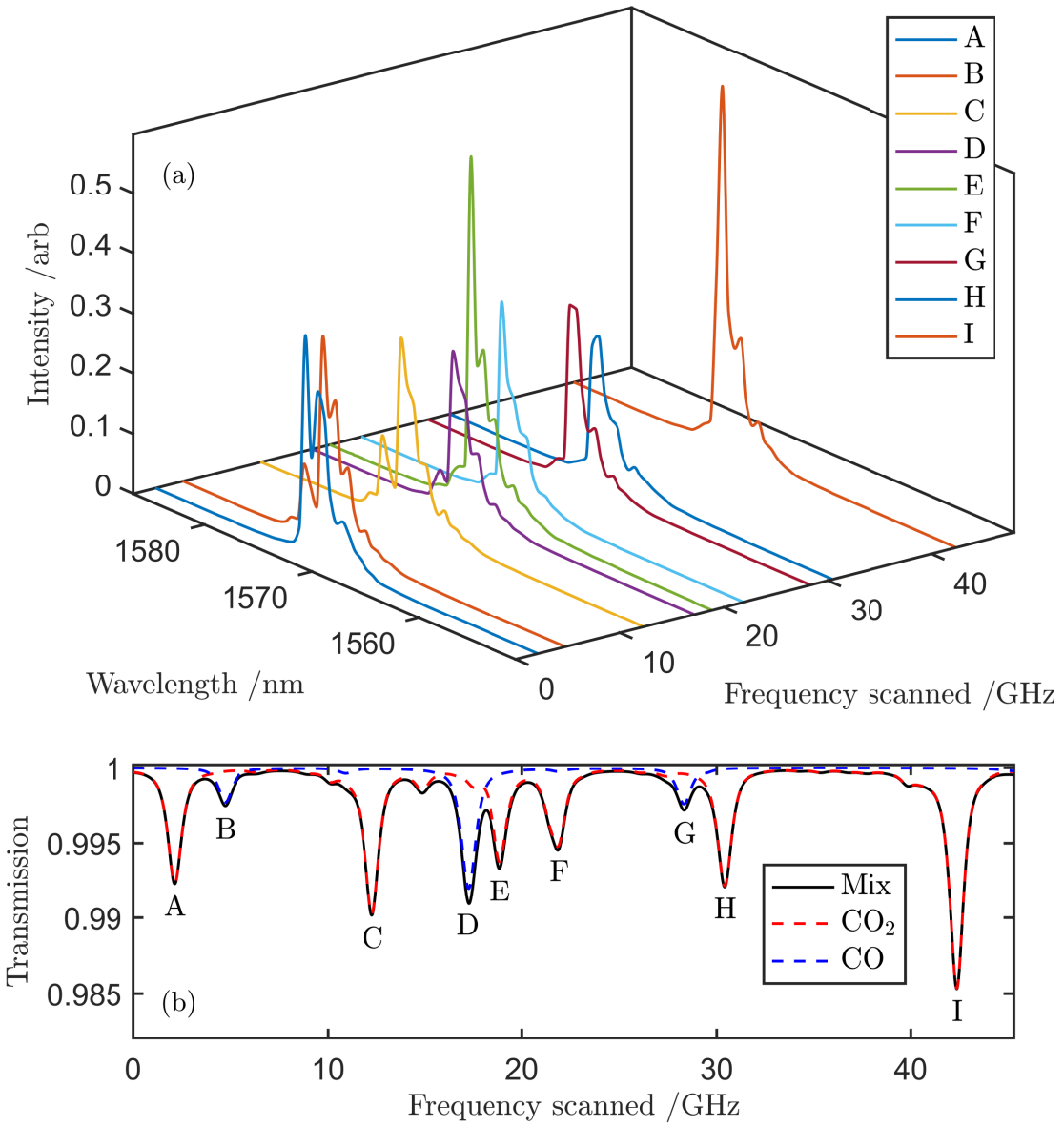

Figure 6.5: Panel (b) shows the CO_2 and CO anchoring features which have the mode intensity envelopes in panel (a) assigned to them. Panel (a) shows the mode intensity envelopes of the laser when it is tuned to a position where one of the modes interacts with either a CO_2 or CO transition. Each of these mode-envelopes, labelled 'A' to 'I', corresponds to the features in panel (b).

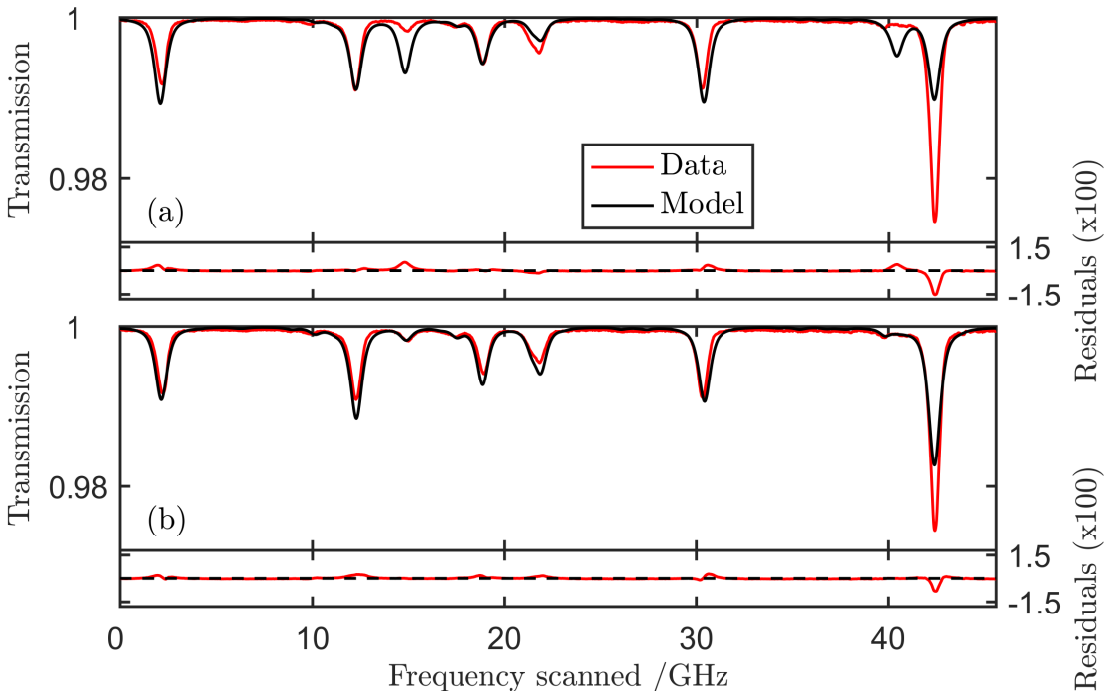

Figure 6.6: Panel (a) shows a fitted spectrum of CO_2 using a constant mode intensity envelope. Panel (b) shows the same spectrum of CO_2 fitted with a varying mode intensity envelope which comprises the data from figure 6.5a.

across the scan. A 2D linear-interpolation is used to estimate the mode intensity envelope between these measured mode intensity envelopes. When calculating a modelled MUMAS spectrum, this 2D linear-interpolation of the mode intensity envelope is used to calculate the MFP of the interacting modes at all positions along the scan.

Figure 6.6 shows a spectrum of CO_2 fitted using both a constant mode intensity envelope (figure 6.6a) and a varying mode intensity envelope (figure 6.6b). The various mode intensity envelopes in figure 6.5a are used to model the varying mode intensity envelope. It is clear that the spectrum fitted using the varying mode intensity envelope has a much more accurate fit. This varying mode intensity envelope will be used for the rest of the work in this chapter.

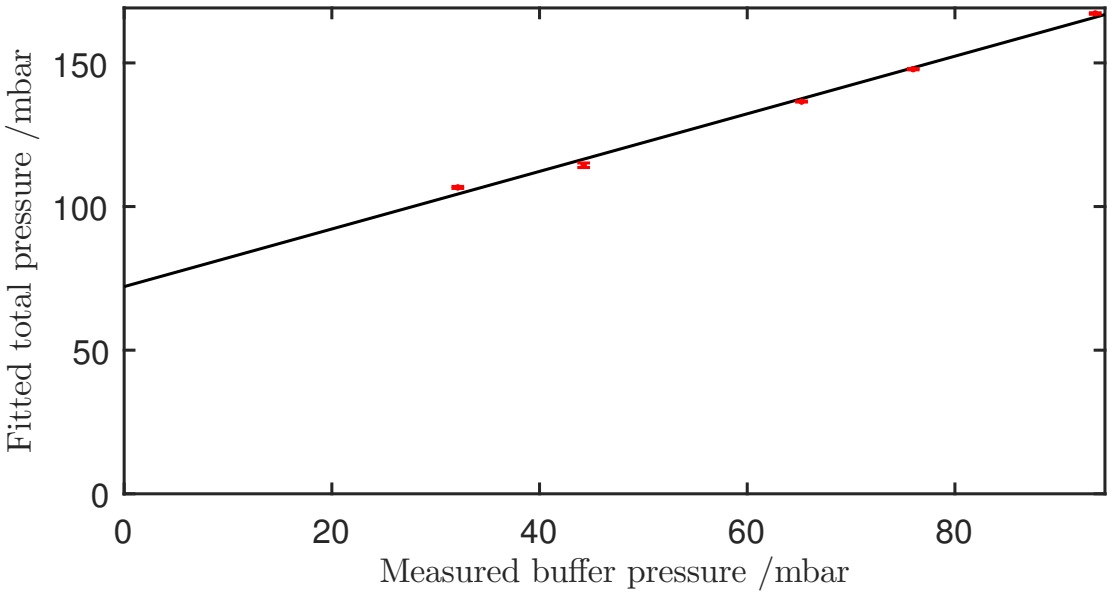

Figure 6.7: Fitted buffer pressure against measured buffer pressure for a range of CO_2 spectra with different buffer pressures, whilst assuming zero mode-linewidth. When extrapolated to zero, the intercept gives a Lorentzian component which corresponds to the mode-linewidth of the laser modes.

6.5 MUMAS with balanced detection and a varying mode intensity envelope

The rest of the work in this chapter will make use of both the balanced ratiometric detection scheme and the new modelling code which accounts for the varying mode intensity envelope.

6.5.1 Linewidth measurements

The mode-linewidth contributes towards the spectral width of the measured MUMAS absorption features and it limits the ultimate spectral resolution of the MUMAS technique. However, in practice it is usually much smaller than the spectral width of the MUMAS absorption features being detected and so its value is not critical. Nonetheless, it is still

important to measure it for this particular laser to ensure that it will have negligible effect on a MUMAS spectrum. The mode-linewidth is calculated using the same method which was used in section 5.4. MUMAS spectra of CO_2 are recorded over a range of buffer pressures, and the total buffer pressure is used as one of the fitting variables whilst also assuming zero contribution from the mode-linewidth. The apparent pressure determined from the pressure-broadened linewidths derived from these fits, i.e. the 'fitted pressure', is plotted versus the 'measured buffer pressure' and is shown in figure 6.7. Extrapolating the data to zero measured pressure determines the intercept on the 'fitted pressure' axis. This is the pressure that would give a Lorentzian broadening equal to the mode-linewidth. To find the conversion factor to relate this apparent pressure to the corresponding mode-linewidth, MUMAS spectra are simulated for a range of buffer gas pressures using a mode-linewidth set to zero, and then for each resulting spectrum, the simulation is repeated but instead setting the buffer gas pressure to zero and adjusting the mode-linewidth to give an equivalent spectrum matching the original. A plot of the equivalent mode-linewidth versus the simulated buffer pressure yields the conversion factor. Accordingly, the mode-linewidth, $\delta\nu$, derived from the fitted pressure intercept at zero measured pressure is found to be 325.13 ± 8.62 MHz. This is much larger than the linewidth of the lasers used in previous MUMAS work, which suggests that this laser has a lower Q-Factor. However, due to the much larger intermode-spacing of these lasers, it only has a small effect on the resolution of the MUMAS spectra.

6.5.2 Multi-species detection

In order to demonstrate the multi-species capability of the laser used for this work, a mixture of CO and CO_2 is interrogated. The red line in figure 6.8b shows a MUMAS spectrum of CO and CO_2 and the modelled spectrum is shown as a black line. Figure 6.8a and 6.8c show fitted individual spectra of CO and CO_2, respectively.

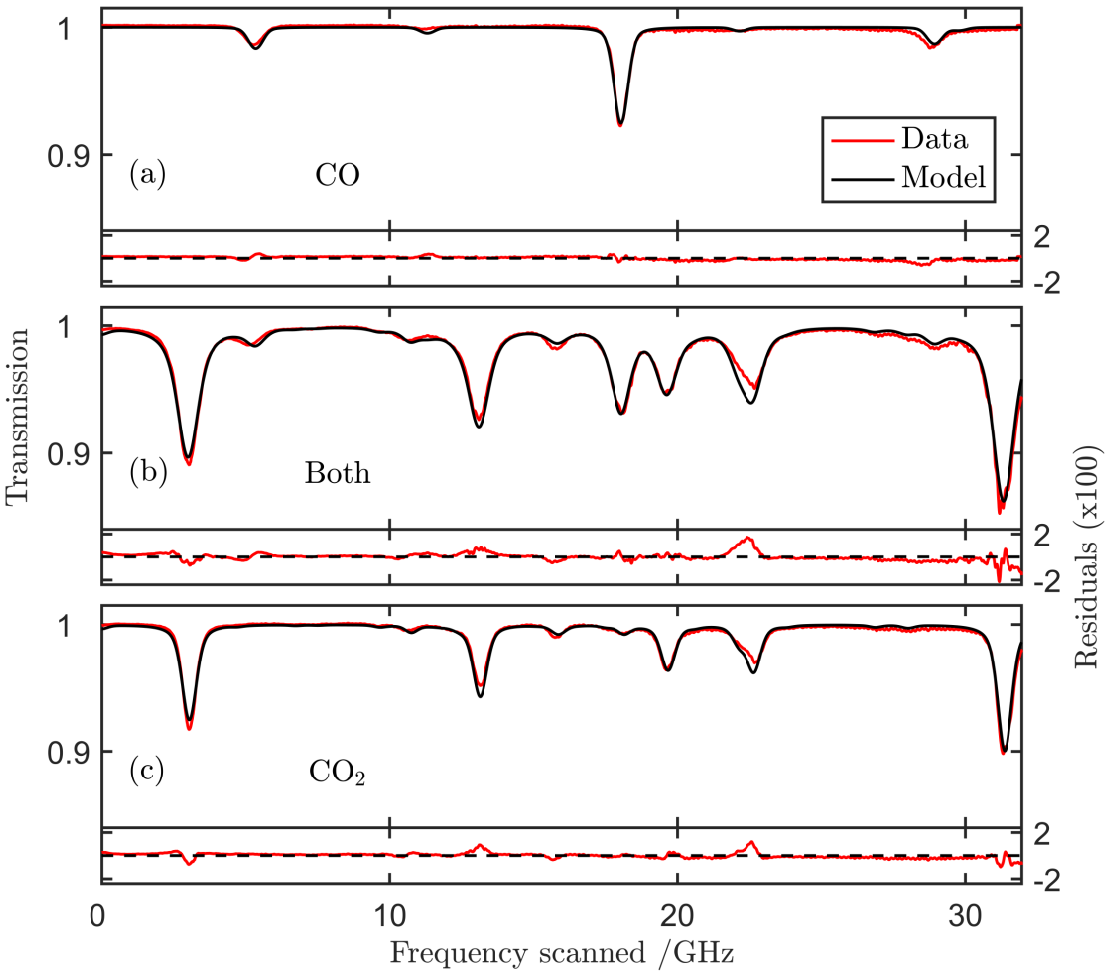

Figure 6.8: Panel (a) shows a fitted spectrum of CO, panel (b) shows a fitted spectrum of CO and CO_2 and panel (c) shows a fitted spectrum of CO_2. The experimental data are shown as red lines and the modelled MUMAS spectra are shown as black lines.

It is clear that the model is able to accurately model all the absorption features of both species. Furthermore, the peaks are well resolved which make it less likely for a featureless MUMAS spectrum to result when it is pressure broadened.

The concentration, or partial pressure, of both gases is determined to be that giving the best-fit to the data. Using this method, the CO and CO_2 partial pressures are determined to be 19.2 ± 0.9 mbar and 21.0 ± 0.9 mbar for the individual pure samples, respectively, which agrees within experimental uncertainty with the values of 19.1 ± 0.1 mbar and 20.5 ± 0.1 mbar measured using the capacitance manometer.

The same sample of CO that was used for analysing the individual pure sample is used for producing the mixture, whilst a new sample of CO_2 is added to complete the mixture. In the mixture, the CO_2 partial pressure is determined to be 49.1 ± 2.3 mbar which agrees within experimental uncertainty with the measured value of 49.6 ± 0.2 mbar. When in a mixture, the partial pressure of CO is determined to be 19.6 ± 2.4 mbar, which also agrees within experimental uncertainty with the measured value of 19.1 ± 0.1 mbar. The error on the partial pressure of CO when in a mixture is larger than in the individual pure samples, and this is expected as the other interfering species will result in fewer regions with zero-absorption and therefore more uncertainty in the fitted partial pressure.

6.5.3 Atmospheric pressure sensing

Figure 6.9a is the MUMAS spectrum of CO_2 which is also shown in figure 6.8c. Given the wide intermode-spacing of ~ 70 GHz, there is low spectral congestion of MUMAS features and there is a zero-absorption baseline for the majority of the spectrum. The spectrum in figure 6.9b is a MUMAS spectrum with the same quantity of CO_2, but broadened by 1 atm of N_2. Rather than being featureless, a distinctive MUMAS spectrum results. This is the first demonstration of MUMAS for species detection at atmospheric pressure using a commercially available laser.

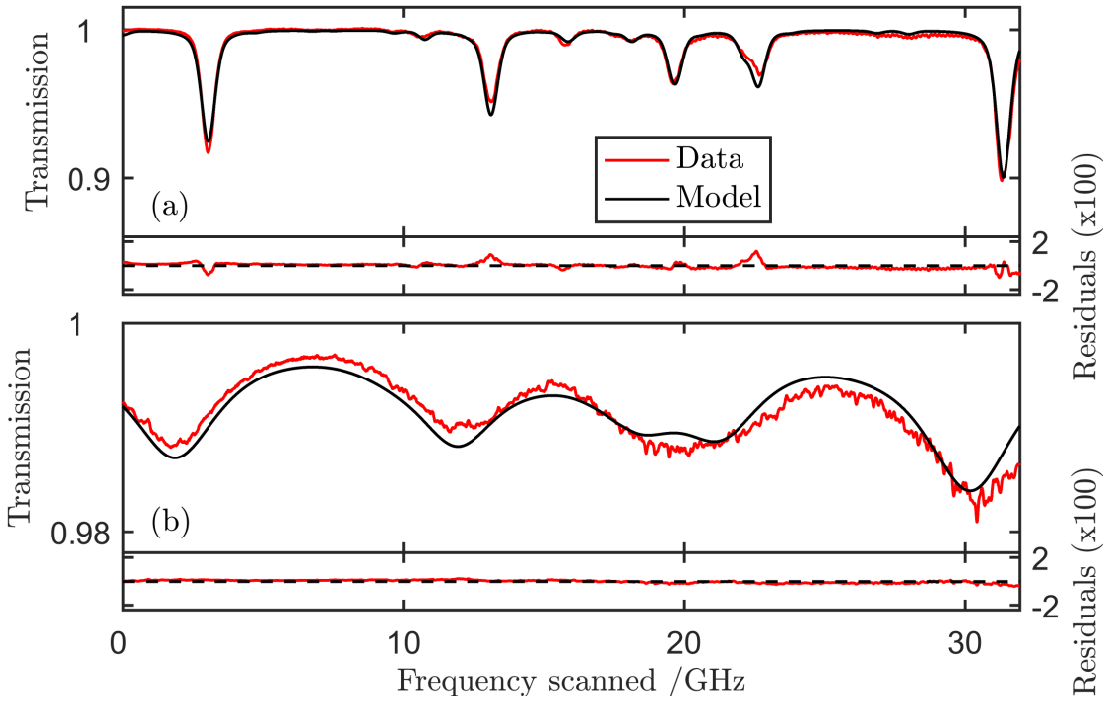

Figure 6.9: Panel (a) shows the fitted spectrum of CO_2 replicated from figure 6.8c. Panel (b) shows the same spectrum of CO_2 but broadened by 1 atm of N_2.

6.6 Thermometry with MUMAS

Section 6.5.2 described how a commercially available diode laser combined with a balanced ratiometric detection scheme was used to simultaneously detect CO and CO_2. The potential applications of this multi-species capability were explored in section 2.5. However, in addition to containing multiple species, certain environments may also have unknown temperatures. Environments at different temperatures will affect the MUMAS spectra which are recorded and the data analysis which follows, and it is therefore necessary to measure the temperature of the environment being probed. Generally this will involve an additional measurement technique which may also need to be restricted to being non-invasive or resilient to harsh environments, thereby adding further complexity to a potential gas sensing device. However, as has been demonstrated in previous work

on MUMAS, it is also possible to measure temperature using MUMAS [3].

The potential temperature sensing capability arises because the absorption strengths of molecular transitions are temperature dependent, and the rate of change of the absorption strength with temperature differs for different molecular transitions. Therefore, as MUMAS is able to detect multiple transitions, the technique can be used as a thermometer.

Different spectral regions will have different rates of variation of the absorption strength with temperature, and therefore there are optimum spectral regions in which to probe in order to maximise temperature sensitivity. Unfortunately the laser used for this work probes a spectral region where the relative absorption strengths do not vary appreciably with temperature. Despite this limitation, the possibility of also using this commercial laser to perform thermometry of a sample of CO_2 is explored, and the potential improvements in temperature sensitivity by interrogating a different spectral region are investigated.

6.6.1 Temperature measurements

In order to demonstrate the ability to measure temperature, a MUMAS experiment is performed with the gas cell and its contents heated to different temperatures. For the gas sample, 22.5 mbar of CO_2 is admitted into a 95 cm long, double-pass cell. A tube furnace covers the middle 65 cm of the cell and water cooling rings abutted to the ends of this tube furnace keep the ends of the gas cell at room temperature. To monitor the temperature inside the cell, a thermocouple is inserted into the centre of the gas cell, but does not obstruct the beam path. MUMAS spectra are obtained with the gas cell heated to temperatures of up to 730 K and the spectra are shown in figure 6.10 as red lines.

For the preliminary fitting procedure, the temperature distribution of the gas in the cell is assumed to be uniform. Modelled, fitted MUMAS spectra are shown in figure 6.10

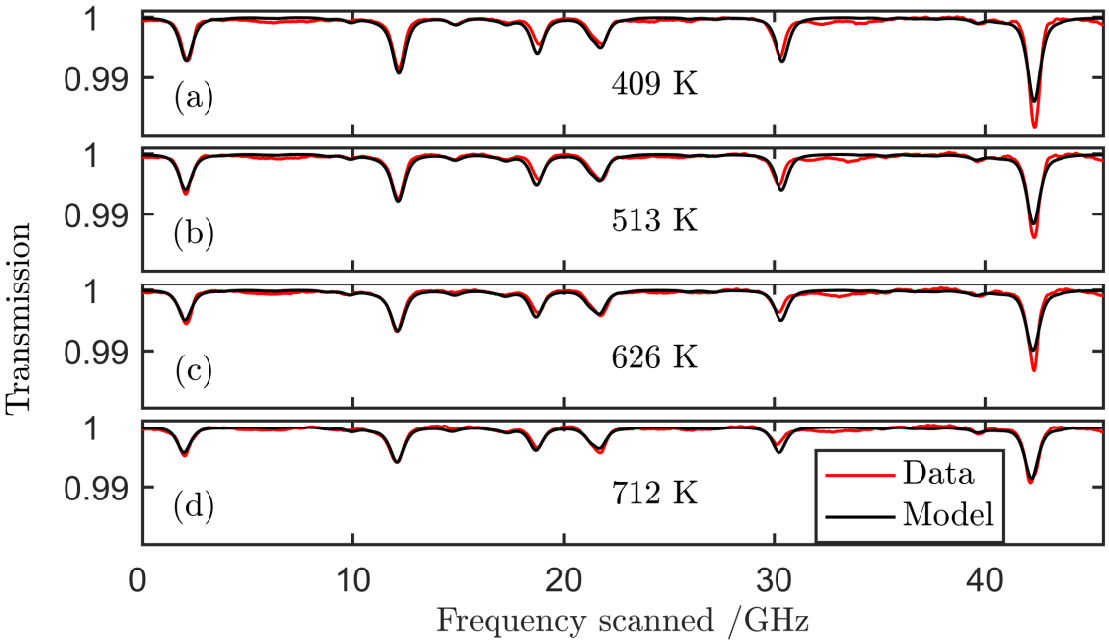

Figure 6.10: Panels (a)-(d) show MUMAS spectra at a range of temperatures. The experimental data are shown as red lines and the modelled spectra are shown as black lines. The models assume a uniform temperature distribution in the gas cell. The measured temperature from using the thermocouple is given in the panel for each spectrum.

as black lines. The modelled spectra give reasonably good fits to the experimental data over the range of temperatures involved.

In order to obtain a value for the temperature from the model, temperature is used as one of the fitting variables. A plot of measured temperature against fitted temperature is shown in figure 6.11. It is clear that there is a linear relationship between the two temperatures. However, the gradient of this relationship is 0.3. This is a large discrepancy from unity which results in poor accuracy for the derived temperatures.

The reason for the large discrepancy from unity is that, unlike in the modelling procedure, the temperature distribution in the gas cell is not uniform. The tube furnace only covers the middle $\sim 68\%$ of the length of the gas cell, and the cooling rings ensure that the gas at the ends of the gas cell are kept at room temperature. Therefore, there is a

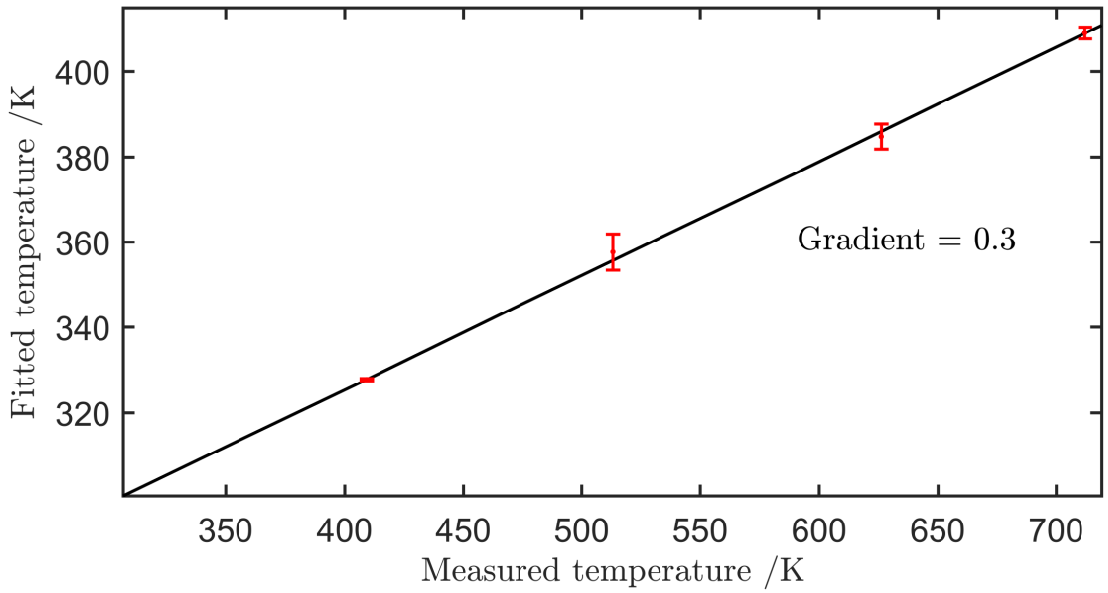

Figure 6.11: Fitted temperature against measured temperature for the spectra in figure 6.10, where a uniform temperature distribution in the gas cell is assumed. The gradient of the line-of-best-fit for this graph is 0.3.

non-uniform temperature distribution within the gas cell and the probe beam encounters gas at a range of temperatures. The resulting MUMAS features are due to the cumulative absorptions of varying relative magnitudes from different temperature regions in the line-of-sight of the beam.

Higher temperatures decrease the absorption strength of all the CO_2 transitions being probed with this laser. The combination of MUMAS features caused by colder gas at the ends of the gas cell and MUMAS features caused by hotter gas near the centre of the gas cell results in the MUMAS fitting routine over-compensating for the colder gas by predicting a lower temperature than the measured temperature from the thermocouple in the middle of the cell. This results in the gradient of the line-of-best-fit in figure 6.11 being less than one.

Subsequently, the modelling code is modified to account for the non-uniform temperature distribution of the line-of-sight of the probe beam. The modelled temperature

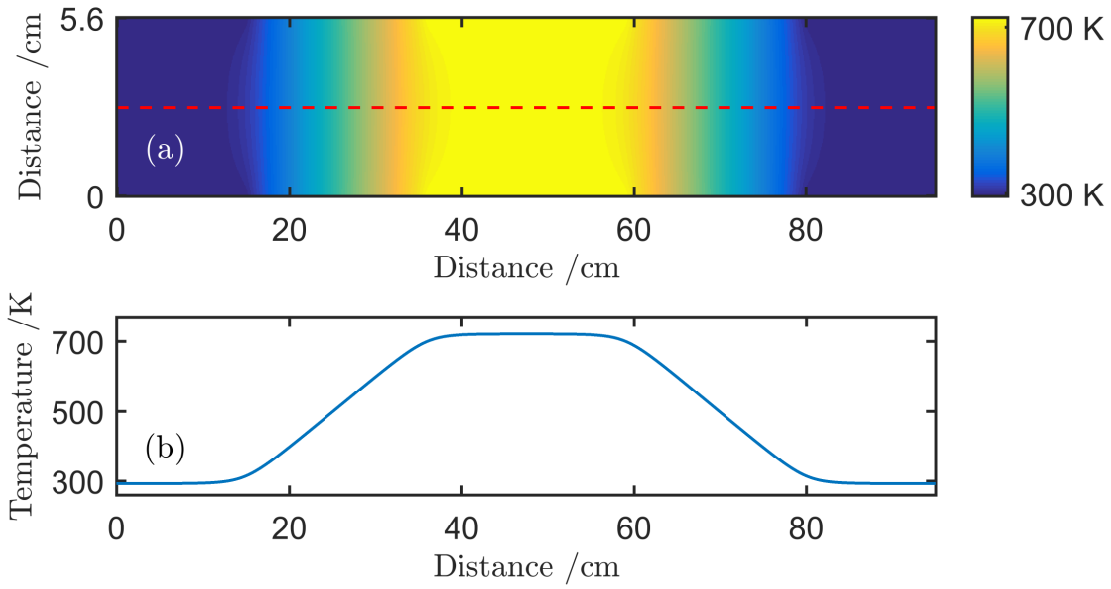

Figure 6.12: Panel (a) shows a simulated temperature map of the gas cell using a numerical, finite-differences transient heat conduction model. Panel (b) shows the temperature profile of a cross-section through the centre of the cell, as highlighted by the red, dashed line in panel (a).

distribution is simulated using a numerical, finite-differences transient heat conduction model. A 2-dimensional rectangle is used to simulate the gas cell, the length and diameter of which are 95 cm and 5.6 cm, respectively. The technical specification for the tube furnace states that the middle 23 cm of the tube furnace is held at a uniform temperature. The full length of the tube furnace is 65 cm, and since no further information is given on the temperature profile along the length of the tube furnace, the temperature profile is approximated to vary linearly between the temperature of the cold regions at the ends of the tube furnace (which are kept at room temperature by the cooling rings abutting the ends of the tube furnace) and the temperature of the heated, uniform region in the middle of the tube furnace. Thus, for the boundary conditions for the finite-differences transient heat conduction model, the middle 23 cm at the top and bottom of the rectangle representing the gas cell are held at the high-temperature, the 15 cm sections at the

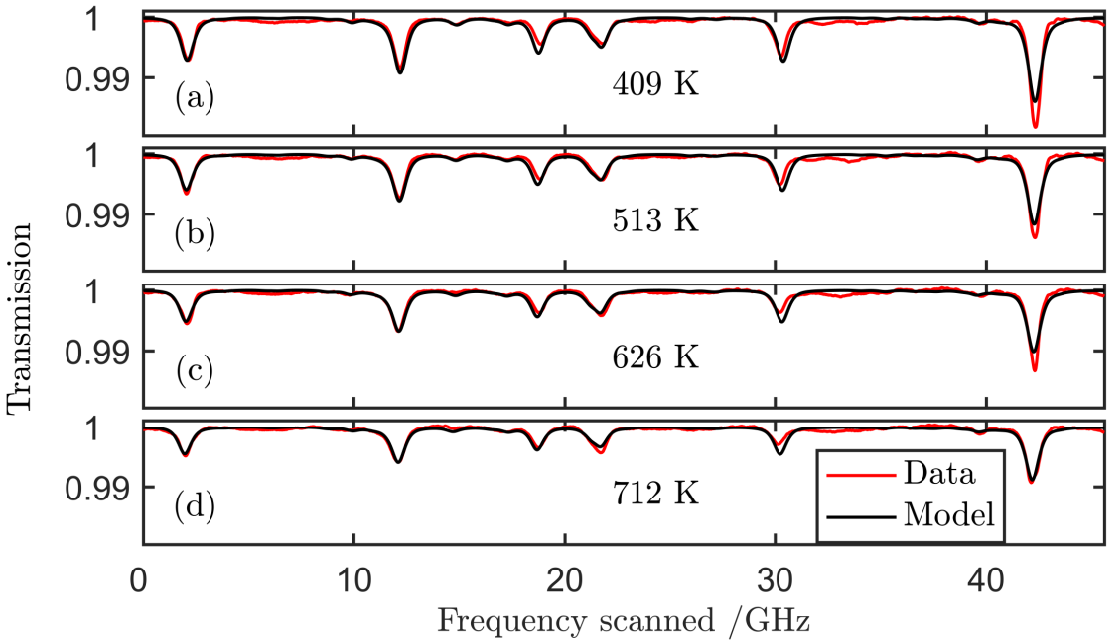

Figure 6.13: Panels (a)-(d) show MUMAS spectra at a range of temperatures. The experimental data are shown as red lines and the modelled spectra are shown as black lines. The models assume a non-uniform temperature distribution in the gas cell. The temperature distribution is calculated using a numerical, finite-differences transient heat conduction model and is illustrated in figure 6.12. The measured temperature from using the thermocouple is given in the panel for each spectrum.

ends of this rectangle are held at room temperature (293 K), and the temperature of the remaining boundaries varies linearly between the room temperature of the cold boundaries and the high-temperature of the heated, uniform boundaries. A temperature map of the resulting simulation is shown in figure 6.12a. A cross-section taken through the line-of-sight of the cell is shown in figure 6.12b.

In the fitting procedure, the fitted temperature is the temperature at the centre of the gas cell as this is where the thermocouple is placed in the cell. Modelled fits to the range of MUMAS spectra are shown in figure 6.13 as black lines. Again, the modelled spectra give good fits to the experimental data over the range of temperatures involved. A plot of measured temperature against fitted temperature is shown in figure 6.14. It is

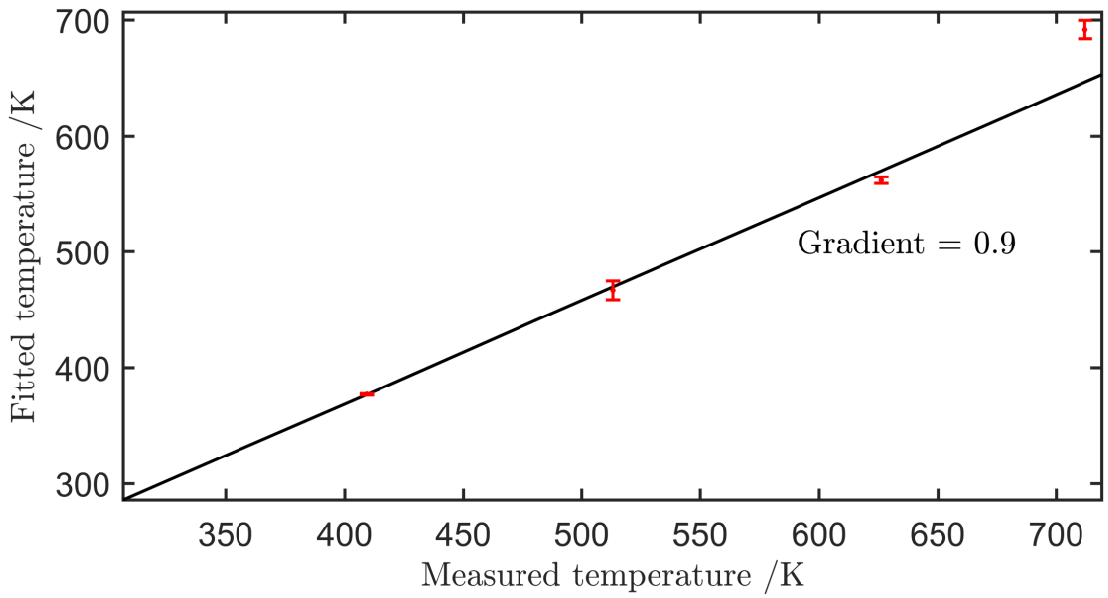

Figure 6.14: Fitted temperature against measured temperature for the spectra in figure 6.13, where the temperature distribution is calculated using a numerical, finite-differences transient heat conduction model and is illustrated in figure 6.12. The gradient of the line-of-best-fit for this graph is 0.9.

clear that this relationship is not as linear when compared with the relationship when assuming a uniform temperature distribution in the gas cell. The most likely reason for this is, again, the inaccurate temperature distribution in the simulations. Despite accounting for the cold ends of the gas cell, the assumption for the temperature along the boundaries of the tube furnace is likely to be inaccurate.

Although not perfect, this simulated non-uniform temperature distribution is a better approximation than a uniform temperature distribution. Furthermore, with this more accurate model for the temperature distribution, the gradient of the line-of-best-fit between the two temperatures is 0.9, which is much closer to a gradient of one than the gradient of 0.3 which is calculated when assuming a uniform temperature distribution in the gas cell. Therefore, these proof-of-principle experiments indicate that MUMAS can be used as a method of measuring temperature provided that the temperature distribution

of the line-of-sight is taken into account.

It is clear that the experimental apparatus used in this work is not ideal for investigating the temperature sensing capability of MUMAS. A better setup would involve a gas cell which is fully submerged in a furnace so that the temperature of the gas in the line-of-sight is at a uniformly high-temperature. Despite the imperfections of this experimental setup, the temperature sensing capability of MUMAS can still be investigated and, accordingly, the sensitivity of these temperature measurements is investigated in section 6.6.2, below.

6.6.2 Temperature sensitivity

To obtain a measure of the temperature sensitivity of the MUMAS spectra in figure 6.13, the χ^2 is determined for the comparison between each experimental spectrum and a range of modelled spectra which are at temperatures slightly either side of the temperature of each experimental spectrum. The result of this χ^2 calculation is taken to be the error function. An example error function is shown in figure 6.15. The minimum occurs when the temperature of a modelled spectrum matches the temperature of the experimental spectrum, and the variation of the error function is approximately parabolic near this minimum. A measure of the temperature sensitivity, or the precision, is the temperature range which gives a 5% deviation from the minimum of the error function. A more temperature sensitive MUMAS spectrum will produce a narrower parabola and hence a smaller value for this sensitivity metric.

Using this '5%-deviation in χ^2' metric, the average temperature precision of the MUMAS spectra in figure 6.13 is found to be 3.2%. This temperature sensitivity is specific to this spectral region of CO_2. As mentioned previously, the laser used for this work probed a spectral region where the relative absorption strengths did not vary appreciably with temperature. A laser operating in a more temperature sensitive region of this band of CO_2 transitions would give better precision for the temperature

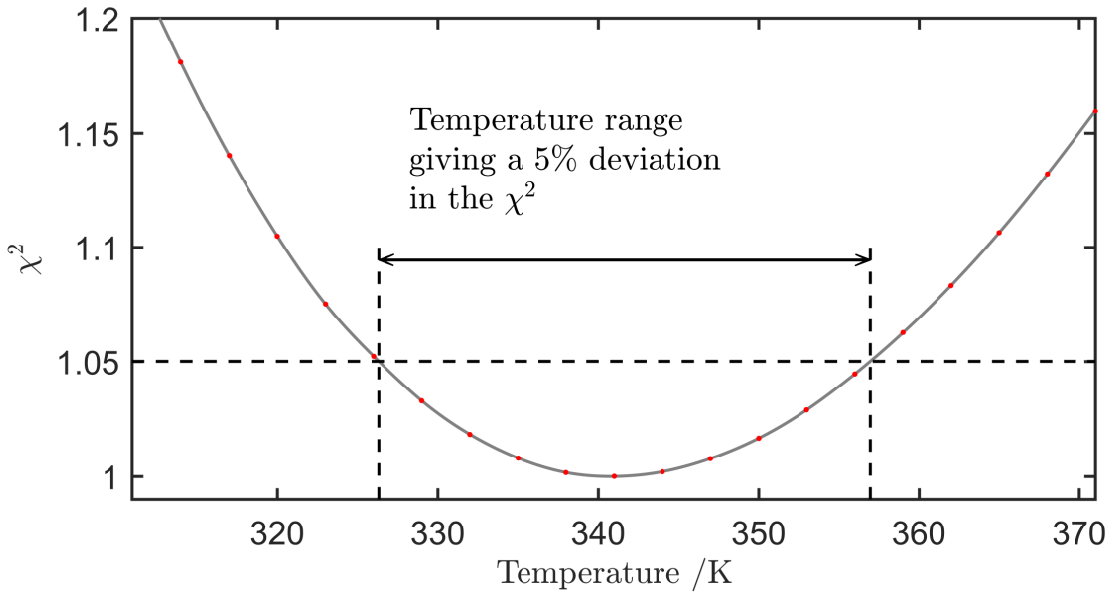

Figure 6.15: An example of the χ^2 parabola which is used to obtain a measure for the temperature sensitivity of a MUMAS spectrum. The χ^2 is determined for the comparison between each experimental spectrum and a range of modelled spectra which are at temperatures slightly either side of the temperature of each experimental spectrum. A measure of the temperature sensitivity, or the precision, is the temperature range which gives a 5% deviation from the minimum of this χ^2.

measurements, and hence better sensitivity.

In earlier work which used a laser diode operating at 760 nm, MUMAS was also used to measure the temperature of oxygen [1]. Using the same metric, the 5% deviation from the minimum of the χ^2, the precision was found to be $\pm 2\%$. This precision is better than that found for the temperature measurements of CO_2 reported in this chapter. The reason for the higher precision of temperature measurements for O_2 is that the molecular oxygen transitions exhibit a band-head in this region. Thus, in this region, molecular transitions which correspond to low J states are spectrally close to molecular transitions which correspond to high J states. As the absorption strengths of pairs of molecular transitions which correspond to both low and high J states have very different temperature dependencies, probing these pairs of transitions results in much higher

temperature sensitivity. There is no such band-head for CO_2 at 1.57 µm, which explains the poorer temperature sensitivity.

6.6.3 Temperature sensitivity enhancement

Due to the limited driving current which can be applied to the device, it is not possible to tune the laser used in this work to a significantly more temperature sensitive region. However, it may be possible to obtain a different laser which would operate in a more temperature sensitive region. Therefore, the potential improvements in temperature sensitivity are simulated for lasers operating in different spectral regions with the aim of identifying a more temperature sensitive region so that a suitable laser operating in this region could be obtained.

The standard method which was used to quantify the temperature sensitivity in section 6.6.2 was the 5% deviation from the minimum of the χ^2, where the χ^2 was determined for the comparison between each experimental spectrum and a range of modelled spectra which are at temperatures slightly either side of the temperature of each experimental spectrum. However, as experimental spectra are not available for a wide range of laser conditions, MUMAS spectra generated by different laser emission wavelengths have to be simulated. In order to aid in the computation of sensitivity measurements which follow, each of these simulated spectra has a small amount of white-noise imposed on them.*

As a χ^2 analysis was found to be a useful method to quantify the temperature sensitivity of an experimental MUMAS spectrum, this concept is adapted to obtain a

*The noise that is added is sufficiently small that it does not affect the χ^2 measurements. It is added purely for computational purposes. As mentioned previously, each of the χ^2 parabolae are normalised so that the minimum of the χ^2 is at 1. However, if no noise is added to the modelled spectrum, then due to there being a perfect fit between the modelled reference spectrum and the identical modelled spectrum which it is being compared with, the minimum of the χ^2 would be 0. Therefore it would not be possible to normalise this χ^2 measurement. The addition of a small amount to noise to the modelled reference spectrum ensures that the minimum of the χ^2 has a finite value, and hence normalisaiton is possible.

measure for the temperature sensitivity of a particular modelled MUMAS spectrum. Accordingly, the *model*-$\tilde{\chi}^2$ is defined as the χ^2 obtained when comparing a modelled reference spectrum which is at a particular temperature with a selection of modelled spectra which are at temperatures slightly either side of this temperature. Evidently, the best-fit will be when the temperature from one of the modelled spectra matches the temperature of the reference spectrum. If a small change in temperature causes an appreciable change in the MUMAS spectrum, this will manifest itself as a large change in the model-$\tilde{\chi}^2$, and thereby indicate good temperature sensitivity. Therefore, this model-$\tilde{\chi}^2$ is used as a metric for temperature sensitivity of a laser probing a particular set of molecular transitions. It is worth noting that the model-$\tilde{\chi}^2$ is indicative of how sensitive to temperature fluctuations a particular MUMAS spectrum is, and it is not affected by systematic errors which would occur in a typical experimental MUMAS spectrum.

In order to simulate the potential improvements in the temperature sensitivity of CO_2, MUMAS spectra are simulated with the laser emission spectrum translated to different spectral regions so that it coincides with different parts of this band of CO_2 transitions. The model-$\tilde{\chi}^2$ measurements are compared with similar model-$\tilde{\chi}^2$ measurements obtained for the laser used in this work (section 6.6.2). After an extensive search of nearby spectral regions, it is found that when the laser emission spectrum is shifted by 266 GHz (from 1573 nm to 1570 nm), the temperature sensitivity of the MUMAS spectrum can be increased by a factor of approximately 3.5. This is illustrated in figure 6.16 by the narrower model-$\tilde{\chi}^2$ parabola which is obtained for the simulated laser compared with that obtained for the laser used in this work. These simulations will provide guidance when purchasing another laser with the aim of improving the temperature sensitivity for a particular species.

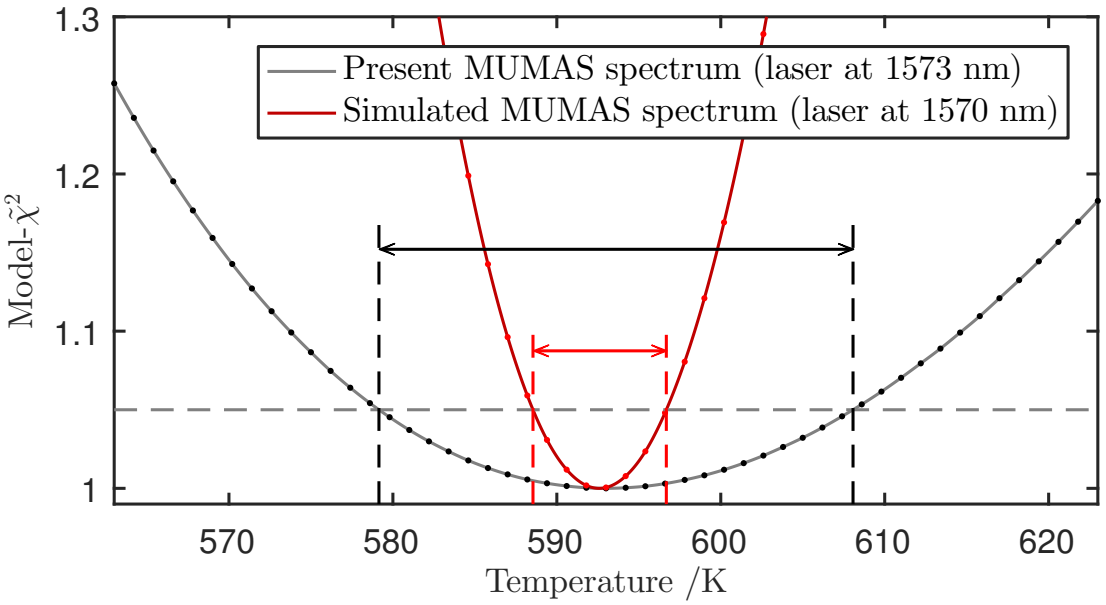

Figure 6.16: An illustration of the potential enhanced sensitivity which could be achieved by using a laser in a different spectral region of this band of CO_2 transitions. The model-$\tilde{\chi}^2$ for the MUMAS spectrum which is obtained by the laser used in this work is shown as a black line. The model-$\tilde{\chi}^2$ for the MUMAS spectrum which is obtained by the laser operating in a different spectral region is shown as a red line. The simulated laser emission spectrum is the result of shifting the laser emission spectrum of the laser used in this work by 266 GHz (from 1573 nm to 1570 nm).

6.7 Conclusion

This chapter described an alternative detection scheme, balanced ratiometric detection, which was used in this work. This new scheme has some advantages over the standard scheme. The noise characteristics of this technique are superior which improves the SNR of the experimental MUMAS spectra and consequently improves the MDL of the MUMAS technique. Furthermore, there are operational benefits of balanced ratiometric detection, including: an improvement in the dynamic range of the acquired signal, the need to record only a single channel, a flatter baseline of the signal, and the transmission spectrum of the empty gas cell no longer needing to be recorded in advance.

This chapter describes the modifications to the modelling code which take into account the variation of the laser intensity envelope as the modes are scanned in frequency. By relaxing the restriction that the mode intensity envelope must be constant, it opens up the possibility of having a much wider selection of multi-mode lasers available for performing MUMAS. Furthermore, the modelling code was developed to provide the ability to fit a MUMAS spectrum which only covers part of the intermode-spacing.

For the remainder of the work performed for this chapter, the balanced ratiometric detection scheme was used and the model incorporated data to simulate a varying mode intensity envelope. A multi-species spectrum of CO and CO_2 was obtained and the model was accurately fitted to the data. The mode-linewidth was found to be 325.13 ± 8.62 MHz. The first MUMAS spectrum obtained at atmospheric pressure using a commercially available laser was demonstrated. Finally, MUMAS spectra were obtained at a range of temperatures to demonstrate the ability to perform thermometry using MUMAS. The temperature sensitivity enhancements that would be possible with a laser in a slightly different spectral region were subsequently simulated.

Chapter 7

Conclusions

This thesis reported the work undertaken to further the development of the novel spectroscopic technique Multi-mode Absorption Spectroscopy (MUMAS). The three main aims of the work were as follows: firstly, to further understand the operation of MUMAS and subsequently improve the modelling of a MUMAS spectrum; secondly, to perform MUMAS in the mid-infrared region so as to access the strong fundamental transitions of many species found in this region and; thirdly, to identify and address the limitations of MUMAS when working towards the ultimate aim of designing and manufacturing a robust and portable gas monitoring device based on MUMAS.

In order to further understand the operation of MUMAS, the theory of tuning was considered in detail in chapter 3. This exposed inadequacies of the previous model for the tuning, the translation-model. Hence, a new model for the tuning, the expansion-model, was devised to replace it. The inadequacies of the translation-model only manifested themselves when performing MUMAS with lasers operated in the mid-infrared region and/or lasers which had many more modes than the multi-mode lasers used for MUMAS work prior to this thesis. Thus, the translation-model was sufficient for all the earlier work on MUMAS. The basis of the expansion-model is the MUMAS Equation, which

defines the position of the MUMAS absorption features, the derivation of which is given in appendix A. The expansion-model was verified by the accurate fits to the experimental MUMAS spectra throughout this thesis. Along with being more accurate, the computational modelling code for the expansion-model is also more versatile than that for the translation-model. Unlike in the computational modelling code for the translation-model, which produced the entire spectrum in one step, the expansion-model is focused around each feature in the MUMAS spectrum and therefore the properties of each feature are easily accessible. This allows property-specific modelling of selected features which helps with both the diagnosis of poorly-fitted spectra and the investigation of further advancements of the MUMAS technique, and generally aids in a more in-depth understanding of the nature of a particular MUMAS spectrum. Along with these advantages, there are also various computational-efficiency advantages of the computational modelling code for the expansion-model which allows for faster processing times.

In addition to developing a more accurate model for the scanning of the modes, the computational code was also modified to be able to incorporate data from a varying laser intensity envelope as the modes scan (chapter 6). Accordingly, the concept of the Mode Fractional Power (MFP) was introduced. Thus, by relaxing the restriction that the laser intensity envelope must be constant, it opens up the possibility of having a much wider selection of multi-mode laser sources available for performing MUMAS. Finally, the development of an efficient fitting routine based on a lookup of pre-generated MUMAS spectra, described in section 4.4.3, has greatly reduced the computational requirements for the technique in cases where many spectra produced under the same conditions need to be fitted. All these computational advancements lend themselves to developing a portable MUMAS device with on-board computation.

The first mid-infrared MUMAS spectrum obtained using an ICL was reported in

chapter 4. These ICLs were provided by the Naval Research Laboratory and are physically small with low power requirements, thus making them suitable for gas sensing applications in the field. These mid-infrared laser sources have numerous advantages over similar devices which operate at longer mid-infrared wavelengths. This range includes the region of the fundamental X-H stretch mode of many molecules including that of the C-H bond characteristic of many important hydrocarbon species. These strong molecular transitions enable higher sensitivity detection of trace species. Furthermore, these strong absorption bands typically lie closer in frequency space in the $3-4$ µm range – a feature that facilitates simultaneous detection of several species with a single, wide bandwidth, multi-mode laser source. Accordingly, a multi-species spectrum of trace amounts of methane, acetylene and formaldehyde was presented, thus demonstrating the multi-species capability of the technique. In addition, it was demonstrated that the MUMAS spectra for the constituent species of this mixture were orthogonal, thus permitting unambiguous detection of each of them. Furthermore, the MDL of the technique was investigated, and ICLs with a wider intermode-spacing were used to obtain MUMAS spectra of trace amounts of methane in atmospheric pressure, thus demonstrating the potential for highly sensitive, multi-species detection using a single multi-mode laser source.

A previously recognised limitation of MUMAS was the difficulty in sourcing a suitable multi-mode laser. The ICLs used for the work in chapter 4 were not commercially available whilst other lasers used for previous work were built in-house. However, the results of chapter 5 were obtained using a commercially available multi-mode QCL. Although these QCLs had the advantage of being commercially available, the intensity envelope of their laser spectrum was highly irregular and variable. Nonetheless, even with an irregular and spectrally structured multi-mode envelope, which also varied during the spectral scanning, all the features of experimentally recorded MUMAS spectra were modelled with sufficient accuracy to achieve good fits to the data. Therefore, potential

users are no longer required to construct custom lasers or use relatively complex DFG systems, thus facilitating more widespread use of MUMAS.

The QCL used for the work in chapter 4 extended the spectral range over which MUMAS has been demonstrated. MUMAS spectra of NO were obtained with a QCL operating at 5.3 µm. Extension of laser-based methods to this region has the advantage of exploiting the strong absorption lines found here, hence increasing the number of molecular species that can be detected by using this technique. In addition to detecting NO, transitions of H_2O were simultaneously recorded from the presence of laboratory air containing water vapour. These data illustrate the potential for MUMAS to distinguish background 'interference' from water, or other species, since additional information on the target species being detected is provided at locations where overlapping of absorption lines is less severe or absent. This is a particularly advantageous property of MUMAS as H_2O is a common interfering species in many environments. Finally, it was demonstrated that MUMAS data can be obtained at fast scan rates (10 kHz), thus enabling gas sensing with short measurement times, which is important for applications in rapidly changing environments or for active process control.

A key advancement was the development of a balanced ratiometric detection scheme in chapter 6, which also aids portability. This new scheme has advantages over the standard scheme. The superior noise characteristics of this technique improves the SNR of the experimental MUMAS spectra and consequently improves the MDL of the MUMAS technique. Furthermore, there are operational benefits of balanced ratiometric detection: the dynamic range of the acquired signal is improved, only a single channel needs to be recorded, the baseline of the signal is flatter and there is no need for the transmission spectrum of the empty gas cell to be recorded in advance. Being both small and robust, coupled with these operational benefits, greatly simplifies the technique and should subsequently simplify the engineering of a portable, robust device. Using this new

scheme with a commercially available diode laser operating at 1.57 µm, MUMAS spectra were obtained at a range of temperatures, thus demonstrating the ability to perform thermometry using MUMAS.

This work has demonstrated that MUMAS has the potential to be a useful addition to the range of optical gas sensing techniques which are currently available. It is a simple technique which is able to measure both multiple parameters and multiple species using a single laser source and single detection scheme. Many of the limitations of the technique were addressed during the course of the work in this thesis, and therefore it is adequately placed to be developed into a portable gas sensing device. Beyond the work in this thesis, there are a wealth of potential options to explore for the further development of MUMAS, a few of which are outlined in chapter 8.

Chapter 8

Future work

MUMAS has been developed to a stage where it is versatile, powerful and has the potential to be developed into a gas monitoring device. There are a range of directions in which the project can be taken. This chapter discusses suggested further developments of the MUMAS technique.

The next logical step in the development of MUMAS for its use in a widely deployed gas sensor is to engineer such a device for portability, robustness and low cost. A number of potential applications which are on the horizon are discussed in section 8.1. The extension of MUMAS to the mid-infrared region using ICLs was demonstrated in chapter 4, and due to the superior performance of the balanced ratiometric detection scheme, the adaption of this scheme to the mid-infrared region is discussed in section 8.2. Using MUMAS with a multi-heterodyne configuration is outlined in section 8.3 in order to overcome the potential over-congestion of features common to many MUMAS spectra. Finally, an experiment is proposed in section 8.4 to make use of the potential fast scan rates of MUMAS in order to probe the dynamics of non-equilibrium states of molecules which have been excited by a pump laser.

8.1 Portable MUMAS device

The ultimate aim of MUMAS is to develop the technique so that it can be readily deployed in a portable gas monitoring device, whilst delivering on the desirable properties of an ideal gas monitoring instrument. The main components of a portable system have been independently developed over the course of the work in this thesis.

As outlined in chapter 2, a gas monitoring device would ideally have the following properties: be small, robust and non-invasive; have low fabrication costs; have high resolution; operate over a broad bandwidth so as to target multiple species with the same device; have high-selectivity; have reasonable output power yet have low power requirements; have a fast time-response and have high immunity from vibrations, temperature fluctuations and other noise sources. The majority of these requirements are dependent upon the laser properties, and the advent of ICLs has provided a MUMAS laser source which meets many of them. ICLs are small, robust devices, which operate at room temperature and also have high immunity from vibrations, temperature fluctuations and other noise sources. They have inherently low power requirements, yet their output power is sufficient for MUMAS. Therefore, they lend themselves to being integrated into a portable and robust device. Furthermore, they provide a broad bandwidth of radiation, and this coupled with their narrow mode-linewidth means that they can be used to produce high-resolution spectra of multiple species, simultaneously. Being a spectroscopic technique, it is also inherently non-invasive and has high selectivity. At present, the cost and availability of suitable ICL devices and detectors is the main limitation to wide deployment. However, ICLs are becoming more commercially available. Additionally, the fabrication of ICL devices is priced per manufacturing run and the number produced each time can be scaled up thereby decreasing the unit cost.

The balanced ratiometric detection scheme demonstrated in chapter 6 would also help

facilitate a portable device. This detection circuit is small and robust. The noise properties are a significant improvement over those for the standard detection scheme. Furthermore, the operational benefits, outlined in section 6.3, greatly simplify the technique and should subsequently simplify the engineering of a portable, robust device.

The modelling code has been significantly improved to accurately model the scanning of the individual modes and to account for the varying mode intensity envelope as the modes are scanned across the intermode-spacing, thereby relaxing the need to have a constant mode intensity envelope. By relaxing this restriction, it has opened up the possibility of having a much wider selection of multi-mode lasers available for performing MUMAS. In addition, the development of an efficient fitting routine based on a lookup of pre-generated MUMAS spectra, described in section 4.4.3, has greatly reduced the computational requirements for the technique. These computational advancements facilitate the development of a portable MUMAS device with on-board computation. The combination of a small and robust laser source and detection scheme along with the computational advancements of the technique are the main components of a portable MUMAS device. Thus, further development should be directed into engineering and building a complete MUMAS device with a particular focus on miniaturisation and portability.

With a portable MUMAS device, the potential gas sensing applications outlined in section 2.2 could be directly targeted. There are a diverse and abundant range of situations where the technique could be used, and a few are briefly mentioned below. For example, the portable nature of the device would enable atmospheric measurements of certain species in order to monitor the air quality in cities. The concentrations of various gases in engine exhausts could be measured using the multi-species capability. The high sensitivity to hydrocarbons in the $3 - 4$ µm range would enable both process control and safety monitoring in various industrial environments. The high-scan rates that are

possible, coupled with the detection of multiple molecular transitions could be used to monitor, understand and control the dynamics of plasmas.

8.2 Mid-infrared balanced ratiometric detection scheme

An alternative detection scheme, balanced ratiometric detection, was demonstrated in chapter 6. This particular device was built using photodiodes which were able to detect in the range $800 - 1700$ nm.

The improvements in the noise characteristics and the operational advantages of the balanced ratiometric detection scheme would be equally as beneficial to the MUMAS work performed in the mid-infrared region. However, the circuit used for the near-infrared balanced ratiometric detection device was designed to work with particular photodiodes. The mid-infrared photovoltaic detectors used in this work had different operating characteristics to these photodiodes and therefore the circuit will require suitable modifications to incorporate these photovoltaic detectors.

Given the superior performance of such a detection scheme and the potential sensitivity improvements in particular, it is suggested that a balanced ratiometric detection scheme that works with photovoltaic detectors in the mid-infrared region is developed.

8.3 Multi-heterodyne MUMAS

When performing spectroscopy with a multi-mode laser, the intensity of the radiation which passes through the sample is a superposition of the intensity of each individual mode. Therefore, when there is an absorption, it is difficult to determine which mode is being absorbed. Consequently, without a spectrometer to selectively the monitor the intensity of particular modes, the specific mode involved in the absorption feature is unknown.

This has implications for MUMAS. MUMAS requires extensive modelling to extract the spectral information encoded in the transmitted intensity, and to determine which modes are being absorbed. Even with this modelling, MUMAS spectra can suffer from congestion of spectral features as absorption features from many modes can occur at the same location in the scan. This issue is exacerbated when there are multiple species.

One promising solution is to use a heterodyne technique with two ICLs, with each ICL having a slightly different intermode-spacing. This method has been demonstrated for other, similar techniques, as mentioned in section 2.6.6. By down-converting the ICL spectrum of one of the ICLs using an optical multi-heterodyne process with the other ICL used as the local oscillator, the transmitted intensity of each individual mode can be observed. If the intermode-spacings are tuned correctly, the heterodyne signal will be in the RF spectral region. As the intermode-spacings of the two ICLs would be slightly different, the frequency separation between each pair of proximal interacting modes would also be slightly different. Thus, each pair of proximal interacting modes would produce a heterodyne signal in a slightly different region of the RF spectrum, and therefore the transmission spectra, which are currently superposed in a single MUMAS spectrum, would be separated and equally spaced in the RF spectrum. The lasers used for the multi-heterodyne techniques described in section 2.6.6 were kept at a constant position in frequency, and hence the sampling resolution of this technique was given by the intermode-spacing of the probing laser. The heterodyne technique could be extended by scanning the modes of the ICLs, and subsequently using a modified MUMAS modelling code to analyse the resulting RF spectrum. This would make obtaining MUMAS spectra at atmospheric pressures more likely as the spectra would be less susceptible to becoming featureless through pressure broadening.

Using multi-heterodyne spectroscopy in combination with MUMAS presents a possible solution to obtaining MUMAS spectra at atmospheric pressures. However, it comes

with additional complexity and cost, and requires stable, phase-locked lasers and fast detectors. Furthermore, the upper bound on the bandwidth of the fast detectors will directly impact the spectral coverage that is possible.

8.4 Measurement of relaxation dynamics in excited species

In section 5.7, MUMAS was demonstrated with a scan rate of 10 kHz. The laser used in these studies was capable of being scanned at significantly faster rates. However, the modulation amplitude of the scan was found to decrease at faster scan rates owing to limitations imposed by the drive electronics available. Despite this, these results demonstrated the potential for gas sensing with fast response times. Electronic laser drivers with a higher bandwidth would allow an increase in scan rates with a subsequent decrease in measurement times.

With a scan rate of 10 kHz, each spectrum is acquired over a time period of 50 µs. Therefore, the maximum time delay between the measurement of two particular MUMAS features in a MUMAS spectrum is 50 µs. With the width of each MUMAS feature being approximately 2% of a MUMAS spectrum, it takes approximately 1 µs to probe each molecular transition. Faster scans rates decrease the probe duration of a MUMAS feature.

These fast scan rates enable the measurement of rapidly changing molecular concentrations. In addition, due to the multiple interacting modes in MUMAS, many molecular transitions can be probed in a pre-determined time sequence (maximum time delay of 50 µs). By varying the time at which the modes begin to scan relative to when the molecules have been excited, the time sequence at which particular transitions are probed can be shifted, thereby providing the ability to further improve the temporal resolution.

The fast scan rates achievable with MUMAS opens up the possibility of rapidly

monitoring the dynamic behaviour of the populations of energy levels in non-equilibrium systems. In one such experiment, a pulse from a pump laser could be used to excite a sample of a species, thereby enabling the subsequent transient behaviour of the energy level populations to be studied. This would aid in the understanding of chemical reaction dynamics and relaxation to equilibrium.

Appendix A

Derivation of the MUMAS equation

The following is a derivation of the MUMAS equation. The MUMAS equation describes the frequency position of all the MUMAS absorption features in a MUMAS spectrum. It is the fundamental building block of the computational modelling code for the expansion-model, in which the position of all the MUMAS absorption features are prospectively determined before their magnitudes or lineshapes are calculated.

For a laser mode with a mode index of q, the frequency of the mode, $\nu_q(\mathrm{t})$, is given by equation A.1, where $L(t)$ is the optical length of the cavity. This optical length accounts for changes in both the physical length of the cavity and the refractive index of the cavity. The time dependence of the length of the cavity, and hence of the frequency of the mode, are determined by the rate at which the laser scans.

$$\nu_q(\mathrm{t}) = \frac{qc}{2L(t)}\,. \tag{A.1}$$

The wavelength, $\lambda_q(\mathrm{t})$, of this mode is given by equation A.2.

$$\lambda_q(\mathrm{t}) = \frac{2L(t)}{q}\,. \tag{A.2}$$

The optical length of the cavity changes linearly with time (equation A.3), where L_0 is the initial optical length of the cavity and ϕ is a measure of the rate at which the optical length of the cavity changes.

$$L(t) = L_0 - \phi t\,. \tag{A.3}$$

The initial intermode-spacing, Δm_0, is given by equation A.4.

$$\Delta m_0 = \frac{c}{2L_0}\,. \tag{A.4}$$

Thus, the initial central wavelength, λ_c, is given by equation A.5, where ν_c and q_c are the frequency and mode index of the central mode, respectively.

$$\lambda_c = \frac{c}{\nu_c} = \frac{c}{q_c \Delta m_0}\,. \tag{A.5}$$

In order to keep this derivation general, the variable $s = \pm 1$ is introduced to define whether the modes scan in a positive or negative direction in frequency. Two conditions are used to find expressions for L_0 and ϕ:

1. The wavelength of the central mode is λ_c when $t = 0$. Thus, for q_c and $t = 0$, $\lambda(0) = \lambda_c$. Alternatively, for $q = q_c$ and $t = 0$, $\nu(0) = \nu_c = q_c \Delta m_0$.

2. t_x is the time taken for the central mode to scan from ν_c to $\nu_c + sx\Delta m_0$, where x defines a fraction of the intermode-spacing.

The first condition results in an expression for L_0, which is given by equation A.6.

$$L_0 = \frac{q_c \lambda_c}{2} \,. \tag{A.6}$$

Substituting this expression into equation A.2 gives equation A.7.

$$\begin{aligned} \lambda_q(\mathrm{t}) &= \frac{2}{q}\left(\frac{q_c\lambda_c}{2} - \phi t\right) \\ &= \frac{q_c}{q}\lambda_c - \frac{2\phi}{q}t \,. \end{aligned} \tag{A.7}$$

The second condition results in an expression for ϕ, which is given by equation A.8.

$$\frac{-2\phi}{q} = \frac{q_c}{q}\frac{1}{t_x}\left(\frac{-\lambda_c s x}{q_c + sx}\right) \,. \tag{A.8}$$

Substituting this expression into equation A.7 gives equation A.9.

$$\begin{aligned} \lambda_q(\mathrm{t}) &= \frac{q_c}{q}\lambda_c + \frac{q_c}{q}\frac{t}{t_x}\left(\frac{-\lambda_c s x}{q_c + sx}\right) \\ &= \frac{q_c}{q}\lambda_c\left(1 - \frac{t}{t_x}\left(\frac{sx}{q_c + sx}\right)\right) \,. \end{aligned} \tag{A.9}$$

Differentiating equation A.9 gives equation A.10, which is the rate of change of wavelength of the modes.

$$\dot{\lambda_c}(\mathrm{t}) = -\lambda_c \frac{1}{t_x}\left(\frac{sx}{q_c + sx}\right) \,. \tag{A.10}$$

Substituting $\dot{\lambda_c}(\mathrm{t})$ back into equation A.9 gives equation A.11.

$$\lambda_q(\mathrm{t}) = \frac{q_c}{q}\left(\lambda_c - \dot{\lambda_c} t\right) \,. \tag{A.11}$$

To determine the frequency positions at which the MUMAS absorption features appear on a MUMAS spectrum, the absolute frequency positions of the molecular transitions

must be obtained from a spectroscopic database. The absolute wavelength position of a gas transition with index j is denoted as W_j. There will be a MUMAS absorption feature when a particular mode with mode index q is resonant with the frequency of a molecular transition. Thus, the wavelength position of a MUMAS feature, $F^{\lambda}_{q,j} = \dot{\lambda_c} t$, is given by equation A.12. The superscript λ in $F^{\lambda}_{q,j}$ indicates that this is a wavelength position, rather than a frequency position.

$$F^{\lambda}_{q,j} = \frac{q_c}{q} W_j - \lambda_c \,. \tag{A.12}$$

The frequency positions of the MUMAS absorption features on a MUMAS spectrum, $F_{q,j}$, are given by equation A.13, where the absolute frequency positions of the gas transitions are denoted by T_j. This is the *MUMAS equation*.

$$F_{q,j} = \frac{q}{q_c} T_j - \nu_c \,. \tag{A.13}$$

For computational modelling purposes, it is important to define the range of frequencies of potential MUMAS absorption features to be considered when simulating a MUMAS spectrum. In order to do this, MUMAS frequency boundaries are defined which depend on the required number of repeat-units in the simulated MUMAS spectrum. The length of one repeat-unit is equivalent to the initial value for the intermode-spacing, Δm_0. For N repeat-units, the boundaries are defined by equation A.14.

$$x = \pm \frac{N}{2} \,. \tag{A.14}$$

The boundaries, in absolute wavelength, are subsequently given by equation A.15. This is the equation which is used to define the boundaries between which molecular

transitions from the spectroscopic database are considered.

$$F_{bounds} = \dot{\lambda_c} t_{\pm\frac{N}{2}} = \frac{\mp\lambda_c \frac{N}{2} s}{q_c \pm \frac{N}{2} s} = \frac{\mp\lambda_c N s}{2q_c \pm N s} \,. \tag{A.15}$$

Appendix B

Approximation of Voigt profiles

Spectral lineshapes for each molecular transition are a combination of Lorentzian and Gaussian profiles, and are modelled as Voigt profiles. These can be calculated through the numerical convolution of Lorentzian and Gaussian profiles. However, these line profiles can be generated much more efficiently, and without significant error, through the use of an empirical Voigt approximation.

The approximation chosen for the work in this thesis was first published by Whiting in 1968 [123] and developed by Olivero and Longbothum in 1977 [124]. It is reported in Brassington [34] in the form given in equation B.1, where $x = \gamma_L/\gamma_V$, and $y = |\nu - \nu_0|/\gamma_V$. γ_V is the Voigt profile half-width at half maximum (HWHM) given approximately by equation B.2, and $\sigma_V(\nu_0)$ is the cross-section at the line centre which is given by equation B.3.

$$\begin{aligned}\sigma_\nu(\nu) = \sigma_\nu(\nu_0)\big\{&(1-x)\exp(-0.693y^2) + x/(1+y^2) \\ &+0.016(1-x)x[\exp(0.0841y^{2.25}) - 1/(1+0.210y^{2.25})]\big\}\ .\end{aligned} \tag{B.1}$$

$$\gamma_V = 0.5346\gamma_L + (0.2166\gamma_L^2 + \gamma_D^2)^{\frac{1}{2}} \,. \tag{B.2}$$

$$\sigma_V\,(\nu_0) = S/[2\gamma_V(1.065 + 0.447x + 0.058x^2)] \,. \tag{B.3}$$

Bibliography

[1] Y. Arita and P. Ewart. 'Multi-mode absorption spectroscopy'. *Optics Communications* 281.9 (May 2008), pp. 2561–2566. DOI: 10.1016/j.optcom.2007.12.096.

[2] Y. Arita and P. Ewart. 'Infra-red multi-mode absorption spectroscopy of acetylene using an Er/Yb:glass micro-laser'. *Optics Express* 16.7 (Mar. 2008), p. 4437. DOI: 10.1364/OE.16.004437.

[3] Y. Arita, R. Stevens and P. Ewart. 'Multi-mode absorption spectroscopy of oxygen for measurement of concentration, temperature and pressure'. *Applied Physics B* 90.2 (Jan. 2008), pp. 205–211. DOI: 10.1007/s00340-007-2917-y.

[4] M. L. Hamilton, G. A. D. Ritchie, Y. Arita and P. Ewart. 'Multi-mode absorption spectroscopy, MUMAS, using wavelength modulation and cavity enhancement techniques'. *Applied Physics B* 100.3 (May 2010), pp. 665–673. DOI: 10.1007/s00340-010-4040-8.

[5] J. H. Northern, A. Thompson, M. L. Hamilton and P. Ewart. 'Multi-species detection using multi-mode absorption spectroscopy (MUMAS)'. *Applied Physics B* 111.4 (Mar. 2013), pp. 627–635. DOI: 10.1007/s00340-013-5382-9.

[6] A. Thompson, J. H. Northern, B. Williams, M. L. Hamilton and P. Ewart. 'Simultaneous detection of CO$_2$ and CO in engine exhaust using multi-mode

absorption spectroscopy, MUMAS'. *Sensors and Actuators B: Chemical* 198 (July 2014), pp. 309–315. DOI: 10.1016/j.snb.2014.03.060.

[7] J. H. Northern, S. O'Hagan, M. L. Hamilton and P. Ewart. 'Mid-infrared multi-mode absorption spectroscopy, MUMAS, using difference frequency generation'. *Applied Physics B* (Dec. 2014). DOI: 10.1007/s00340-014-5989-5.

[8] J. H. Northern, S. O'Hagan, B. Fletcher, B. Gras, P. Ewart, C. S. Kim, M. Kim, C. D. Merritt, W. W. Bewley, C. L. Canedy, J. Abell, I. Vurgaftman and J. R. Meyer. 'Mid-infrared multi-mode absorption spectroscopy using interband cascade lasers for multi-species sensing'. *Optics letters* 40.17 (2015), pp. 4186–4189.

[9] S. O'Hagan, J. H. Northern, B. Gras, P. Ewart, C. S. Kim, M. Kim, C. D. Merritt, W. W. Bewley, C. L. Canedy, I. Vurgaftman and J. R. Meyer. 'Multi-species sensing using multi-mode absorption spectroscopy with mid-infrared interband cascade lasers'. *Applied Physics B* 122.6 (2016), p. 173. DOI: 10.1007/s00340-016-6377-0.

[10] S. O'Hagan, T. Pinto, P. Ewart and G. A. D. Ritchie. 'Multi-mode absorption spectroscopy using a quantum cascade laser for simultaneous detection of NO and H2O'. *Applied Physics B* 122.8 (2016), p. 226. DOI: 10.1007/s00340-016-6499-4.

[11] P. Werle. 'A review of recent advances in semiconductor laser based gas monitors'. *Spectrochimica Acta Part A: Molecular and Biomolecular Spectroscopy* 54.2 (1998), pp. 197–236.

[12] J. Hodgkinson and R. P. Tatam. 'Optical gas sensing: a review'. *Measurement Science and Technology* 24.1 (Jan. 2013), p. 012004. DOI: 10.1088/0957-0233/24/1/012004.

[13] P. H. Saldiva, A. J. Lichtenfels, P. S. Paiva, I. A. Barone, M. A. Martins, E. Massad, J. C. Pereira, V. P. Xavier, J. M. Singer and G. M. Böhm. 'Association between air pollution and mortality due to respiratory diseases in children in

São Paulo, Brazil: a preliminary report'. *Environmental research* 65.2 (1994), pp. 218–25. DOI: 10.1006/enrs.1994.1033.

[14] M. Bobak. 'Outdoor air pollution, low birth weight, and prematurity'. *Environmental health perspectives* 108.2 (2000), pp. 173–6. DOI: 10.2307/3454517.

[15] I. Linnerud, P. Kaspersen and T. Jæger. 'Gas monitoring in the process industry using diode laser spectroscopy'. *Applied Physics B* 67.3 (1998), pp. 297–305. DOI: 10.1007/s003400050509.

[16] IPCC. *Climate Change 2014: Synthesis Report. Contribution of Working Groups I, II and III to the Fifth Assessment Report of the Intergovernmental Panel on Climate Change*. 2014, p. 151. DOI: 10.1017/CBO9781107415324.004.

[17] R. P. Wayne. *Chemistry of Atmospheres: An Introduction to the Chemistry of the Atmospheres of Earth, the Planets, and their Satellites*. Oxford University Press, 2000.

[18] H. I. Schiff, G. I. Mackay and J. Bechara. 'The use of tunable diode laser absorption spectroscopy for atmospheric measurements'. *Research on Chemical Intermediates* 20.3 (1994), pp. 525–556. DOI: 10.1163/156856794X00441.

[19] USEPA Office of Air and Radiation. *The Benefits and Costs of the Clean Air Act: 1990 to 2020*. Tech. rep. April. 2010, pp. 5–23.

[20] WHO. 'Health risks of particulate matter from long-range transboundary air pollution'. *Pollution Atmospherique* 190 (2006), p. 169. DOI: ISBN9789289042895.

[21] H. Bovensmann, M. Buchwitz, J. P. Burrows, M. Reuter, T. Krings, K. Gerilowski, O. Schneising, J. Heymann, A. Tretner and J. Erzinger. 'A remote sensing technique for global monitoring of power plant CO2 emissions from space and related

applications'. *Atmospheric Measurement Techniques* 3.4 (2010), pp. 781–811. DOI: 10.5194/amt-3-781-2010.

[22] W. Cao and Y. Duan. 'Current status of methods and techniques for breath analysis'. *Critical Reviews in Analytical Chemistry* 37.1 (Apr. 2007), pp. 3–13. DOI: 10.1080/10408340600976499.

[23] F. K. Tittel. 'Current status of mid-infrared quantum and interband cascade lasers for clinical breath analysis'. *Optical Engineering* 49.11 (Nov. 2010), p. 111123. DOI: 10.1117/1.3498768.

[24] W. Miekisch, J. K. Schubert and G. F. Noeldge-Schomburg. 'Diagnostic potential of breath analysis - focus on volatile organic compounds'. *Clinica Chimica Acta* 347 (2004), pp. 25–39. DOI: 10.1016/j.cccn.2004.04.023.

[25] J. M. Sanchez and R. D. Sacks. 'GC analysis of human breath with a series-coupled column ensemble and a multibed sorption trap'. *Analytical Chemistry* 75.10 (2003), pp. 2231–2236. DOI: 10.1021/ac020725g.

[26] L. Ciaffoni, D. P. O. Neill, J. H. Couper, G. A. D. Ritchie, G. Hancock and P. a. Robbins. 'In-airway molecular flow sensing: a new technology for continuous, non-invasive monitoring of oxygen consumption in critical care'. *Sci. Adv* Aug. (2016), pp. 1–10. DOI: 10.1126/sciadv.1600560.

[27] X. Liu, S. Cheng, H. Liu, S. Hu, D. Zhang and H. Ning. 'A survey on gas sensing technology'. *Sensors* 12.7 (2012), pp. 9635–9665. DOI: 10.3390/s120709635.

[28] C. R. Arkin, T. P. Griffin, A. K. Ottens, J. A. Diaz, D. W. Follistein, F. W. Adams and W. R. Helms. 'Evaluation of small mass spectrometer systems for permanent gas analysis'. *Journal of the American Society for Mass Spectrometry* 13.8 (2002), pp. 1004–1012. DOI: 10.1016/S1044-0305(02)00422-1.

[29] N. Yamazoe, G. Sakai and K. Shimanoe. 'Oxide semiconductor gas sensors'. *Catalysis Surveys from Asia* 7.1 (2003), pp. 63–75. DOI: 10.1023/A:1023436725457.

[30] H. Teichert, T. Fernholz and V. Ebert. 'Simultaneous in situ measurement of CO, H2O, and gas temperatures in a full-sized coal-fired power plant by near-infrared diode lasers'. *Applied optics* 42.12 (2003), pp. 2043–51. DOI: 10.1364/AO.42.002043.

[31] X. Chao, J. B. Jeffries and R. K. Hanson. 'Real-time, in situ, continuous monitoring of CO in a pulverized-coal-fired power plant with a 2.3 μm laser absorption sensor'. *Applied Physics B: Lasers and Optics* 110.3 (2013), pp. 359–365. DOI: 10.1007/s00340-012-5262-8.

[32] B. Cummings, M. L. Hamilton, L. Ciaffoni, T. R. Pragnell, R. Peverall, G. A. D. Ritchie, G. Hancock and P. A. Robbins. 'Laser-based absorption spectroscopy as a technique for rapid in-line analysis of respired gas concentrations of O2 and CO2'. *Journal of applied physiology* 111.1 (2011), pp. 303–7. DOI: 10.1152/japplphysiol.00119.2011.

[33] B. Buchholz, A. Afchine and V. Ebert. 'Rapid, optical measurement of the atmospheric pressure on a fast research aircraft using open-path TDLAS'. *Atmospheric Measurement Techniques* 7.11 (2014), pp. 3653–3666. DOI: 10.5194/amt-7-3653-2014.

[34] D. J. Brassington. 'Tunable diode laser absorption spectroscopy for the measurement of atmospheric species'. In: *Spectroscopy in Environmental Science*. 1995. Chap. 3.

[35] J. Hollas. *High resolution spectroscopy*. 2nd. John Wiley and Sons, 1998, p. 743.

[36] W. Demtröder. *Laser Spectroscopy: 1*. Springer Berlin Heidelberg, 2008.

[37] W. Heisenberg. 'The actual content of quantum theoretical kinematics and mechanics'. *Zeitschrift für Physik* 43.3-4 (1927), pp. 172–198. DOI: 10.1119/1.1991172.

[38] S. Hooker and C. Webb. *Laser Physics (Oxford Master Series in Physics)*. Oxford University Press, 2010.

[39] C. Wieman and T. W. Hänsch. 'Doppler-free laser polarization spectroscopy'. *Physical Review Letters* 36.20 (1976), pp. 1170–1173. DOI: 10.1103/PhysRevLett.36.1170.

[40] H. J. W. Muller-Kirsten. *Basics of Statistical Physics (Second Edition)*. World Scientific Publishing Company, 2013. Chap. 2.

[41] O. Svelto. *Principles of Lasers*. Springer, 2009, p. 644.

[42] T. H. Maiman. 'Stimulated optical radiation in Ruby'. *Nature* 187.4736 (Aug. 1960), pp. 493–494. DOI: 10.1038/187493a0.

[43] R. N. Hall, G. E. Fenner, J. D. Kingsley, T. J. Soltys and R. O. Carlson. 'Coherent light emission from GaAs junctions'. *Physical Review Letters* 9.9 (1962), pp. 366–368. DOI: 10.1103/PhysRevLett.9.366.

[44] G. Gould. 'The LASER, Light Amplification by Stimulated Emission of Radiation'. In: *The Ann Arbor Conference on Optical Pumping: June 15 Through June 18, 1959*. 1959.

[45] M. G. Allen. 'Diode laser absorption sensors for gas-dynamic and combustion flows'. *Measurement science & technology* 9 (1998), pp. 545–562. DOI: 10.1088/0957-0233/9/4/001.

[46] K. Petermann. *Laser Diode Modulation and Noise (Advances in Opto-Electronics)*. Springer, 1991.

[47] F. K. Tittel, D. Richter and A. Fried. 'Mid-infrared laser applications in spectroscopy'. In: *Solid-State Mid-Infrared Laser Sources*. Vol. 516. 7. 2003, pp. 458–529. DOI: 10.1007/3-540-36491-9_11.

[48] K. Krzempek, R. Lewicki, L. Nähle, M. Fischer, J. Koeth, S. Belahsene, Y. Rouillard, L. Worschech and F. K. Tittel. 'Continuous wave, distributed feedback diode laser based sensor for trace-gas detection of ethane'. *Applied Physics B: Lasers and Optics* 106.2 (2012), pp. 251–255. DOI: 10.1007/s00340-011-4857-9.

[49] P. Werle, F. Slemr, K. Maurer, R. Kormann, R. Mücke and B. Jänker. 'Near- and mid-infrared laser-optical sensors for gas analysis'. *Optics and Lasers in Engineering* 37.2-3 (2002), pp. 101–114. DOI: 10.1016/S0143-8166(01)00092-6.

[50] G. B. Rieker. 'Wavelength-modulation spectroscopy for measurements of gas temperature and concentration in harsh environments'. PhD thesis. 2009.

[51] K. Duffin, A. J. McGettrick, W. Johnstone, G. Stewart and D. G. Moodie. 'Tunable diode-laser spectroscopy with wavelength modulation: a calibration-free approach to the recovery of absolute gas absorption line shapes'. *Journal of Lightwave Technology* 25.10 (2007), pp. 3114–3125. DOI: 10.1109/JLT.2007.904937.

[52] M. Mazurenka, A. J. Orr-Ewing, R. Peverall and G. A. D. Ritchie. 'Cavity ring-down and cavity enhanced spectroscopy using diode lasers'. *Annual Reports Section "C" (Physical Chemistry)* 101 (2005), p. 100. DOI: 10.1039/b408909j.

[53] J. Morville, S. Kassi, M. Chenevier and D. Romanini. 'Fast, low-noise, mode-by-mode, cavity-enhanced absorption spectroscopy by diode-laser self-locking'. *Applied Physics B: Lasers and Optics* 80.8 (2005), pp. 1027–1038. DOI: 10.1007/s00340-005-1828-z.

[54] K. M. Manfred, G. A. D. Ritchie, N. Lang, J. Röpcke and J. H. Van Helden. 'Optical feedback cavity-enhanced absorption spectroscopy with a 3.24 μm interband

cascade laser'. *Applied Physics Letters* 106.22 (2015), pp. 2–6. DOI: 10.1063/1.4922149.

[55] D. Romanini. *Cavity-Enhanced Spectroscopy and Sensing*. Vol. 179. 2014, p. 60. DOI: 10.1007/978-3-642-40003-2.

[56] Y. He, R. Kan, F. V. Englich, W. Liu and A. J. Orr-Ewing. 'Simultaneous multi-laser, multi-species trace-level sensing of gas mixtures by rapidly swept continuous-wave cavity-ringdown spectroscopy.' *Optics express* 18.19 (2010), pp. 20059–20071. DOI: 10.1364/OE.18.020059.

[57] P. A. Martin. 'Near-infrared diode laser spectroscopy in chemical process and environmental air monitoring'. *Chemical Society Reviews* 31 (2002), pp. 201–210. DOI: 10.1039/b003936p.

[58] N. Docquier and S. Candel. 'Combustion control and sensors: a review'. *Progress in Energy and Combustion Science* 28.2 (2002), pp. 107–150. DOI: 10.1016/S0360-1285(01)00009-0.

[59] G. Gao, B. Chen and T. Cai. 'Simultaneous detection of CO and CO2 at elevated temperatures using tunable diode laser absorption spectroscopy near 1570 nm'. *Optics and Spectroscopy* 114.3 (2013), pp. 340–346. DOI: 10.1134/S0030400X13030120.

[60] B. L. Upschulte, D. M. Sonnenfroh and M. G. Allen. 'Measurements of CO, CO2, OH, and H2O in room-temperature and combustion gases by use of a broadly current-tuned multisection InGaAsP diode laser'. *Applied Optics* 38.9 (1999), pp. 1506–1512. DOI: 10.1364/AO.38.001506.

[61] R. K. Hanson. 'Applications of quantitative laser sensors to kinetics, propulsion and practical energy systems'. *Proceedings of the Combustion Institute* 33.1 (2011), pp. 1–40. DOI: 10.1016/j.proci.2010.09.007.

[62] Y. Gérard, R. J. Holdsworth and P. A. Martin. 'Multispecies in situ monitoring of a static internal combustion engine by near-infrared diode laser sensors'. *Applied Optics* 46.19 (2007), pp. 3937–3945. DOI: 10.1364/AO.46.003937.

[63] K. Kohse-Höinghaus, R. S. Barlow, M. Aldén and J. Wolfrum. 'Combustion at the focus: laser diagnostics and control'. *Proceedings of the Combustion Institute* 30.1 (Jan. 2005), pp. 89–123. DOI: 10.1016/j.proci.2004.08.274.

[64] D. S. Baer and R. K. Hanson. 'Multiplexed diode-laser sensor system for simultaneous H2O, O2, and temperature measurements'. *Optics letters* 19.22 (1994), pp. 1900–1902. DOI: 10.1364/OL.19.001900.

[65] D. B. Oh, M. E. Paige and D. S. Bomse. 'Frequency modulation multiplexing for simultaneous detection of multiple gases by use of wavelength modulation spectroscopy with diode lasers'. *Applied optics* 37.12 (Apr. 1998), pp. 2499–501.

[66] A. S. Arnold, J. S. Wilson and M. G. Boshier. 'A simple extended-cavity diode laser'. *Review of Scientific Instruments* 69.3 (1998), p. 1236. DOI: 10.1063/1.1148756.

[67] F. Duarte. *Tunable Laser Optics*. Butterworth-Heinemann, 2003.

[68] P. Heim, Z. Fan, S.-H. Cho, K. Nam, M. Dagenais, F. Johnson and R. Leavitt. 'Single-angled-facet laser diode for widely tunable external cavity semiconductor lasers with high spectral purity'. *Electronics Letters* 33.16 (1997), p. 1387. DOI: 10.1049/el:19970911.

[69] S. T. Sanders, D. W. Mattison, J. B. Jeffries and R. K. Hanson. 'Sensors for high-pressure, harsh combustion environments using wavelength-agile diode lasers'. *Proceedings of the Combustion Institute* 29.2 (2002), pp. 2661–2667. DOI: 10.1016/S1540-7489(02)80324-8.

[70] C. Gierl, T. Gruendl, P. Debernardi, K. Zogal, C. Grasse, P. Meißner, S. Jatta and F. Küppers. 'Surface micromachined tunable single-mode tuning'. *Optics Express* 19.18 (2011), pp. 17336–17343. DOI: 10.1364/OE.19.017336.

[71] J. M. Rey, M. Fill, F. Felder and M. W. Sigrist. 'Broadly tunable mid-infrared VECSEL for multiple components hydrocarbon gas sensing'. *Applied Physics B: Lasers and Optics* 117.3 (2014), pp. 935–939. DOI: 10.1007/s00340-014-5911-1.

[72] A. Q. Liu and X. M. Zhang. 'A review of MEMS external-cavity tunable lasers'. *Journal of Micromechanics and Microengineering* 17.1 (2006), R1–R13. DOI: 10.1088/0960-1317/17/1/R01.

[73] W. Denzer, M. L. Hamilton, G. Hancock, M. Islam, C. E. Langley, R. Peverall and G. A. D. Ritchie. 'Near-infrared broad-band cavity enhanced absorption spectroscopy using a superluminescent light emitting diode'. *Analyst* 134.11 (2009), pp. 2220–2223. DOI: 10.1039/b916807a.

[74] F. Xu, Z. Lv, Y. G. Zhang, G. Somesfalean and Z. G. Zhang. 'Concentration evaluation method using broadband absorption spectroscopy for sulfur dioxide monitoring'. *Applied Physics Letters* 88.23 (2006). DOI: 10.1063/1.2211299.

[75] *LI-7500A open path CO2 / H2O gas analyser*. 2009.

[76] H. S. Wang, Y. G. Zhang, S. H. Wu, X. Lou, Z. G. Zhang and Y. K. Qin. 'Using broadband absorption spectroscopy to measure concentration of sulfur dioxide'. *Applied Physics B: Lasers and Optics* 100.3 (2010), pp. 637–641. DOI: 10.1007/s00340-010-4151-2.

[77] M. Cherchi, M. Harjanne, S. Ylinen, M. Kapulainen, T. Vehmas and T. Aalto. 'Flat-top MZI filters: a novel robust design based on MMI splitters'. *Proc. SPIE* 9752 (2016), pp. 975210–975219. DOI: 10.1117/12.2210937.

[78] N. Zia, J. Viheriälä, R. Koskinen, M. Koskinen, S. Suomalainen and M. Guina. 'Fabrication and characterization of broadband superluminescent diodes for 2 μm wavelength'. *Proc. SPIE* 9768 (2016), 97680Q–97680Q–9. DOI: 10.1117/12.2209720.

[79] N. Zia, J. Viheriälä, R. Koskinen, A. Aho, S. Suomalainen and M. Guina. 'High power (60 mW) GaSb-based 1.9fffdfffdfffdμm superluminescent diode with cavity suppression element'. *Applied Physics Letters* 109.23 (2016), p. 231102. DOI: 10.1063/1.4971972.

[80] G. Somesfalean, M. Sjofffdfffdholm, L. Persson, H. Gao, T. Svensson and S. Svanberg. 'Temporal correlation scheme for spectroscopic gas analysis using multimode diode lasers'. *Applied Physics Letters* 86.18 (2005), p. 184102. DOI: 10.1063/1.1921351.

[81] X. Lou, G. Somesfalean and Z. G. Zhang. 'Gas detection by correlation spectroscopy employing a multimode diode laser'. *Applied optics* 47.13 (May 2008), pp. 2392–8.

[82] X. Lou, G. Somesfalean, B. Chen, Y. G. Zhang, H. S. Wang, Z. G. Zhang, S. H. Wu and Y. K. Qin. 'Simultaneous detection of multiple-gas species by correlation spectroscopy using a multimode diode laser'. *Optics letters* 35.11 (2010), pp. 1749–51.

[83] G. Gao, B. Chen and B. Hu. 'Carbon dioxide measurement based on multimode diode laser correlation spectroscopy employing wavelength modulation techniques'. *Spectroscopy Letters* 47.1 (2013), pp. 6–11. DOI: 10.1080/00387010.2013.775462.

[84] T. Udem, R. Holzwarth and T. W. Hänsch. 'Optical frequency metrology'. *Nature* 416.6877 (2002), pp. 233–237. DOI: 10.1038/416233a.

[85] A. Huber, T. Udem, B. Gross, J. Reichert, M. Kourogi, K. Pachucki, M. Weitz and T. W. Hänsch. 'Hydrogen-deuterium 1S-2S isotope shift and the structure

of the deuteron'. *Physical Review Letters* 80 (1998), pp. 468–471. DOI: 10.1103/PhysRevLett.80.468.

[86] A. D. Ludlow, M. M. Boyd, J. Ye, E. Peik and P. O. Schmidt. 'Optical Atomic Clocks'. *Preprint at arxiv.org/abs/1407.3493 (to appear on Rev. Mod. Phys.)* 87.June (2015), pp. 1–86. DOI: 10.1393/ncr/i2013-10095-x.

[87] S. A. Diddams, L. Hollberg and V. Mbele. 'Molecular fingerprinting with the resolved modes of a femtosecond laser frequency comb'. *Nature* 445.7128 (Feb. 2007), pp. 627–30. DOI: 10.1038/nature05524.

[88] M. J. Thorpe, D. Balslev-clausen, M. S. Kirchner and J. Ye. 'Cavity-enhanced optical frequency comb spectroscopy: application to human breath analysis'. *Optics express* 16.4 (2008), pp. 6–15.

[89] A. Castrillo, A. Gambetta, D. Gatti, G. Galzerano, P. Laporta, M. Marangoni and L. Gianfrani. 'Absolute molecular density determinations by direct referencing of a quantum cascade laser to an optical frequency comb'. *Applied Physics B: Lasers and Optics* 110.2 (2013), pp. 155–162. DOI: 10.1007/s00340-012-5013-x.

[90] B. Bernhardt, A. Ozawa, P. Jacquet, M. Jacquey, Y. Kobayashi, T. Udem, R. Holzwarth, G. Guelachvili, T. W. Hänsch and N. Picqué. 'Cavity-enhanced dual-comb spectroscopy'. *Nature Photonics* 4.1 (2010), pp. 55–57. DOI: 10.1038/nphoton.2009.217.

[91] A. Foltynowicz, T. Ban, P. Masłowski, F. Adler and J. Ye. 'Quantum-noise-limited optical frequency comb spectroscopy'. *Physical Review Letters* 107.23 (Nov. 2011), p. 233002. DOI: 10.1103/PhysRevLett.107.233002.

[92] A. Foltynowicz, P. Masłowski, A. J. Fleisher, B. J. Bjork and J. Ye. 'Cavity-enhanced optical frequency comb spectroscopy in the mid-infrared application to

trace detection of hydrogen peroxide'. *Applied Physics B: Lasers and Optics* 110.2 (2013), pp. 163–175. DOI: 10.1007/s00340-012-5024-7.

[93] Y. Arita. 'Multi-mode absorption spectroscopy'. PhD thesis. 2008.

[94] J. Ye and S. T. Cundiff. *Femtosecond Optical Frequency Comb: Principle, Operation and Applications*. Springer US, 2006.

[95] W. H. Oskay, S. A. Diddams, E. A. Donley, T. M. Fortier, T. P. Heavner, L. Hollberg, W. M. Itano and S. R. Jefferts. 'Single-atom optical clock with high accuracy'. *Physical Review Letters* 020801.July (2006), pp. 1–4. DOI: 10.1103/PhysRevLett.97.020801.

[96] H. S. Margolis. 'Spectroscopic applications of femtosecond optical frequency combs'. *Chemical Society Reviews* 41.15 (2012), p. 5174. DOI: 10.1039/c2cs35163c.

[97] J. Mandon, G. Guelachvili and N. Picqué. 'Fourier transform spectroscopy with a laser frequency comb'. *Nature Photonics* 3.2 (2009), pp. 99–102. DOI: 10.1038/nphoton.2008.293.

[98] I. Coddington, W. Swann and N. Newbury. 'Coherent multiheterodyne spectroscopy using stabilized optical frequency combs'. *Physical Review Letters* 100.1 (Jan. 2008), p. 013902. DOI: 10.1103/PhysRevLett.100.013902.

[99] G. B. Rieker, F. R. Giorgetta, W. Swann, J. Kofler, A. M. Zolot, L. C. Sinclair, E. Baumann, C. Cromer, G. Petron, C. Sweeney, P. P. Tans, I. Coddington and N. Newbury. 'Frequency-comb-based remote sensing of greenhouse gases over kilometer air paths'. *Optica* 1.5 (2014), pp. 290–298.

[100] L. C. Sinclair, I. Coddington, W. Swann, G. B. Rieker, A. Hati, K. Iwakuni and N. Newbury. 'Operation of an optically coherent frequency comb outside the metrology lab'. *Optics express* 22.6 (Mar. 2014), pp. 6996–7006. DOI: 10.1364/OE.22.006996.

[101] Y. Wang, M. G. Soskind, W. Wang and G. Wysocki. 'High-resolution multi-heterodyne spectroscopy based on Fabry-Perot quantum cascade lasers'. *Applied Physics Letters* 104.3 (Jan. 2014), p. 031114. DOI: 10.1063/1.4862756.

[102] T. Ideguchi, A. Poisson, G. Guelachvili, N. Picqué and T. W. Hänsch. 'Adaptive real-time dual-comb spectroscopy'. *Nature Communications* 5.20 (2014), pp. 21932–21939. DOI: 10.1038/ncomms4375.

[103] L. S. Rothman, I. E. Gordon, Y. Babikov, A. Barbe, D. Chris Benner, P. F. Bernath, M. Birk, L. Bizzocchi, V. Boudon, L. R. Brown, A. Campargue, K. Chance, E. A. Cohen, L. H. Coudert, V. M. Devi, B. J. Drouin, A. Fayt, J. M. Flaud, R. R. Gamache, J. J. Harrison, J. M. Hartmann, C. Hill, J. T. Hodges, D. Jacquemart, A. Jolly, J. Lamouroux, R. J. Le Roy, G. Li, D. A. Long, O. M. Lyulin, C. J. Mackie, S. T. Massie, S. N. Mikhailenko, H. S. P. Müller, O. V. Naumenko, A. V. Nikitin, J. Orphal, V. I. Perevalov, A. Perrin, E. R. Polovtseva, C. Richard, M. A. H. Smith, E. Starikova, K. Sun, S. A. Tashkun, J. Tennyson, G. C. Toon, V. G. Tyuterev and G. Wagner. 'The HITRAN2012 molecular spectroscopic database'. *Journal of Quantitative Spectroscopy and Radiative Transfer* 130 (2013), pp. 4–50. DOI: 10.1016/j.jqsrt.2013.07.002.

[104] L. S. Rothman, I. E. Gordon, R. J. Barber, H. Dothe, R. R. Gamache, A. Goldman, V. I. Perevalov, S. A. Tashkun and J. Tennyson. 'Journal of Quantitative Spectroscopy & Radiative Transfer HITEMP, the high-temperature molecular spectroscopic database'. *Journal of Quantitative Spectroscopy and Radiative Transfer* 111.15 (2010), pp. 2139–2150. DOI: 10.1016/j.jqsrt.2010.05.001.

[105] P. Duhamel and M. Vetterli. 'Fast fourier transforms: a tutorial review and a state of the art'. *Signal Processing* 19.4 (1990), pp. 259–299. DOI: 10.1016/0165-1684(90)90158-U.

[106] J. Abell, C. S. Kim, W. W. Bewley, C. D. Merritt, C. L. Canedy, I. Vurgaftman, J. R. Meyer and M. Kim. 'Mid-infrared interband cascade light emitting devices with milliwatt output powers at room temperature'. *Applied Physics Letters* 104.26 (2014). DOI: 10.1063/1.4886394.

[107] W. W. Bewley, C. S. Kim, C. L. Canedy, C. D. Merritt, I. Vurgaftman, J. Abell, J. R. Meyer and M. Kim. 'High-power, high-brightness continuous-wave interband cascade lasers with tapered ridges'. *Applied Physics Letters* 103.11 (2013), pp. 1–5. DOI: 10.1063/1.4821263.

[108] C. L. Canedy, J. Abell, C. D. Merritt, W. W. Bewley, C. S. Kim, M. Kim, I. Vurgaftman and J. R. Meyer. 'Pulsed and CW performance of 7-stage interband cascade lasers'. *Optics Express* 22.7 (2014), pp. 7702–10. DOI: 10.1364/OE.22.007702.

[109] M. Kim, W. W. Bewley, C. L. Canedy, C. S. Kim, C. D. Merritt, J. Abell, I. Vurgaftman and J. R. Meyer. 'High-power continuous-wave interband cascade lasers with 10 active stages'. *Optics Express* 23.8 (2015), pp. 9664–72. DOI: 10.1364/OE.23.009664.

[110] I. Vurgaftman, W. W. Bewley, C. L. Canedy, C. S. Kim, M. Kim, C. D. Merritt, J. Abell and J. R. Meyer. 'Interband cascade lasers with low threshold powers and high output powers'. *IEEE Journal on Selected Topics in Quantum Electronics* 19.4 (2013). DOI: 10.1109/JSTQE.2012.2237017.

[111] I. Vurgaftman, C. L. Canedy, C. S. Kim, M. Kim, W. W. Bewley, J. R. Lindle, J. Abell and J. R. Meyer. 'Mid-infrared interband cascade lasers operating at ambient temperatures'. *New Journal of Physics* 11.12 (Dec. 2009), p. 125015. DOI: 10.1088/1367-2630/11/12/125015.

[112] G. Agrawal. *Long-Wavelength Semiconductor Lasers*. Springer, 2012.

[113] I. Vurgaftman, W. W. Bewley, C. L. Canedy, C. S. Kim, M. Kim, C. D. Merritt, J. Abell, J. R. Lindle and J. R. Meyer. 'Rebalancing of internally generated carriers for mid-infrared interband cascade lasers with very low power consumption'. *Nature communications* 2 (Jan. 2011), p. 585. DOI: 10.1038/ncomms1595.

[114] C. L. Canedy, C. S. Kim, M. Kim, D. C. Larrabee, J. a. Nolde, W. W. Bewley, I. Vurgaftman and J. R. Meyer. 'High-power, narrow-ridge, mid-infrared interband cascade lasers'. *Journal of Vacuum Science & Technology B: Microelectronics and Nanometer Structures* 26.3 (2008), p. 1160. DOI: 10.1116/1.2884733.

[115] C.-T. Zheng, W. Ye, N. P. Sanchez, C. Li, L. Dong, Y. Wang, R. J. Griffin and F. K. Tittel. 'Development and field deployment of a mid-infrared methane sensor without pressure control using interband cascade laser absorption spectroscopy'. *Sensors and Actuators B: Chemical* 244 (2017), pp. 365–372. DOI: 10.1016/j.snb.2016.12.146.

[116] I. E. Trofimov, C. L. Canedy, C. S. Kim, M. Kim, W. W. Bewley, C. D. Merritt, I. Vurgaftman, J. R. Meyer and L. T. Le. 'Interband cascade lasers with long lifetimes'. *Applied Optics* 54.32 (2015), p. 9441. DOI: 10.1364/AO.54.009441.

[117] J. C. Lagarias, J. A. Reeds, M. H. Wright and P. E. Wright. 'Convergence properties of the Nelder-Mead simplex method in low dimensions'. *SIAM Journal on Optimization* 9.1 (1998), pp. 112–147. DOI: 10.1137/S1052623496303470.

[118] M. Meinshausen, S. J. Smith, K. Calvin, J. S. Daniel, M. L. T. Kainuma, J. Lamarque, K. Matsumoto, S. A. Montzka, S. C. B. Raper, K. Riahi, A. Thomson, G. J. M. Velders and D. P. P. van Vuuren. 'The RCP greenhouse gas concentrations and their extensions from 1765 to 2300'. *Climatic Change* 109.1 (2011), pp. 213–241. DOI: 10.1007/s10584-011-0156-z.

[119] P. C. D. Hobbs. 'Shot noise limited optical measurements at baseband with noisy lasers'. *Proc. SPIE* 1376 (Mar. 1991). Ed. by R. Roy, pp. 216–221. DOI: 10.1117/12.25014.

[120] D. York, N. M. Evensen, M. L. Martfffdfffdfffdfffdnez and J. De Basabe Delgado. 'Unified equations for the slope, intercept, and standard errors of the best straight line'. *American Journal of Physics* 72.2004 (2004), p. 367. DOI: 10.1119/1.1632486.

[121] M. G. Lawrence. 'The relationship between relative humidity and the dewpoint temperature in moist air: a simple conversion and applications'. *Bulletin of the American Meteorological Society* 86.July 2004 (2005), pp. 225–233. DOI: 10.1175/BAMS-86-2-225.

[122] P. C. D. Hobbs. 'Ultrasensitive laser measurements without tears'. *Applied optics* 36.4 (Feb. 1997), pp. 903–20.

[123] E. Whiting. 'An empirical approximation to the Voigt profile'. *Journal of Quantitative Spectroscopy and Radiative Transfer* 8.6 (1968), pp. 1379–1384. DOI: 10.1016/0022-4073(68)90081-2.

[124] J. Olivero and R. Longbothum. 'Empirical fits to Voigt line-width: a brief review'. *Journal of Quantitative Spectroscopy & Radiative Transfer* 17.2 (1977), pp. 233–236. DOI: 10.1016/0022-4073(77)90161-3.